Development of High-Performance π-Conjugated Donor: Acceptor Structures and Their Application Aimed for the Relaxation of Efficiency Rolloff in Organic Light-Emitting Diodes

金, 鍾旭

https://hdl.handle.net/2324/4110477

出版情報：Kyushu University, 2020, 博士（工学）, 課程博士
バージョン：
権利関係：

2020

Doctoral Dissertation

Development of High-Performance π-Conjugated Donor–Acceptor Structures and Their Application Aimed for the Relaxation of Efficiency Rolloff in Organic Light-Emitting Diodes

Jonguk Kim

Department of Chemistry and Biochemistry

Graduate School of Engineering

Kyushu University

Table of Contents

Chapter 1. General Introduction

Chapter 2. The Effect of Substitution Position of the Donors for Green Thermally Activated Delayed Fluorescence Organic Light-Emitting Diodes with Small Efficiency Rolloff

Chapter 3. High-Triplet-Energy Bipolar Host Molecules for Sky-Blue Thermally Activated Delayed Fluorescence Organic Light-Emitting Diodes with Reduced Efficiency Rolloff

Chapter 4. A Nanosecond Time Scale Delayed Fluorescence Molecule for Deep-Blue Organic Light-Emitting Diodes with Small Efficiency Rolloff

Chapter 1

General Introduction

1. 1. Introduction of OLED History

Organic light-emitting materials possess an ability of light emission in response to a various kinds of energy stimulation. Major sources for this excitation energy include mechanical, optical, electrical, and chemical processes, which respectively lead to mechano-, photo-, electro-, and chemi-luminescence. Organic light-emitting diodes (OLEDs), which exhibit electroluminescence (EL), have been emerging as the basis for next-generation advanced displays and lighting applications because of their unique advantages such as high EL efficiency, high contrast, light-weight, good flexibility, and potentially low manufacturing cost.[1]

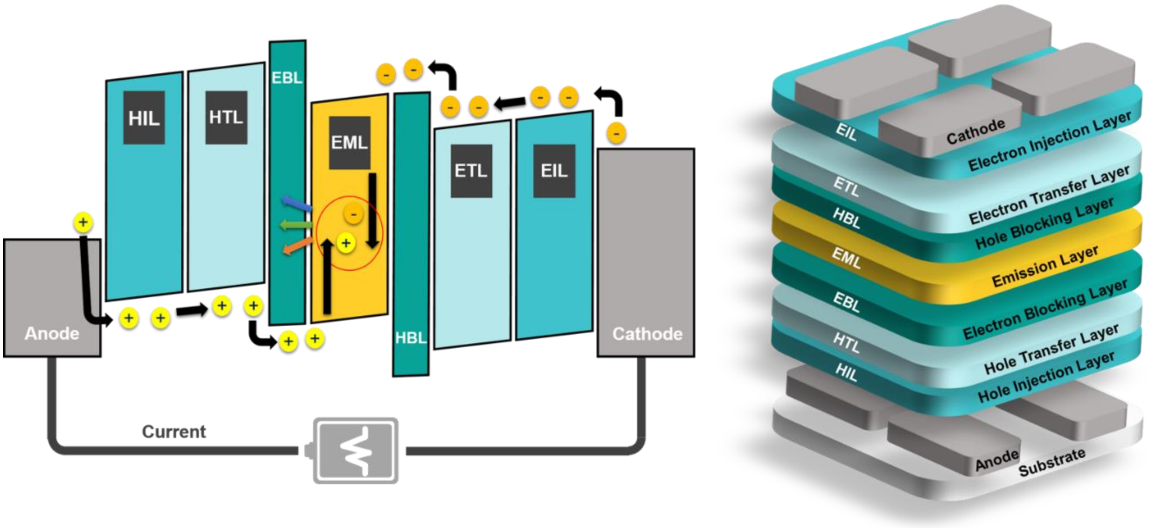

Figure 1-1. Schematic energy diagram of an OLED.

Figure 1-1 depicts the basic operation of a typical OLED. Holes are injected from the anode into the hole conduction level (*E*v) of the hole injection layer (HIL), whereas electrons are injected from the cathode into the electron conduction level (*E*c) of the electron injection layer under electrical excitation. These carriers are transported through the hole transporting layer (HTL) and the electron transporting layer (ETL) toward the emitting layer (EML), respectively, in which the both carriers recombine to form excitons, leading to light emission as fluorescence or phosphorescence in the EML. Additionally, an electron-blocking layer (EBL) and a hole-blocking layer (HBL) are commonly included to confine charge carriers within the EML, hence enhancing the recombination efficiency. On the anode side, the energy levels of the E_{v} of HIL and HTL in respect to the work function of the anode layer should be as close as possible, in order to transport holes to the EML efficiently. Likewise, on the cathode side, the EIL should have a relatively deep E_c, and the ETL should have a high electron mobility to inject and transport electrons efficiently. Using such a multilayer structure, carriers are effectively injected, transported and recomibined, resulted in EL.[2]

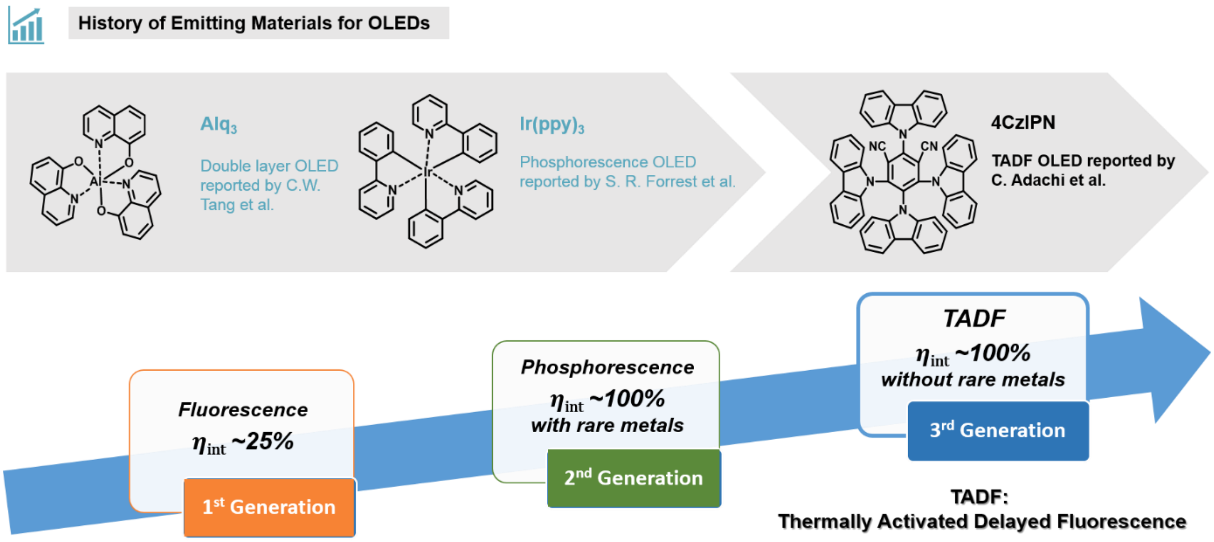

Figure 1-2. Molecular structures of tris(8-hydroxyquinolinato)aluminum (**Alq$_3$**), tris [2-phenylpyridinato-C^2,*N*]iridium(III) (**Ir(ppy)$_3$**), and 1,2,3,5tetrakis(carbazol-9-yl)-4,6-dicyanobenzene (**4CzIPN**).

The history and background of the development of OLEDs are summarized in **Figure 1-2**. A first-generation OLED was first reported by Professor Ching W. Tang in 1987. This O has been assinged as a fluorescence based OLED (1st generation). The efficiency of the fluorescent OLED was limted with an internal quantum efficiency (IQE) of 25 %, which was based on the fluorescencnt tris(8-hydroxyquinolinato)aluminum (**Alq$_3$**, **Figure 1-2**) emitter. This fluorescent device reported by Tang exhibited a luminance of 1,000 cd m^{-2} at a voltage of 10 V and an external EL quantum efficiency (η_{ext}) of almost 1.0%.[3] In 1999, Professor Stephen R. Forrest realized a second-generation OLED with an IQE of nearly 100% based on a room temperature phosphorescenct material. High-performance OLEDs were demonstrated by employing a green phosphorescent emitter, tris(2-phenylpyridine)iridium (**Ir(ppy)$_3$**, **Figure 1-2**) in the EML. Such a device exhibited a peak η_{ext} of 8.0% together with a current efficiency (η_c) of 28 cd A^{-1} and power efficiency (η_p) of 31 lm W^{-1}, respectively. At 100 cd m^{-2}, η_{ext} and η_p are 7.5% and 19 lm W^{-1}, respectively, with an operating voltage of 4.3 V.[4] In 2012, Professor

Chihaya Adachi reported the third-generation OLED, in which an IQE of nearly 100% was achieved with the use of a thermally activated delayed fluorescence (TADF) mechanism using pure organic aromatics. A green OLED utilizing 1,2,3,5-tetrakis(carbazol-9-yl)-4,6-dicyanobenzene (**4CzIPN**, **Figure 1-2**) achieved a high maximum η_{ext} of close to 20%. Since then, the research and development of TADF-OLEDs have been rapidly growing through the unlimited molecular design of new organic materials.[5-7]

1. 2. Photophysical Processes of Emissive Organic Materials

In organic materials, all unique photo-, thermal-, and chemical properties can be ascribed to molecular structures. In particular, light emission from organic molecules follows photopysical processes. Organic molecules excited by opticall or electrical excitation return to their original ground states with light emission of their excited states' nature, where they also undergo various deactivation processes simultaneously.

1. 2. 1. Solvatochromic Shifts

The photophysical properties of the luminescent organic materials in solution are greatly affected by solvent polarity, other dissolved impurities, temperatures, pH, and concentrations. Thus, the absorption and emission spectra are greatly affected by these environmental variables. In fact, the high sensitivity of emissive organic materials originates mainly from the interactions with the polarity of solvents occurring in the local environment during the excitation lifetime, which is called solvent relaxation as shown in **Figure 1-3**.[8,9]

TADF molecules based on CT emissive states have strong dipole moments in their excited states. Therefore, in solution, since solvent molecules in their ground states have dipole moments, they interact with the dipole moment of the emissive molecules, resulted in an ordered distribution of solvent molecules around the TADF molecule. Likewise, the solvent's dipole interacts with the dipole moment of the excited molecule, and the dipoles reorganize to minimize the free energy, resulting in a relaxed excited state after excitation of a molecule in solution. As the solvent polarity increases, the solvent relaxation affects are increased, leading to the emission shifts to lower energies. In fact, most TADF molecules can be identified by the red-shifting of the CT-emission, which is dependent on the polarity of the solvent. The polarity of the molecule also determines the extent of the sensitivity of the excited state to solvent effects. A higher polar molecule exhibits a much stronger effect comparing to non-polar molecules.

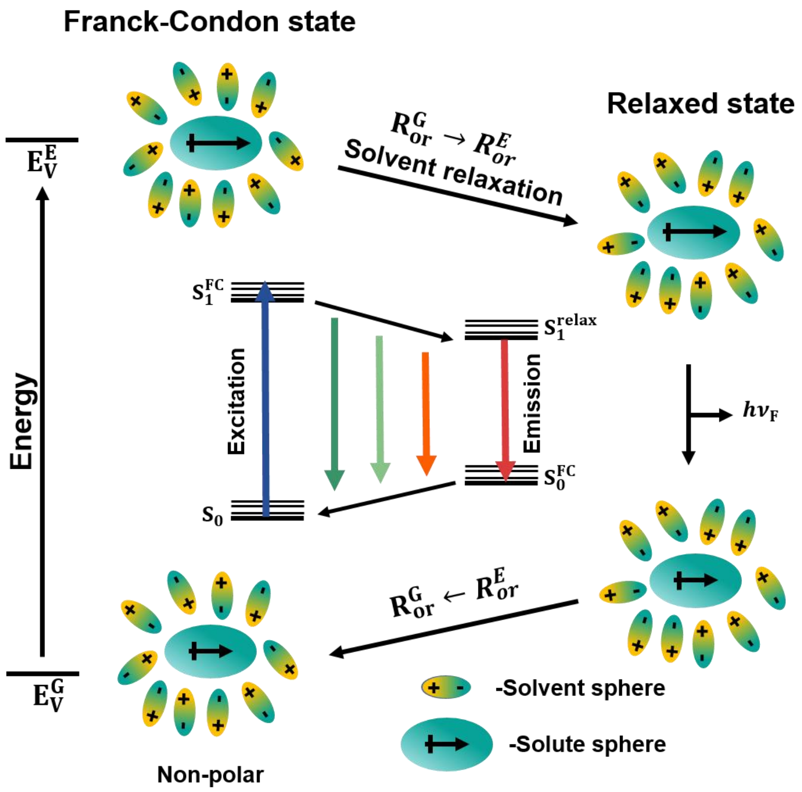

Figure 1-3. Jablonski diagram for the effect of solvent relaxation, resulting in the solvatochromic shift in a solute-solvent system.

The solvatochromic shifts in the wavenumbers of absorption and emission for such a mechanism are given by the following equations, respectively:

$$\overline{v_a} = -\frac{2}{hc}\mu_g(\mu_e - \mu_g)a^{-3}\Delta f + const. \qquad \textbf{(1-1)}$$

$$\overline{v_f} = -\frac{2}{hc}\mu_e(\mu_g - \mu_e)a^{-3}\Delta f + const. \qquad \textbf{(1-2)}$$

where *h* is Plank's constants, *c* is the velocity of light, *a* is the radius of the cavity in which the solute resides, μ_g and μ_e are the transition dipole moments in ground states and excited states, and Δf is the orientation polarizability defined as

$$\Delta f = f(\varepsilon) - f(n^2) = \frac{\varepsilon - 1}{2\varepsilon + 1} - \frac{n^2 - 1}{2n^2 + 1} \qquad \textbf{(1-3)}$$

The Δf of each solvent is calculated using its dielectric constant (ε) which varies for each solvent.

Subtraction of **Eq. 1-1** and **1-2** leads to the Lippert-Mataga equation:[10]

$$\overline{v_a} - \overline{v_f} = \frac{2}{hc}\left(\mu_e - \mu_g\right)^2 a^{-3}\Delta f + const. \qquad \textbf{(1-4)}$$

As shown in **Eq. 1-4**, the Stoke's shift depends only on the absolute magnitude of the charge transfer dipole moment (μ_e–μ_g) and it can be approximated using this equation. Thus, general emissive molecules exhibit a linear relationship when stoke's shift is plotted against Δf, which is called a Lippert's plot. In the case of intermolecular charge transfer (ICT) emissive states for molecules having donor–acceptor (D–A) combined molecular frameworks, $\overline{v_f}$ is very sensitive towards the changes in Δf compared to non-CT state emissive molecules, so the Lippert's plots for these materials exhibit a steeper slope. Therefore, we can predict the origin of emission by using a solvatochromic study. For instance, strong CT emission based TADF molecules is expected to be very sensitive with solvent polarity. [11]

1. 2. 2. Energy Transfer (Förster & Dexter Energy Transfer)

Excited molecules return to their ground states with undergoing various deactivation processes. Among them, intermolecular energy transfer systems can be explained in two ways as shown in **Figure 1-4**. One is long-range Förster energy transfer and the other is short-range Dexter energy transfer. Förster energy transfer (FRET, dipole-dipole interactions) is an electron coupling based on dipole-dipole interaction within the range of up to 10 nm.[12] A donor molecule (D) can transfer an energy to a acceptor molecule (A) nonradiatively. It is proportional to the spectral overlap between the emission spectrum of a donor and the absorption spectrum of an acceptor and the relative orientation between the emission dipole moment of a donor and the absorption dipole moment of an acceptor. The efficiency of Förster energy transfer depends on the distance between the donor and acceptor pair (r) given by following equation:

$$E_{\mathrm{F}} = R_0^6/(R_0^6 + r^6) \qquad \textbf{(1-5)}$$

where R_0 is Förster radius at which the efficiency of energy transfer becomes 50%. It can be determined from photophysical data by employing the following equation:

$$R_0^6 = \frac{9(\ln 10)\kappa^2 \Phi_{\mathrm{D}}}{128\pi^5 N_A n^4} J \qquad \textbf{(1-6)}$$

where κ^2 is the dipole orientation factor, Φ_D is the PL quantum efficiency of the donor in the absence of transfer, N_A is the Avogadro's number, n is the refractive index of the medium, and J is the spectral overlap integral calculated as

$$J = \int f_{\mathrm{D}}(\lambda)\varepsilon_{\mathrm{A}}(\lambda)d\lambda \quad \textbf{(1-7)}$$

where f_{D} is the normalized emission spectrum of the donor and ε_{A} is the molar extinction coefficient in the absorption spectrum of the acceptor.

On the other hand, Dexter energy transfer (the exchange coupling) can be dominated by an electron exchange interaction between a donor molecule (D) to an acceptor molecule (A). The excited hole and electron of the donor are simulationally transferred to these levels of the acceptor through an electron exchange at a short distance (~ 1 nm). The Dexter energy transfer process can be used for singlet–singlet and triplet–triplet energy transfers (**Figure 1-6**). Therefore, the wavefunction overlap between the donor and acceptor is required for efficient Dexter energy transfer.[13] The rate constant of Dexter energy transfer is given by the following equation:

$$k_D = \left(\frac{2\pi}{h}\right)\kappa^2 \exp\left(\frac{-2R_{\mathrm{DA}}}{L}\right)J \qquad \textbf{(1-8)}$$

where R_{DA} is the distance between the donor and acceptor, L is the sum of the Van der Waals radii of the donor and acceptor, and J is the spectral overlap integral calculated as the **Eq. 1-7**.

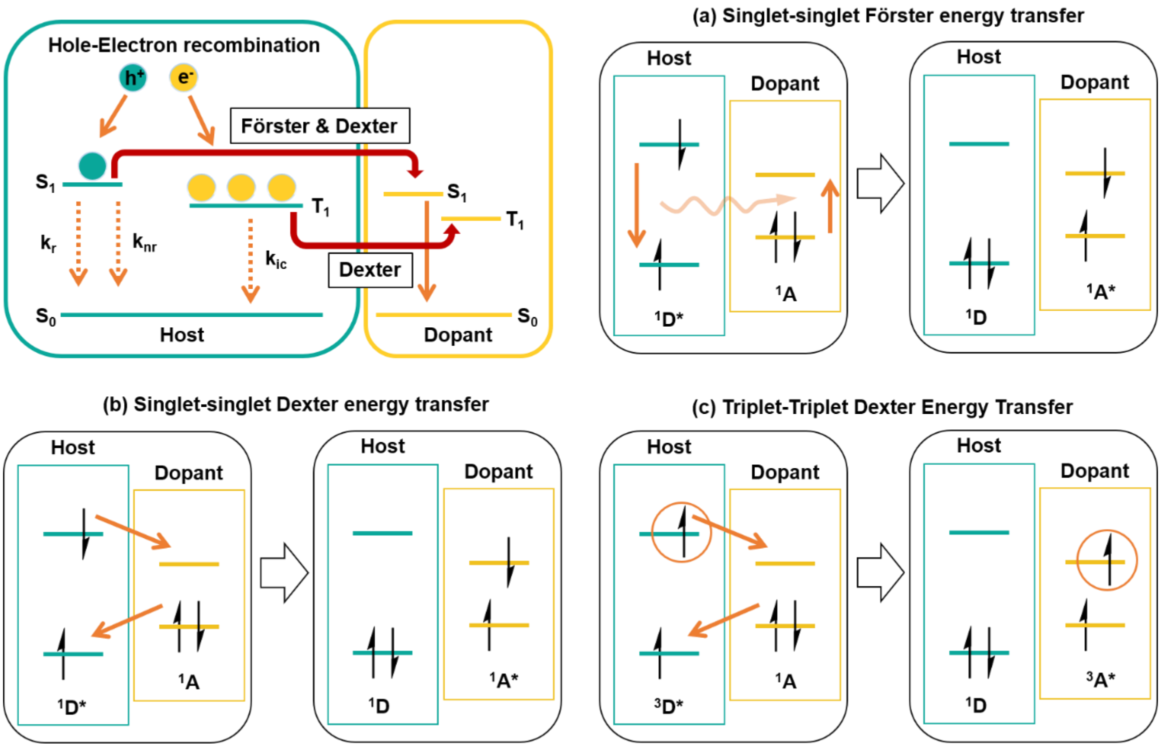

Figure 1-4. Schematic representation for (a) singlet–singlet Förster energy transfer, (b) singlet–singlet Dexter energy transfer, and (c) triplet–triplet Dexter energy transfer.

1. 2. 3 Energy Transfer in Host–Guest System

TADF emitters are usually doped into a suitable host matrix at a low concentration (1–30 wt%) to prevent the concentration quenching and avoid self-absorption of the emitting materials in OLEDs to realize high EL efficiency. There are two kinds of energy transfer mechanisms from a host (exciton donor) to a guest (exciton acceptor) in a host−guest system, i.e., Förster and Dexter energy transfers. Förster energy transfer is only allowed between a host singlet state to a guest singlet state because the transitions between the same spin multiplicity are spin-allowed, while transitions between the different spin multiplicity are forbidden (Wingner rule).[14-16]

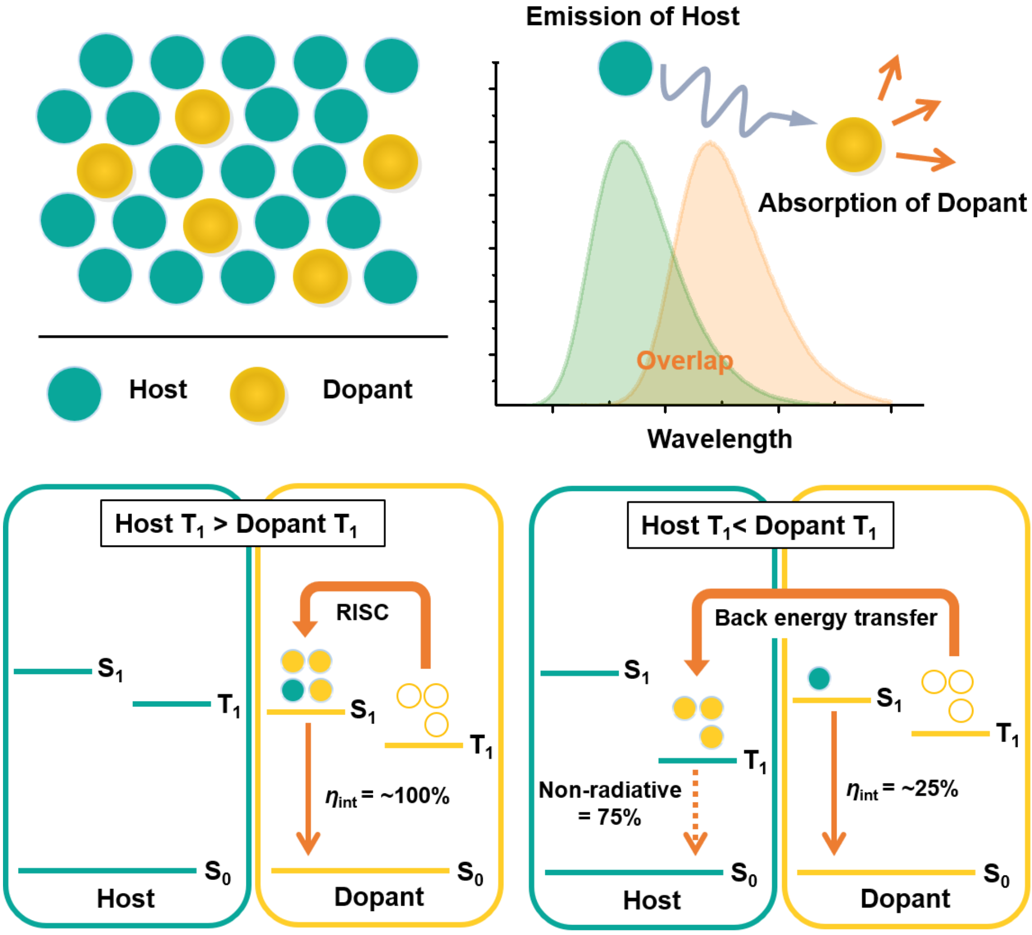

Figure 1-5. Schematic representation for energy transfer between a host material and a TADF emitter under electrical excitation. S_0^H and S_0^D are the ground states, S_1^H and S_1^D are the lowest excited singlet states, and T_1^H and T_1^D are the lowest excited triplet states of the host and TADF materials, respectively.

As shown in **Figure 1-7**, host matrices largely influence the exciton recombination zone to shift closer to the emission layer/electron-transport layer (EML/ETL) interface in case of the hole-transporting (HT) hosts. Likewise, the recombination region is likely to be shifted to the EML/HTL interface in case of the electron-transporting (ET) hosts. Therefore, OLEDs with narrow charge recombination zones lead to induce severe efficiency rolloff due to the local accumulation of high-density triplet excitons, especially at high current densities. Whereas, the bipolar host matrices can provide a broad recombination region, resulted in improved efficiencies, stability and relaxation of rolloff than those of the unipolar host matrices.

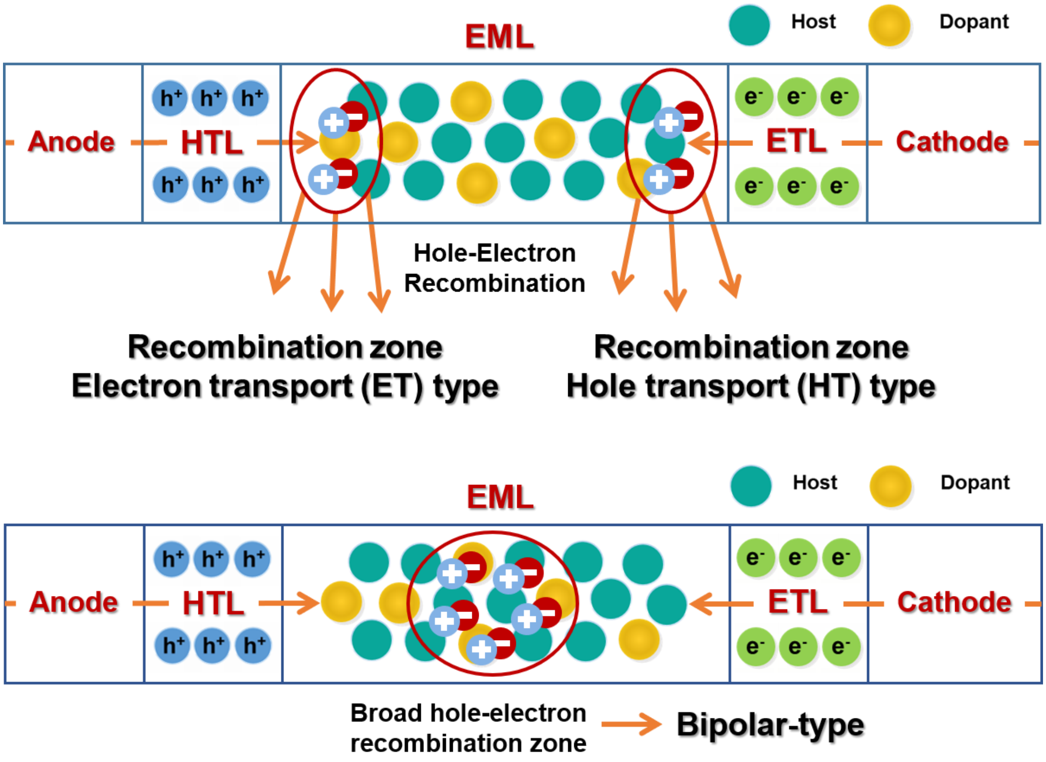

Figure 1-6. Schematic representation for EL processes in unipolar host and bipolar hosts.

1. 2. 4. Exciton Annihilation Processes

Exciton annihilation processes are caused by the collision of two excitons or that of an exciton and a polaron. The annihilation processes lead to a decrease of the EL quantum efficiency with an increased current density, resulted in poor device performance. Since such annihilation processes deactivate one exciton to a graund state, it results in the loss of excitons. Under electrical excitation, both excitons and polarons of excited molecules undergo several annihilation processes as shown in **Figure 1-7.**[17]

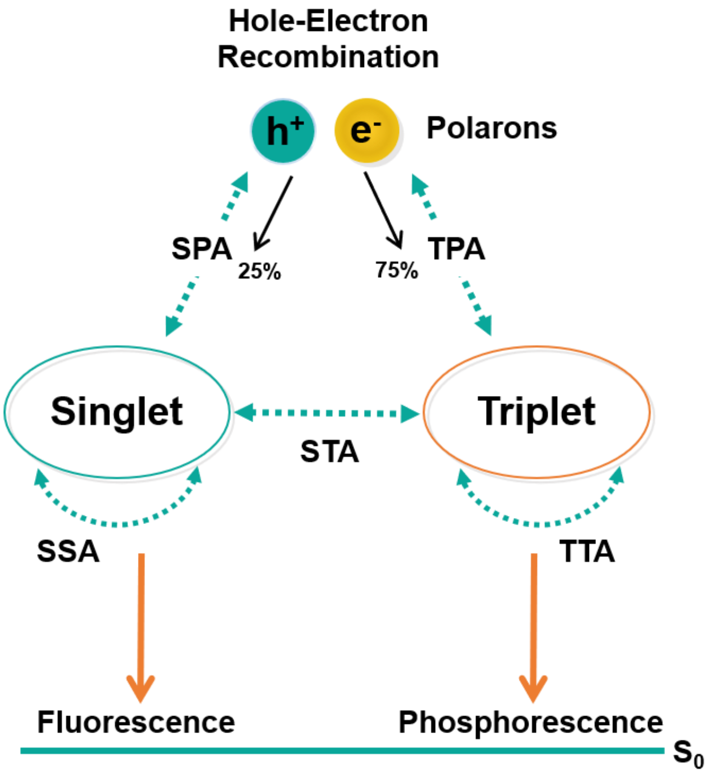

Figure 1-7. Schematic representation for energy transfer between a host material and a TADF emitter under electrical-excitation.

Singlet–singlet annihilation (SSA) usually appears in solid-states. SSA occurs between two excited singlet states, and one singlet exciton results in deactivation as a result of dipole-dipole interactions through Förster energy transfer. Therefore, this is one of the main reason for the efficiency rolloff in fluorescent OLEDs.[17-19] SSA can be described as the following process.

$$S_1 + S_1 \xrightarrow{K_{SSA}} S_0 + S_n^* \overset{IC}{\rightarrow} S_0 + S_1 + Q \quad \textbf{(1-9)}$$

where K_{SSA} is the rate constant of SSA, Q is heat.

Singlet–triplet annihilation (STA) can be caused by the interaction between singlet and triplet excited states and it occurs through energy transfer via long dipole-dipole interaction.[20-22] This phenomenon can be widely observed in conventional fluorescence and TADF based OLEDs. While it should not be dominate in phosphorescent OLEDs, since singlet excitons undergo fast ISC from S_1 to T_1 states.[23,24] STA can be described as the following process.

$$S_1 + T_1 \xrightarrow{K_{STA}} S_0 + T_n^* \overset{IC}{\rightarrow} S_0 + T_1 + Q \quad \textbf{(1-10)}$$

where K_{STA} is the rate constant of STA, Q is heat.

Triplet–triplet annihilation (TTA) occurs between two excited triplet states through Dexter energy transfer. Two triplet excitons react to form a higher singlet excited state by exchange energy transfer. Conventional fluorescent materials have a nanosecond scale emission lifetime, whereas rather long emission lifetimes of excited triplet excitons in microsecond scale are observed in phosphorescence and TADF materials.[24-26] Compared to fluorescent OLEDs, TADF or phosphorescent OLEDs can achieve a much higher brightness, while significant efficiency rolloffs are commonly observed in these OLEDs at a high brightness. Such phenomenon can be attributed to the relatively long exciton lifetime of the triplet excitons.[27-29] TTA can be described as the following process.

$$T_1 + T_1 \xrightarrow{K_{TTA}} \{S_0 + S_n^*\} + \{S_0 + T_n^*\} \quad \mathbf{(1\text{-}11)}$$

where K_{TTA} is the rate constant of TTA.

Exciton–polaron annihilation is the interaction between an exciton and a polaron, i.e., the annihilation process of an exciton by a polaron such as singlet–polaron annihilation (SPA) and triplet–polaron annihilation (TPA) which occur in the excited singlet or triplet states with free or trapped charge carriers. SPA and TPA can be described as the following processes.[30,31]

$$S_1 + D_0 \xrightarrow{K_{SPA}} S_0 + D_n^* \overset{IC}{\rightarrow} S_0 + D_1 + Q \quad \mathbf{(1\text{-}12)}$$

$$T_1 + D_0 \xrightarrow{K_{TPA}} S_0 + D_n^* \overset{IC}{\rightarrow} S_0 + D_1 + Q \quad \mathbf{(1\text{-}13)}$$

where D is the spin state of polaron, Q is heat, k_{SPA} is the rate constant of SPA, and k_{TPA} is the rate constant of TPA.

To realize high-brightness OLEDs for practical applications, several concepts such as decreasing the exciton lifetime of emitters, reducing molecular aggregation in an emitting layer, and broadening of the recombination zone in an emitting layer have been proposed.[32,33]

1. 3. Luminescence Mechanism of Emissive Organic Molecules

1. 3. 1. Fluorescence and Phosphorescence

When a molecule is excited by photon absorption, the transition from its ground state (S_0) to a lowest excited singlet state (S_1) and/or higher excited singlet states (S_2–S_n) occur with the transient time of 10^{-13} to 10^{-15} s. Then, the electron relaxes to the lowest vibrational level of the same electronic energy level. This process is known as a vibrational relaxation (v_r), called as internal conversion (IC). These processes are also fast of 10^{-10} to 10^{-14} s.

Fluorescence is the light emission from $S_1 \rightarrow S_0$ transition with the transition lifetime ranging from 10^{-5} to 10^{-9} s.[34] Intersystem crossing (ISC) is a non-radiative transition from the excited singlet state to the excited triplet state. This process is slower (10^{-5} to 10^{-10}) than the IC process because of the forbidden spin-flipping process as shown in **Figure 1-8**.

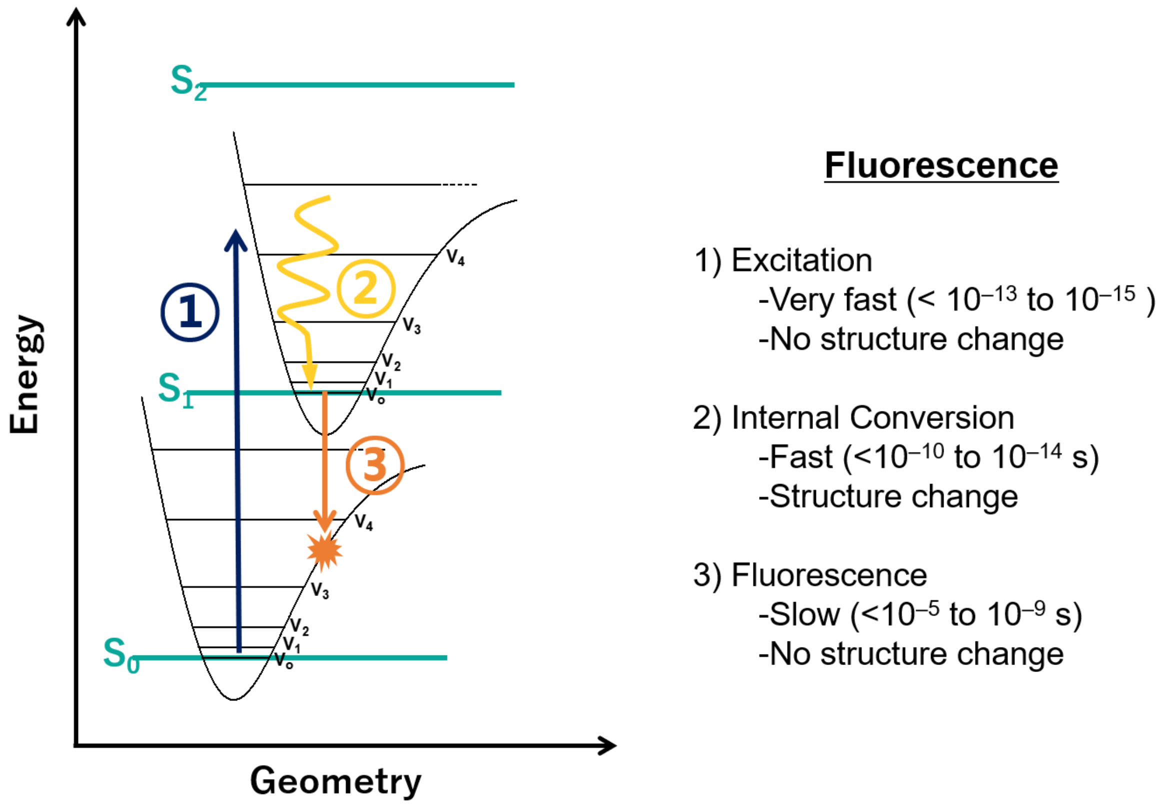

Fluorescence

1) Excitation
   - -Very fast (< 10^{-13} to 10^{-15})
   - -No structure change

2) Internal Conversion
   - -Fast (<10^{-10} to 10^{-14} s)
   - -Structure change

3) Fluorescence
   - -Slow (<10^{-5} to 10^{-9} s)
   - -No structure change

Figure 1-8. Schematic representation for fluorescence mechanism under electrical-excitation.

$$\text{(Fluorescence)} \qquad S_0 + h\nu_{ex} \longrightarrow S_1 \longrightarrow S_0 + h\nu_{em} \quad \textbf{(1-14)}$$

Phosphorescence is the radiative transition from T_1 to S_0 states with a change in spin angular momentum with the transition time ranging from 10 to 10^{-9} s as shown in **Figure 1-9**. When luminescence is produced by electrical excitation, i.e., EL, the emission can again results from both fluorescence and phosphorescence.[35] Fluorescent OLEDs utilize singlet excitons for EL, while phosphorescent OLEDs utilize both singlet and triplet excitons for EL. Due to the branching ratio of singlet and triplet excitons, the production efficiency of singlet excitons is limited to 25%. In contrast, phosphorescent OLEDs can utilize both singlet and triplet excitons for EL. Therefore, an ideal 100% of electrogenerated excitons can be harvested. Moreover, in order to suppress non-radiative recombination, emitters are often doped into a wide energy gap host layer to minimize the exciton quenching effect.

$$\text{(Phosphorescence)} \quad S_0 + h\nu_{ex} \longrightarrow S_1 \longrightarrow T_1 \longrightarrow S_0 + h\nu_{em} \quad \textbf{(1-15)}$$

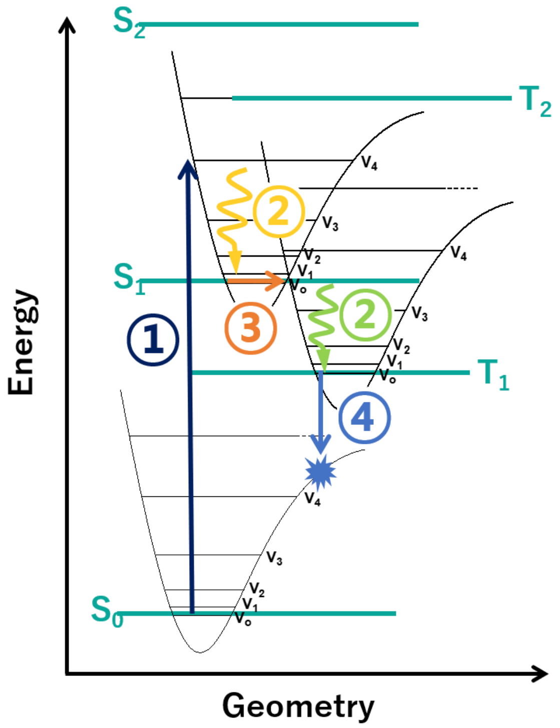

Phosphorescence

1) Excitation
    -Very fast (< 10^{-13} to 10^{-15})
    -No structure change

2) Internal Conversion
    -Fast (<10^{-10} to 10^{-14} s)
    -Structure change

3) Intersystem Crossing
    -Fast (<10^{-5} to 10^{-10} s)
    -No structure change

4) Phosphorescence
    -Slow (<10 to 10^{-9} s)
    -No structure change

Figure 1-9. Schematic representation for phosphorescence mechanism under electrical-excitation.

Delayed fluorescence is the radiative transition from S_1 to S_0 states via ISC and reverse intersystem crossing (RISC) processes of excitons and that happens with the transition time ranging from 10^{-3} to 10^{-9} s as shown in **Figure 1-10**. RISC is a non-radiative transition from a triplet excited state to a singlet excited state, which can occur when molecules possessing a small ΔE_{ST}. This process displays nearly same spectrun with the fluorescence. However, its decay time is longer than that of the fluorescence because a molecule emits light after recycling of the ISC and RISC processes.

$$\text{(Delayed fluorescence)} \quad S_0 + h\nu_{ex} \longrightarrow S_1 \longrightarrow T_1 \longrightarrow S_1 \longrightarrow S_0 + h\nu_{em} \quad \textbf{(1-16)}$$

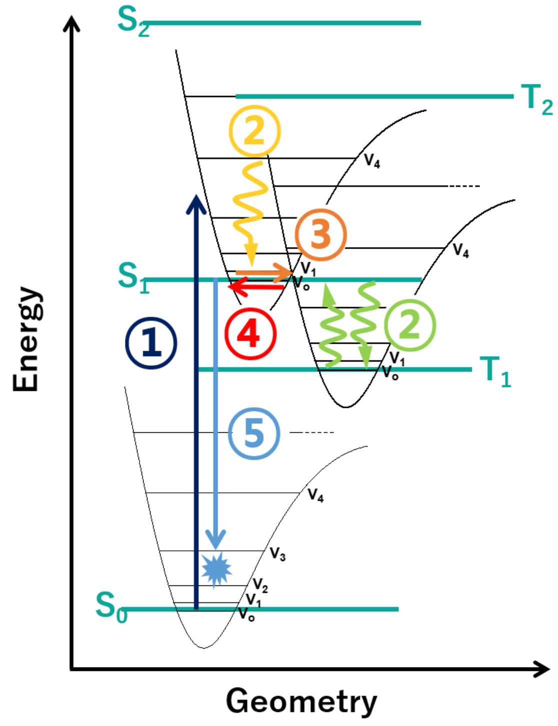

Delayed fluorescence

1) Excitation
   - Very fast (< 10^{-13} to 10^{-15})
   - No structure change

2) Internal Conversion
   - Fast (<10^{-10} to 10^{-14} s)
   - Structure change

3) Intersystem Crossing
   - Fast (<10^{-5} to 10^{-10} s)
   - No structure change

4) Reverse Intersystem Crossing
   - Slow (<10^{-3} to 10^{-9} s)
   - No structure change

5) Delayed fluorescence
   - Slow (<10 to 10^{-9} s)
   - No structure change

Figure 1-10. Schematic representation for delayed fluorescence mechanism under electrical-excitation.

1. 3. 2. Thermally Activatived Delayed Fluorescence (TADF) Process

1. 3. 2. 1. Design Principle for TADF Molecules

Efficient TADF emission can be usually observed in the organic materials with a small ΔE_{ST} ($k_{\mathrm{B}}T \approx 25.6$ meV) because the RISC process can be strongly accelerated by the thermal energy at 300 K. In accordance to Fermi's Golden rule, k_{RISC} is expressed by the following equation:

$$k_{\mathrm{RISC}} \propto \left|\langle \mathrm{S}|\hat{H}_{\mathrm{SOC}}|\mathrm{T}\rangle\right|^2 \exp\left(\frac{-\Delta E_{\mathrm{ST}}}{k_{\mathrm{B}}T}\right) \qquad \textbf{(1-17)}$$

where, $<\mathrm{S}|\hat{H}_{\mathrm{SOC}}|\mathrm{T}>$ is the spin–orbit coupling (SOC) matrix element between the excited singlet (S) and triplet (T) states, k_{B} is the Boltzmann constant, and T is temperature. The RISC process in purely organic materials with a negligiblely small H_{SO} can be accelerated by realizing a small ΔE_{ST}.[36] Here, assuming S_0 energy (E_0) is zero, the S_1 energy (E_{S}), T_1 (E_{T}) energy, and ΔE_{ST} of a molecule are given by the following equations:

$$E_0 = 0 \qquad \textbf{(1-18)}$$

$$E_S = E_0 + K + J \qquad \textbf{(1-19)}$$

$$E_T = E_0 + K - J \qquad \textbf{(1-20)}$$

$$\Delta E_{ST} = 2J > 0 \qquad \textbf{(1-21)}$$

where K is the electron repulsion energy between negative charge distributions and J is the electron exchange energy between the different states. Thus, the ΔE_{ST} depends only on the electron exchange energy and is precisely equal to $2J$ (**Eqs. 1-19-21**).[37] J, which is associated with the Pauli principle, is expressed by the following equation of the overlap integral between the highest occupied molecular orbital (HOMO) and the lowest unoccupied molecular orbital (LUMO):

$$J = \iint \Phi_{\mathrm{H}}(1)\Phi_{\mathrm{L}}(2)\left(\frac{e^2}{r_{12}}\right)\Phi_{\mathrm{L}}(2)\Phi_{\mathrm{H}}(1)dr_1dr_2 \qquad \textbf{(1-22)}$$

where Φ_{H} and Φ_{L} are the wavefuctions of the HOMO and LUMO, respectively, e is the charge on an electron and r_{12} is the distance separating the electrons. From these equations, ΔE_{ST} value can be controlled by the overlap integral between the two states. The energy diagram of benzophenone shown in **Figure 1-11** serves as an exemplified case. The π–π* transition of benzophenone has relatively a large ΔE_{ST} due to their large orbital overlap, whereas the n–π* transition has relatively a small ΔE_{ST} owing to their small orbital overlap.

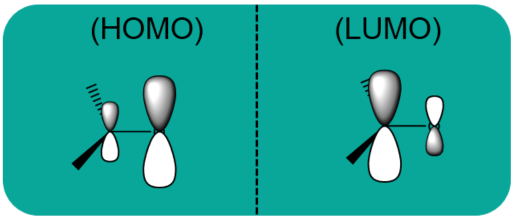

→ Large orbital overlap between *π* and *π* *

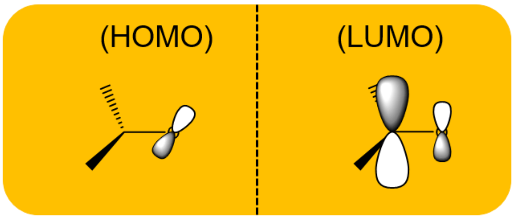

→ Small orbital overlap between n and *π* *

Figure 1-11. π–π* (upper) and n–π* (lower) orbital overlap in benzophenone.

Therefore, the small overlap between the HOMO and LUMO in a molecule leads to minimizing the electron exchange interactions, resulting in a small ΔE_{ST}. Under this condition, the RISC process can be strongly accelerated. However, a weak frontier orbital overlap is a drawback for efficient light emission, because a negligible spatial overlap of the HOMO and LUMO results in the loss of transition dipole moment according to the Fermi's Golden rule. Therefore, both small ΔE_{ST} and proper orbital overlap should be well balanced when designing novel efficient TADF molecules.

1. 3. 2. 2. Determination of Rate Constants for TADF

The rate constants of TADF materials can be calculated by fitting corresponding rate equations. $k_{\mathrm{r}}{}^{\mathrm{S}}$ and $k_{\mathrm{nr}}{}^{\mathrm{S}}$ are the radiative and non-radiative decay rate constants of the S_1 state, k_{ISC} and k_{RISC} are the ISC and RISC rate constants, respectively, k_{d} is the radiative decay rate constant of the S_1 state involving the ISC and RISC processes, and $k_{\mathrm{nr}}{}^{\mathrm{T}}$ is the non-radiative decay rate constant of the T_1 state. Φ is corresponding PL quantum efficiencies. The PL quantum efficiencies (Φ_{PL}) of the prompt (Φ_{p}) and delayed (Φ_{d}) components can be experimentally obtained from the transient PL decay curves (**Figure 1-12**) and the absolute Φ_{PL}. The lifetimes of the prompt (τ_{p}) and delayed (τ_{d}) components were determined by fitting the transient PL decay curves by the following equation:

$$\mathrm{y} = y_0 + A_{\mathrm{p}} e^{-x/\tau_{\mathrm{p}}} + A_{\mathrm{d}} e^{-x/\tau_{\mathrm{d}}} \qquad \textbf{(1-23)}$$

where, A_{p} and A_{d} are the area of the prompt and delayed components. In the presence of ISC and RISC between the S_1 and T_1 states, the rate constants of the prompt (k_{p}) and delayed (k_{d}) components can be expressed by the following formulas:[38]

$$k_{\mathrm{p}} = \frac{1}{\tau_{\mathrm{p}}} = k_{\mathrm{r}}^{\mathrm{S}} + k_{\mathrm{nr}}^{\mathrm{S}} + k_{\mathrm{ISC}} \qquad \textbf{(1-24)}$$

$$k_{\mathrm{d}} = \frac{1}{\tau_{\mathrm{d}}} = k_{\mathrm{nr}}^{\mathrm{T}} + \left(1 - \frac{k_{\mathrm{ISC}}}{k_{\mathrm{r}}^{\mathrm{S}} + k_{\mathrm{nr}}^{\mathrm{S}} + k_{\mathrm{ISC}}}\right) k_{\mathrm{RISC}} \qquad \textbf{(1-25)}$$

where $k_{\mathrm{r}}{}^{\mathrm{S}}$ and $k_{\mathrm{nr}}{}^{\mathrm{S}}$ are the radiative and non-radiative decay rate constants of the S_1 state, respectively, and k_{ISC} and k_{RISC} are the ISC ($S_1 \rightarrow T_1$) and RISC ($T_1 \rightarrow S_1$) rate constants, respectively. $k_{\mathrm{r}}{}^{\mathrm{S}}$ and k_{ISC} are assumed to be much faster than $k_{\mathrm{nr}}{}^{\mathrm{T}}$ and k_{RISC}. Φ_{p}, Φ_{d}, and Φ_{ISC} are given by the following formulas:

$$\Phi_{\mathrm{p}} = \frac{k_{\mathrm{r}}^{\mathrm{S}}}{k_{\mathrm{r}}^{\mathrm{S}}+k_{\mathrm{nr}}^{\mathrm{S}}+k_{\mathrm{ISC}}} = \frac{k_{r}^{S}}{k_{p}} \qquad \textbf{(1-26)}$$

$$\Phi_{\mathrm{d}} = \sum_{k=1}^{\infty}(\Phi_{\mathrm{ISC}}\,\Phi_{\mathrm{RISC}})^{k}\,\Phi_{\mathrm{p}} = \frac{\Phi_{\mathrm{ISC}}\,\Phi_{\mathrm{RISC}}}{1-\Phi_{\mathrm{ISC}}\,\Phi_{\mathrm{RISC}}}\cdot\Phi_{\mathrm{p}} \qquad \textbf{(1-27)}$$

$$\Phi_{\mathrm{ISC}} = \frac{k_{\mathrm{ISC}}}{k_{\mathrm{r}}^{\mathrm{S}}+k_{\mathrm{nr}}^{\mathrm{S}}+k_{\mathrm{ISC}}} = \frac{k_{\mathrm{ISC}}}{k_{p}} \qquad \textbf{(1-28)}$$

From **Eq. 1-24–1-28**, the following equation for k_{RISC} can be obtained.

$$k_{\mathrm{RISC}} = \frac{k_{\mathrm{p}}k_{\mathrm{d}}}{k_{\mathrm{ISC}}}\frac{\Phi_{\mathrm{d}}}{\Phi_{\mathrm{p}}} \qquad \textbf{(1-29)}$$

Since the Φ_{p} exhibits almost negligible temperature dependence, we assume that $k_{\mathrm{nr}}^{\mathrm{S}} \approx 0$ at 300 K. Thus, the radiative and non-radiative rate constants and the corresponding decay efficiencies can be estimated.

The most critical parameter in OLEDs is η_{ext}, which describes the ratio between the number of emitted photons that are extracted to air per injected electrons and injected charge carriers:

$$\eta_{\mathrm{ext}} = (\gamma \times \eta_{\mathrm{ST}} \times \Phi_{\mathrm{PL}}) \times \eta_{\mathrm{out}} = \eta_{\mathrm{int}} \times \eta_{\mathrm{out}} \qquad \textbf{(1-30)}$$

where γ is the fraction of holes and electrons recombination to form excitons in an emitting layer (EML). η_{ST} is the exciton production efficiency resulting in the radiative transition according to the spin selection rules. Φ_{PL} is the PL quantum efficiency for radiative decay of the excitons and η_{out} is the light out-coupling efficiency, which is the fraction of the radiated photons from the device into air. γ and Φ_{PL} can be up to 100% by the advanced device architectures and well-designed molecules with a suppressed non-radiative activation, respectively. η_{r} can be changed by emission mechanisms (fluorescence = ~25% and phosphorescence = ~100%). Therefore, assuming η_{out} of 20%, η_{ext} of fluorescence-based OLEDs is limited to 5%, whereas phosphorescence-based OLEDs can be achieved high η_{ext} of up to 20%.[39] In contrary to both fluorescence and phosphorescence-based OLEDs, the directly generated T_1 excitons by carrier recombination in TADF-based OLEDs are converted into the S_1 state via the efficient RISC. Accordingly, the theoretical maxima of η_{int} for TADF-based OLEDs can be given by the following equation:

$$\eta_{\mathrm{int}} = \eta_{\mathrm{S}} \times \Phi_{\mathrm{p}} + \eta_{\mathrm{S}} \times \Phi_{\mathrm{d}} + \eta_{\mathrm{T}} \times \Phi_{\mathrm{d}}/\Phi_{\mathrm{ISC}} \qquad \textbf{(1-31)}$$

where η_S and η_T denote the singlet exciton and triplet exciton production rates (25% and 75%, respectively) and Φ_d is the ISC efficiency ($1 - \Phi_p$). Therefore, the theoretical maxima of η_{ext} for TADF-based OLEDs can be estimated and achieved up to 20%, assuming η_{out} of 20%.

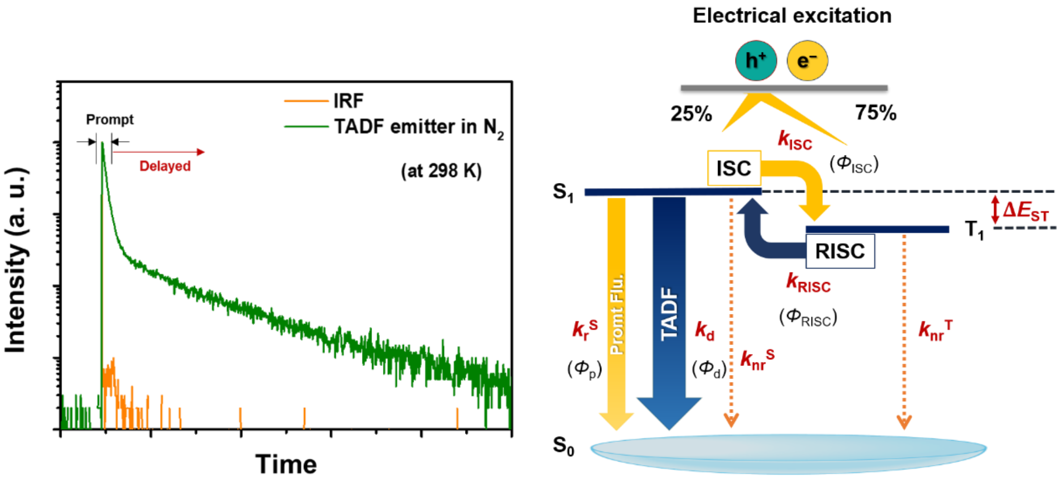

Figure 1-12. Transient PL decay of TADF (left) and PL decay processes for TADF materials (right).

1. 4. Efficiency Rolloff in OLEDs

Efficiency rolloff is a critical problem for high efficiency OLEDs. EL efficiencies are typically decreased with increasing current density by exciton quenching, and that is a drawback for practical pasisive matrix displays and lighting applications.[40,41] Therefore, the efficiency rolloff can be quantified by the critical current density (J), which represents the current density at which the efficiencies drop to the half of its maximum value. J is a useful measure to compare the efficiency rolloff of different OLEDs. Phosphorescence and TADF emitters-based OLEDs have been achieved high efficiencies of over 20%. However, the current density where the efficiency rolloff becomes 90% of its maximum is as low as 1−30 mA cm^{-2}. Instead, conventional fluorescence-based OLEDs can show relexed rolloff behavior, while η_{ext} remains only 5%.[42] The suppressed efficiency rolloff behavior in those of fluorescence-based OLEDs results from their short fluorescence lifetime compared to phosphorescence-based OLEDs. In fact, a truly low efficiency rolloff has so far only been achieved in fluorescence-based OLEDs. Further, blue-emitting devices based on phosphorescence and TADF-based OLEDs tend to have the highest efficiency rolloff. This can be attributed to the usually very poor chemical stability, i.e., irreversible degradation of emitters. In addition, the efficiency rolloff of the luminance is not only caused by the exciton annhilation but also by unbalanced hole and electron injection and transport. These unbalanced losses are due to energy barriers, low charge-carrier mobilities of the constituent materials that lead to a much higher efficiency rolloff in luminance. Such resistive losses can be minimized in devices with doped charge-transport layers, materials with high charge-carrier mobility. Thus, the efficiency rolloff in luminance reflects the superposition of several different effects. The efficiency rolloff behavior in luminance with increasing current density is rather difficult to predict as the theoretical modeling of charge transport remains unclear for the complexed multi-layer systems used in today's OLEDs.[43] Here, OLED efficiency can be given by the following equation:

$$\eta_{ext} = \gamma \times \chi \times \eta_{rad} \times \eta_{out} = \eta_{int} \times \eta_{\mathrm{out}} \tag{1-32}$$

where γ is the charge carrier balance, χ is the spin statistics factor (i.e., the ratio of singlet to triplet excitons), η_{rad} is the effective radiative efficiency of the emitter, and η_{out} is the outcoupling efficiency. Due to the presence of various annihilation processes, η_{ext} can be affected significantly.[44]

The efficiency rolloff of phosphorescence and TADF-based OLEDs is mostly relevant to TTA and TPA. Due to the long exciton lifetime of excited triplet states (in the microsecond to milisecond range), the probability for these excitons to annihilate is much higher than that of singlet states with the radiative lifetimes in the nanosecond range.[45,46] Therefore, efforts to reduce efficiency rolloff should focus on minimizing TTA and TPA, which can be realized by designing TADF emitters with short excition lifetimes in their triplet states (< 1 μs).

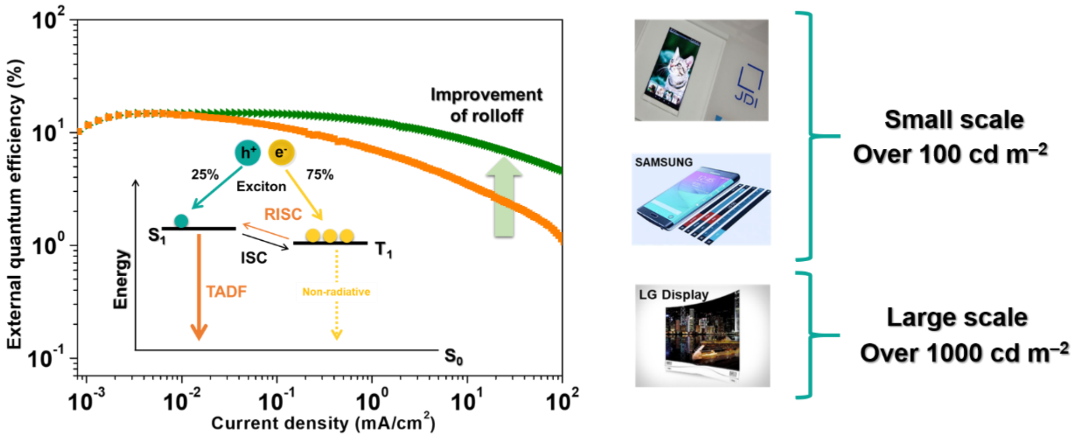

Figure 1-13. Transient PL decay of TADF (left) and luminescence requirements (right) of OLED display (JDI, https://www.j-display.com/, Samsung, http://news.samsungdisplay.com/, and LG, http://www.lgdisplay.com/).

1. 5. Motivation and Outline of This Dissertation

Flat-panel displays and solid-state lighting sources based on OLEDs have attracted considerable research interest since 1987, because of their high contrast, flexibility, and potentially low manufacturing costs as well as bright and full-color light emission from thin organic layers. Recently, the development of deep-blue TADF-OLEDs is most critical for achieving high efficiency OLEDs together with good CIE coordinates. The deep understanding of the structure-property relationships in TADF emitters is essential for developing deep-blue TADF emitters. Although fluorescence materials have attracted intense attention because of their high color purity and high reliability, the internal quantum efficiency of conventional fluorescent OLEDs is limited to 25%. As a result, this spin-statistical requirement limits the maximum external EL quantum efficiencies of fluorescent OLEDs only to 5%. On contratary, phosphorescent OLEDs can achieve external EL quantum efficiencies of over 20%. However, these phosphorescence materials still have some disadvantages: the rarity of the precious metals required for fabrication, toxicity, and difficulty in color rendering of the primary colors (blue, green, and red). In contrast, purely organic TADF materials can utilize both S_1 and T_1 excitons for light emission without the use of any precious metals. Thus, TADF molecules can act as a class of next-generation organic light-emitting materials. However, OLEDs based on TADF emitters with longer exiton lifetimes in their triplet states show serious efficiency rolloff, especially for blue TADF-OLEDs. Thus, this dissertation focuses on molecular design for highly efficient TADF materials with the aim for the relaxation of efficiency rolloff. Outline of this dissertation is as follows.

Chapter 2 reports a design straegy for efficient TADF molecules by employing the donor (D) units with the different position on the acceptor (A) unit. OLEDs using these different position TADF materials as emitters achieved high EL efficiencies compared with conventional fluorescence-based OLEDs. The TADF emission behavior of the doped films and OLED performance were largely depended on k_{RISC}, indicating that a delicate tuning of donor and acceptor arrangement surely enhances efficiency rolloff.

In **Chapter 3**, two ambipolar hosts, **CzPO** and **Cz3PO**, with high triplet energies were designed and synthesized for use in sky blue TADF-based OLEDs. Reduced efficiency rolloff was achieved in the sky blue TADF-based OLEDs using **CzPO** and **Cz3PO** as ambipolar hosts compared to the device with the electron-transporting (ET) host of **DPEPO**. The newly designed and synthesized series of two ambipolar host materials were applied to sky blue TADF-OLEDs, resulted in the reduced efficiency rolloff.

In **Chapter 4**, the molecular design strategies for highly efficient BN-based blue TADF molecules employing a highly twisted D–A molecular architecture were explored. The newly designed and synthesized series of BN-based blue TADF materials were applied to blue TADF-OLEDs. I succeeded to reduce efficiency rolloff because of a shorter exciton lifetime in the triplet state that reduced the exciton annihilations involving TTA and TPA.

References

[1] a) S. Reineke, F. Lindner, G. Schwartz, N. Seidler, K. Walzer, B. Lüssem, K. Leo, *Nature*, **2009**, 459, 234–238; b) M. A. McCarthy, B. Liu, E. P. Donghue, I. Kravchenko, D. Y. Kim, F. So, A. G. Rinzler, *Science*, **2011**, 332, 570–573.

[2] J. Kido, M. Kimura, K. Nagai, *Science*, **1995**, 267, 1332–1334.

[3] C. W. Tang, S. A. VanSlyke, *Appl. Phys. Lett.*, **1987**, 51, 913–915.

[4] M. A. Baldo, S. Lamansky, P. E. Burrows, M. E. Thompson, S. R. Forrest, *Appl. Phys.Lett.*, **1999**, 75, 4–6.

[5] H. Uoyama, K. Goushi, H. Nomura, C. Adachi, *Nature*, **2012**, 492, 234–238.

[6] C. W. Tang, S. A. Vanslyke, and C. H. Chen, *J. Appl. Phys*., **1989**, 65, 3610–3616.

[7] a) C. Adachi, M. A. Baldo, S. R. Forrest, M. E. Thompson, *Appl. Phys. Lett.*, **2000**, 77, 904–906; b) C. Adachi, M. A. Baldo, M. A. Thompson, S. R. Forrest, *J. Appl. Phys.*, **2001**, 90, 5048–5051.

[8] a) B. Valeur, Molecular Fluorescence: Principle and Applications, **2001**, Wiley-VHC Weinheim; b) Z. R. Grabowski, K. Rotkiewicz, W. Rettig, *Chem. Rev.*, **2003**, 103, 3899–4032.

[9] J. R. Lakowicz, *Principles of Fluorescence Spectroscopy*, **2006**, Springer.

[10] N. Mataga, Y. Kaifu, and M. Koizumi, *Bull. Chem. Soc. Jpn.*, **1956**, 29, 465–470.

[11] R. Ishimatsu, S. Matsunami, K. Shizu, C. Adachi, K. Nakano, T. Imato, *J. Phys. Chem. A*, **2013**, 117, 5607–5613.

[12] a) T. Förster, *Discuss Faraday Soc.*, **1959**, 27, 7–17; b) B. P. Lyons, A. P. Monkman, *Phys.Rev. B*, **2005**, 71, 235201; c) H. Fukagawa, T. Shimizu, Y. Iwasaki, T. Yamamoto, *Sci. Rep.*, **2017**, 7, 1*735*.

[13] a) D. L. Dexter, *J. Chem. Phys*., **1953**, 21, 836–850; b) L. S. Cui, S. Bin Ruan, F. Bencheikh, R. Nagata, L. Zhang, K. Inada, H. Nakanotani, L. S. Liao, C. Adachi, *Nat. Commun*., **2017**, 8, 2250.

[14] Y. Kawamura, J. Brooks, J. J. Brown, H. Sasabe, C. Adachi, *Phys. Rev. Lett*., **2006**, 96, 017404.

[15] a) D. Kasemann, R. Brückner, H. Fröb, K. Leo, *Phys. Rev. B*, **2011**, 84, 115208; b) M. Zhu, C. Yang, *Chem. Soc. Rev.*, **2013**, 42, 4963–4976.

[16] Y. Sun, N. C. Giebink, H. Kanno, B. Ma, M. E. Thompson, S. R. Forrest, *Nature*, **2006**, 440, 908–912.

[17] S. D. Babenko, V. A. Benderskii, V. I. Gol'Danskii, A. G. Lavrushko, V. P. Tychinskii, *Chem. Phys. Lett.*, **1971**, 8, 598–600.

[18] M. Pope, C. E. Swenberg, Electric Processes in Organic Crystals, Clarendon Press, Oxford University Press, **1982**.

[19] J. Fourny, G. Delacote, *Phys. Rev. Lett.*, **1968**, 21, 1085–1088.

[20] K. Masui, H. Nakanotani, C. Adachi, *Org. Electron.*, **2013**, 14, 2721–2726.

[21] N. Giebink, S. R. Forrest, *Phys. Rev. B*, **2009**, 79, 073302.

[22] Y. Zhang, M. Whited, M. E. Thompson, S. R. Forrest, *Chem. Phys. Lett.*, **2010**, 495, 161–165.

[23] M. A. Baldo, D. F O'Brien, Y. You, A. Shoustikov, S. Sibley, M. E. Thompson, S. R. Forrest, *Nature*, **1998**, 395, 151–154.

[24] S. Y. Lee, T. Yasuda, H. Nomura, C. Adachi, *Appl. Phys. Lett.*, **2012**, 101, 093306.

[25] N. C. Giebink, S. R. Forrest, *Phys. Rev. B*, **2008**, 77, 235215.

[26] Y. Kawamura, J. Brooks, J. J. Brown, H. Sasabe, C. Adachi, *Phys. Rev. Lett.*, **2006**, 96, 017404.

[27] S. Reineke, K. Walzer, K. Leo, *Phys. Rev. B*, **2007**, 75, 125328.

[28] a) G. Schwartz, S. Reineke, T. C. Rosenow, K. Walzer, K. Leo, *Adv. Funct. Mater.*, **2009**, 19, 1319–1333; b) T. C. Rosenow, M. Furno, S. Reineke, S. Olthof, B. Lüssem, K. Leo, *J. Appl. Phys.*, **2010**, 108, 113113.

[29] M. A. Baldo, R. J. Homes, S. R. Forrest, *Phys. Rev. B*, **2002**, 66, 035321.

[30] J. Kalinowski, W. Stampor, J. Mezyk, M. Cocchi. D. Virgili, V. Fattori. P. Di. Marco, *Phys. Rev. B*, **2002**, 66, 235321.

[31] a) L. Han, D. Yang, W. Li, B. Chu, Y. Chen, Z. Su, D. Zhang, F. Yan, Z. Hu, Z. Zhang, *Appl. Phys. Lett.*, **2008**, 93, 153303; b) H. Yersin, A. F. Rausch, R. Czerwieniec, T. Hofbeck, T. Fischer, *Chem. Rev*. **2011**, 255, 2622–2652.

[32] a) Y. Kawamura, L. Brooks, J. J. Brown, H. Sasabe, C. Adachi. *Phys. Rev. Lett.*, **2006**, 96, 017404; b) S. Reineke, T. C. Rosenow, B. Lussem, K. Leo, *Adv. Mater.*, **2010**, 22, 3189–3193.

[33] a) G. He, M. Pfeiffer, K. Leo, M. Hofmann, J. Birnstock, R. Pudzich, J. Salbeck, *Appl. Phys. Lett.*, **2004**, 85, 3911–3913; b) J.-W. Kang, S.-H. Lee, H.-D. Park, W.-I. Jeong, K.-M. Yoo, Y.-S. Park, J.-J. Kim, *Appl. Phys. Lett.*, **2007**, 90, 223508; c) J. Lee, J.-I. Lee, J. Y. Lee, H. Y. Chu, *Org. Electron.*, **2009**, 10, 1529–1533; d) M.-T. Lee, J.-S. Lin, M-T. Chu, M.-R. Tseng, *Appl. Phys. Lett.*, **2009**, 94, 083506.

[34] a) E. Aminaka, T. Tsutsui, and S. Saito, *J. Appl. Phys.*, **1996**, 79, 8808–8815; b) B. Valeur, M. N. Berberan-Santos, Molecular Fluorescence, WILEY-VCH, Weinheim, **2012**.

[35] a) A. R. Brown, K. Pichler, N. C. Greenham, D. D. C. Bradley, R. H. Friend, A. B. Holmes, *Chem. Phys. Lett.*, **1993**, 210, 61–66; b) T. Tsutsui, M. J. Yang, M. Yahiro, K. Nakamura, T. Watanabe, T. Tsuji, Y. Fukuda, T. Wakimoto, S. Miyaguchi, *Japanese J. Appl. Physics, Part 2 Lett.*, **1999**, 38, 1502–1504.

[36] N. J. Turro, V. Ramamurthy, J. C. Scaiano, Modern Molecular Photochemistry of Organic Molecules, University Science Books, Sausalito, **2010**.

[37] Y. Tao, K. Tuan, T. Chen, P. Xu, H. Li, R. Chen, C. Zheng, L. Zhang, W. Huang, *Adv. Mater.*, **2014**, 26, 7931–7958.

[38] a) K. Goushi, K. Yoshida, K. Sato, C. Adachi, *Nat. Photon.*, **2012**, 6, 253–258; b) I. S. Park, M. Numata, C. Adachi, T. Yasuda, *Bull. Chem. Soc. Jpn.*, **2016**, 89, 375–377.

[39] F. B. Dias, *Philos. Trans. R. Soc. A Math. Phys. Eng. Sci.*, **2015**, 373, 20140447.

[40] C. Murawski, K. Leo, M. C. Gather, *Adv. Mater.*, **2013**, 25, 6801–6827.

[41] a) M. A. Baldo, C. Adachi, S. R. Forrest, *Phys. Rev. B*, **2000**, 62, 10967–10977; b) K. H. Lee, L. K. Kang, J. Y. Lee, S. Kang, S. O. Jeon, K. S. Yook, J. Y. Lee, S. S. Yoon, *Adv. Funct. Mater.*, **2010**, 20, 1345–1358; c) M. C. Gather, A. Köhnen, K. Meerholz, *Adv. Mater.*, **2011**, 23, 233–248.

[42] S. Reineke, M. Thomschke, B. Lüssem, and K. Leo, *Rev. Mod. Phys.*, **2013**, 85, 1245–1293.

[43] M. Schober, M. Anderson, M. Thomschke, J. Widmer, M. Furno, R. Scholz, B. Lüssem, and K. Leo, *Physical Review B*, **2011**, 84, 165326.

[44] M. Furno, R. Meerheim, S. Hofmann, B. Lüssem, and K. Leo, *Physical Review B*, **2012**, 85, 115205.

[45] A. Köhler and H. Bässler, *Materials Science & Engineering R*, **2009**, 66, 71–109.

[46] a) B. Wallikewitz, D. Kabra, S. Gélinas, and R. H. Friend, *Physical Review B*, **2012**, 85, 045209; b) Y. Zhang and S. R. Forrest, *Physical Review Letters*, **2012**, 108, 267404; c) Y. Luo and H. Aziz, *Advanced Functional Materials*, **2010**, 20, 1285–1293.

Chapter 2

The Effect of Substitution Position of the Donors for Green Thermally Activated Delayed Fluorescence Organic Light-Emitting Diodes with Small Efficiency Rolloff

2. 1. Introduction

While TADF-OLEDs realized an ultimate internal quantum efficiency (IQE), exciton quenching under high current density is quite significant due to singlet–triplet annihilation, triplet–triplet annihilation, exciton-polaron annihilation processes and so on. These are mainly due to the long-lived triplet excitons, resulted in serious efficiency rolloff. A rational molecular design for efficient TADF molecules with the reduced exciton lifetime in triplet states are required to slove this issue.[1,2]

In this study, the combination of 9,9-dimethyl-9,10-dihydroacridine as a donor and dibenzo[*b*,*d*]thiophene 5,5-dioxide as an acceptor were focused to investigate the effect of substitution position of the donors for the enhancement of TADF characteristics.[3,4] Here, 3,7-bis(9,9-dimethyl-9,10-dihydroacridine)dibenzo[*b,d*]thiophene 5,5-dioxide (**3ASOA**) and 2,8-bis(9,9-dimethyl-9,10-dihydroacridine)dibenzo[*b,d*]thiophene 5,5-dioxide (**4ASOA**) have a different substituted position of the donors to the dibenzo[*b,d*]thiophene 5,5-dioxide accptor core. Their photophysical and electroluminescence (EL) properties were compareds, and these results indicated that the 2,8-substitution of the donors appreciably improves both photoluminescence (PL) and EL characteristics.

2. 2. Molecular Geometric and Electronic Structures

To understand the effect of variation of the D–A–D structures on the geometric and optoelectronic properties, quantum chemical calculations were performed on the designed molecules. The electronic structures of the TADF emitters were calculated using Gaussian 09 program package.[5] Ground-state geometries were optimized at the B3LYP/6-31G(d,p) level, and the lowest singlet and triplet excitations were calculated with time-dependent density functional theory (TD-DFT) using the optimized ground-state geometries. In **Figure 2-1**, the HOMOs of these molecules are predominantly located on the peripheral donor units, whereas the LUMOs are distributed over the phenylene linkers as well as the central acceptor core. The clear spatial separation of the frontier orbitals of all these molecules resulted in small calculated ΔE_{ST} values of close to 0.01 eV (**Table 2-1**), suggesting the high potential as TADF emitters. It is also evident that the dihedral angles between the peripheral donor units and the nearby phenylene linkers show 88 ± 2° in the optimized ground-state structures. Such highly distorted geometries of these molecules should arise from the steric effects of the hydrogen atoms groups at the *peri*-positions in the donor units, contributing to the decrease of the electron exchange energy for the intermolecular charge transfer (ICT) transitions. These results suggest that the phenylene linker has a stronger conjugation with the central acceptor core than the outermost donor units. The detail calculated results are summarized in **Table 2-1**.

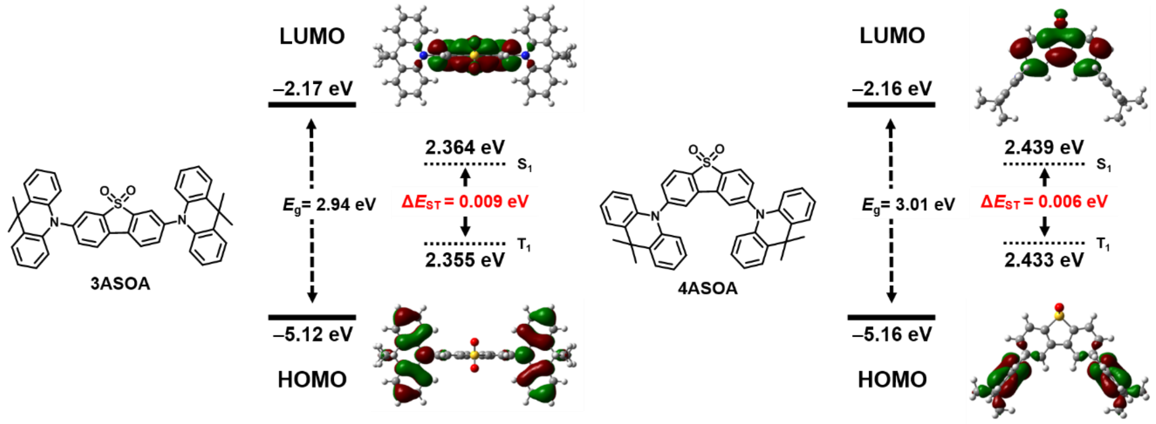

Figure 2-1. Molecular structures, energy levels and Kohn–Sham orbitals of the HOMO and LUMO of dibenzo[*b,d*]thiophene 5,5-dioxide-based TADF molecules characterized by DFT and TD-DFT calculations at the B3LYP/6-31G(d,p) level.

Table 2-1. Triplet and singlet excitation energies (vertical transition), oscillator strength (*f*), and transition configurations of dibenzo[*b,d*]thiophene 5,5-dioxide-based TADF molecules calculated by TD-DFT at the B3LYP/6-31G(d,p).

Compound	State	*E* (eV)	*f*	Main configuration[a]		ΔE_{ST} (eV)
3ASOA	S_1	2.364	0	H → L	99%	0.009
	S_2	2.381	0	H−1 → L	99%	
	T_1	2.355	0	H → L	98%	
	T_2	2.372	0	H−1 → L	98%	
4ASOA	S_1	2.439	0.002	H → L	99%	0.014
	S_2	2.447	0	H−1 → L	99%	
	T_1	2.425	0	H → L	98%	
	T_2	2.433	0	H−1 → L	98%	

[a] H → L represents the HOMO to LUMO transition. Excitation configurations with the highest contributions are presented, together with the corresponding transition symmetry and nature of the involved orbitals.

2. 3. Photophysical Properties

The molecular orbital distributions are reflected in the photophysical properties of dibenzo[*b,d*]thiophene 5,5-dioxide-based D–A–D type molecules. Basic photophysical parameters have been collected from UV–vis absorption and photoluminescence (PL) spectra and time-resolved transient PL analyses for toluene and dichloromethane solutions, and the results are summarized in **Table 2-2**.

Table 2-2. Photophysical data of the dibenzo[*b*,*d*]thiophene 5,5-dioxide-based TADF materials.

Compound	λ_{asb} [nm] sol$^{a)}$	λ_{PL} [nm] sol$^{a)}$ / film$^{b)}$	Φ_{PL}[%]$^{c)}$ sol$^{a)}$ / film$^{b)}$	τ_p [ns]$^{d)}$ / τ_d [ms]$^{d)}$	HOMO [eV]$^{e)}$	LUMO [eV]$^{f)}$	E_S / E_T [eV]$^{g)}$	ΔE_{ST} [eV]$^{h)}$
3ASOA	285,396$^{i)}$	515 / 506	12/ 72	8 / 4.8	−5.7	−3,1	2.91 / 2.65	0.26
4ASOA	284,376	508 / 511	13/ 88	12 / 1.4	−5.5	−2.8	2.82 / 2.73	0.09

[a)] Measured in oxygen-free toluene solution at room temperature; [b)] 6 wt%-doped thin film in a host matrix (host = mCP); [c)] Absolute PL quantum yield evaluated using an integrating sphere under a nitrogen atmosphere; [d)] PL lifetimes of prompt (τ_p) and delayed (τ_d) decay components for the 6 wt%-doped film measured using a Quantaurus-Tau (Hamamatsu Photonics Co.) at 298 K; [e)] Determined by photoelectron yield spectroscopy in pure neat films; [f)] Deduced from the HOMO and optical energy gap (E_g); [g)] Singlet (E_S) and triplet (E_T) energies estimated from onset wavelengths of the emission spectra at 300 and 25 K in the doped films, respectively; [h)] $\Delta E_{ST} = E_S - E_T$; [i)] Shoulder peak.

As shown in **Figure 2-2**, these compounds exhibited a broad and weak absorption band at longer wavelengths in the absorption spectra, which can be assigned to the ICT transitions from the peripheral donor units to the acceptor core. The ICT absorption band shifts to lower energies with increasing donor and acceptor strengths, which is well in accordance with the calculation results. Both materials exhibited green PL emission with maximum PL peaks (λ_{PL}) at 515 and 508 nm in toluene, respectively.

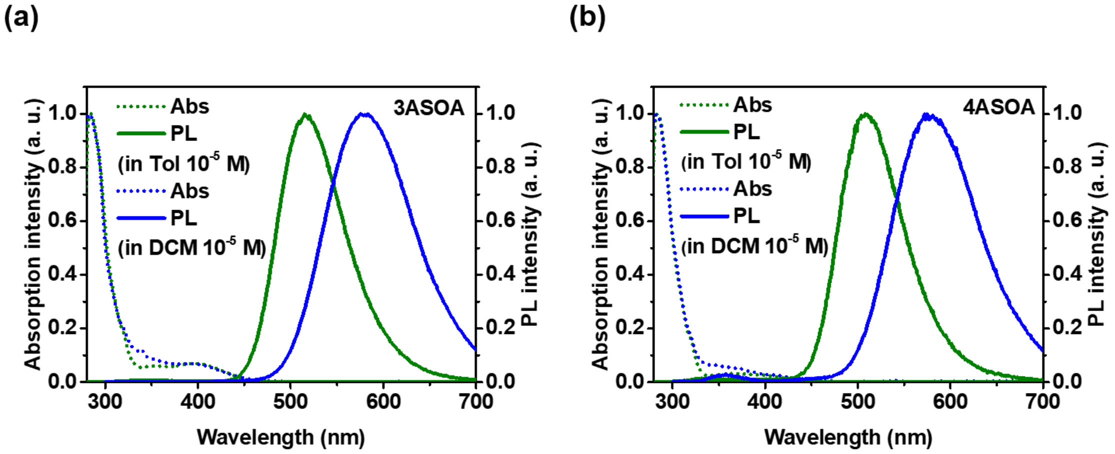

Figure 2-2. UV–vis absorption and PL spectra of dibenzo[*b*,*d*]thiophene 5,5-dioxide-based D–A–D type molecules in toluene (Tol) and dichloromethane (DCM).

For further investigation of the photophysical and TADF properties, doped thin films of the dibenzo[*b*,*d*]thiophene 5,5-dioxide-based emitters in a host matrix were prepared in order to avoid concentration quenching. 1,5-Bis(9-carbazolyl)benzene (mCP)[6] possessing a high T_1 energy (E_T) value of 2.9 eV was selected as a host to prevent the backward energy transfer from the excited the dibenzo[*b*,*d*]thiophene 5,5-dioxide-based emitters to the host material. As can be seen from **Figure 2-3**, in the doped films, green emission with with maximum λ_{PL} at 506 and 511 nm, respectively. The λ_{PL} position of the doped thin film with **3ASOA** was blue-shifted by about 10 nm compared with that measured in a toluene solution. Very similar behavior was also observed in **4ASOA**. In addition, **4ASOA** had a small PL shift between the neat and doped films, while the *meta*-position linked **3ASOA** showed a relatively large PL shift, since **3ASOA** has a strong dipole moment and exhibits a strong redshift in the neat film. This is consistent with the linear shape of **3ASOA**, which easily induces more intense aggregated states, leading to a larger redshift. This phenomenon can be explained by the different polarities of the solid host media.[7]

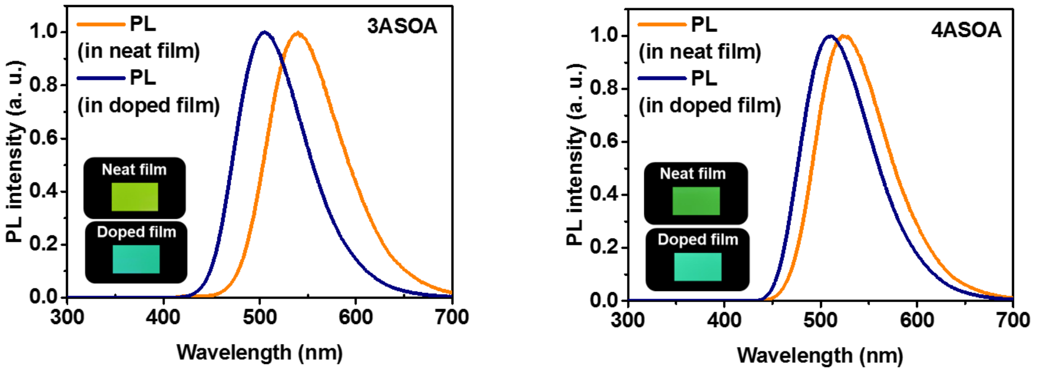

Figure 2-3. Photographs showing PL emission under UV irradiation and steady-state PL spectra of neat and 6 wt%-doped thin films in a mCP host matrix of the dibenzo[*b*,*d*]thiophene 5,5-dioxide-based emitters.

For **3ASOA**, a PL quantum yield (Φ_{PL}) of 12 ± 5% was obtained after N_2 bubbling, which is two times higher than that measured without bubbling (Φ_{PL} = 6 ± 5%); this is because of suppression of excited state energy transfer to oxygen molecules. Further, compared with their solution states, Φ_{PL} of both compounds increased considerably in the solid doped films (Φ_{PL} = 72–88%); this is because the rigid host matrices can suppress molecular fragment rotation and conformational changes. Thus, the experimental PL observations confirm the expected trend that the multi-color tuning of TADF can be accomplished by systematic structural variations.

Additionally, the solvatochromic effects of **3ASOA** and **4ASOA** were investigated in various solvents to understand their excited state properties (**Figure 2-4)**. Fluorescence spectra with large bathochromic shifts were observed when the solvent polarity was changed from non-polar toluene to polar DMF. The λ_{PL} of **3ASOA** were about 515 nm in toluene and 608 nm in DMF, whereas the λ_{PL} for **4ASOA** were 508 nm in toluene and 599 nm in DMF. Owing to increased solvent polarity, there was a large difference in the λ_{PL} ($\Delta\lambda_{max}$ = 100 nm for **3ASOA** and $\Delta\lambda_{max}$ = 96 nm for **4ASOA**), demonstrating pronounced positive solvatochromism.[8] Here, note that the amount of the spectral shift in **3ASOA** and **4ASOA** is nearly same even though they showed the different amount of the spectral shifts in their solid films. At this moment, the reason is unclear.

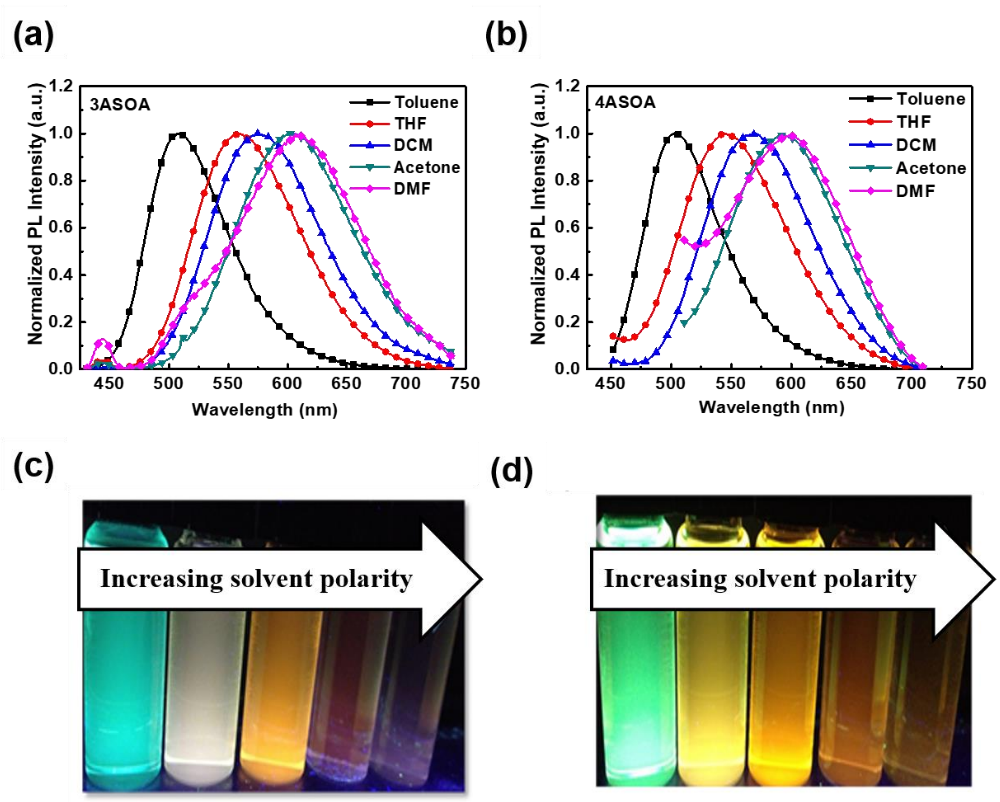

Figure 2-4. Normalized solvatochromic shifts of PL spectra of (a) **3ASOA** and (b) **4ASOA** and corresponding emission photographs of (c) **3ASOA** and (d) **4ASOA** in different solvents (the arrow show the shift from non-polar to polar solvent).

The phosphorescence spectra of **3ASOA** and **4ASOA** in frozen toluene matrices at 77 K are shown in **Figure 2-5**. The phosphorescence spectrum of **3ASOA** showed a vibronic-structured emission profile (i.e., LE character) and resulted in the decrease of the T_1 energy level. Whereas, **4ASOA** showed a broad and structureless spectrum, clearly indicating the CT characteristics. The transient PL characteristics of the emitters were also examined to reveal the TADF behavior. As exemplified in **Figure 2-6**, the transient PL curve of the 6 wt%-emitter doped film obviously indicated a nanosecond-order prompt decay component and a microsecond-order delayed decay component in the time range of 10 ms, which can be fitted with a biexponential model. The overall Φ_{PL} of the 6 wt%-**4ASOA**:mCP film was 88 ± 5% at room temperature, in which the fractional prompt (Φ_p) and TADF (Φ_d) efficiencies were estimated to be 20% and 68%, respectively. Similar PL quantum efficiency valuses were also observed in **3ASOA**. Conversely, the transient decay times of the delayed components of **3ASOA** and **4ASOA** differed significantly, while the fast components were similar values of 8 ns in **3ASOA** and 12 ns in **4ASOA**. Although **4ASOA** showed a short transient lifetime of ~1.4 ms, 3ASOA showed a long transient decay time of ~4.8 ms.

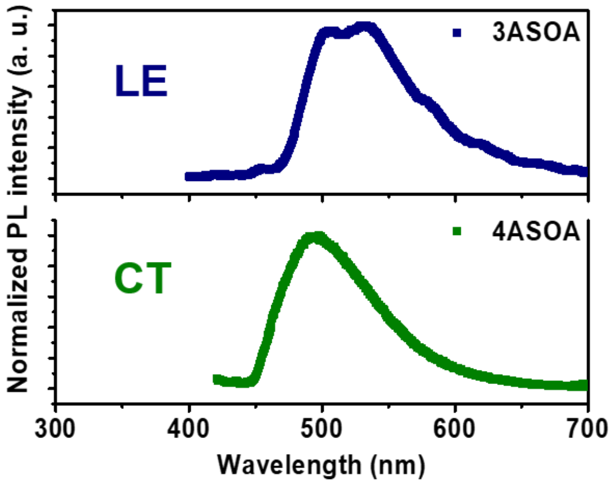

Figure 2-5. Normalized phosphorescence spectra of 3ASOA and 4ASOA in toluene solution matrices at 77 K.

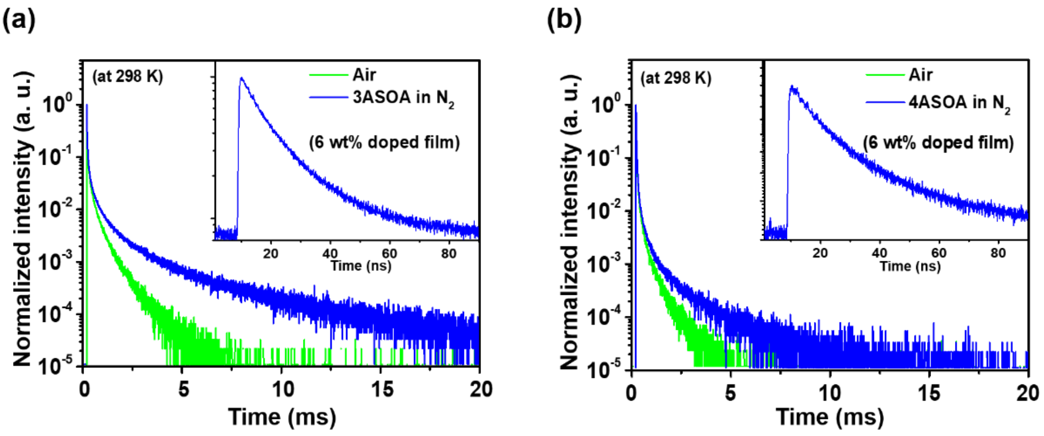

Figure 2-6. (a) Transient PL decay curves of the doped films in air (green) and in nitrogen (blue), and prompt components spectra (insert) of the doped films at 298 K.

From the room-temperature fluorescence and the low-temperature phosphorescence (25 K) spectra of the doped films (**Figure 2-7a**), the experimental ΔE_{ST} values are found to be in the order of **3ASOA** (0.26 eV) > **4ASOA** (0.09 eV), which are in good agreement with the trend of the delayed emission lifetimes. Temperature-dependence of the transient PL was also studied for the 6 wt%-emitter:mCP doped films in the temperature range of 50–300 K (**Figure 2-7b**). Apparently, the delayed emission was intensified when temperature was increased from 50 to 300 K, demonstrating that the $T_1 \rightarrow S_1$ RISC process was enhanced by the thermal energy, which is a direct evidence of TADF.

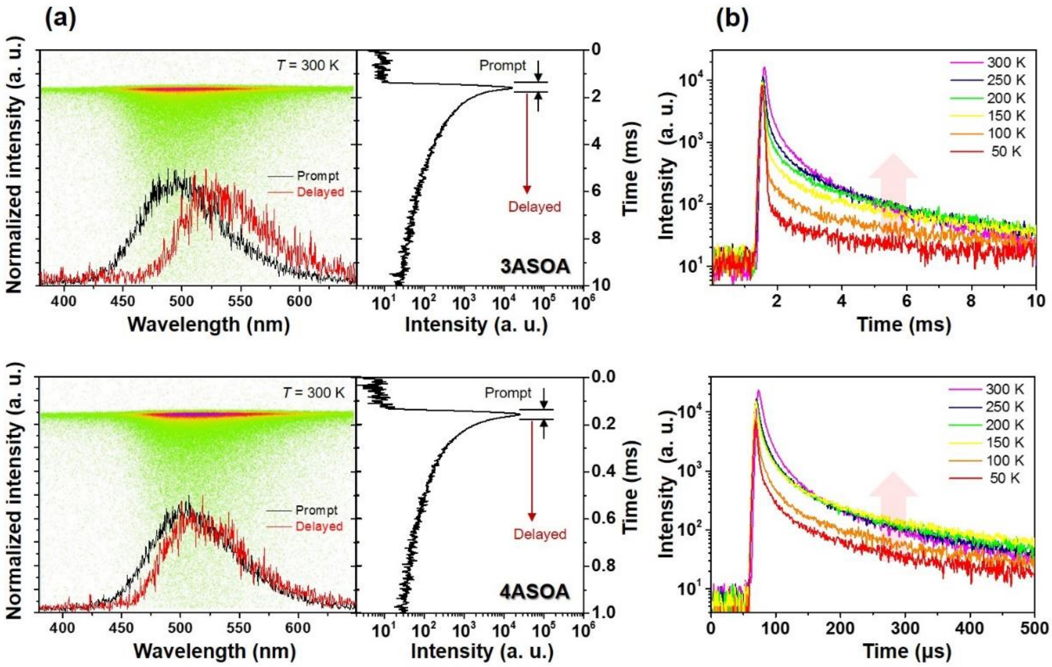

Figure 2-7. (a) Streak image of the doped films measured at 300 K under vacuum, in which green dots represent PL photon counts. (b) Temperature dependence of transient PL decay of a 6 wt%-emitter:mCP doped films.

2. 4. Electroluminescence Performance

Employing **3ASOA** and **4ASOA** as an emitter, two multi-layered OLEDs were fabricated. The materials 4,4-cyclohexylidenebis[*N*,*N*-bis(4-methylphenyl)benzenamine] (TAPC) and 1,3,5-tris(*N*-phenyl benzimidazol-2-yl)benzene (TPBi) were used as hole transport and electron transport layers, respectively. The device structures were: indium tin oxide (ITO)/TAPC (50 nm)/6 wt %-**3ASOA**:mCP (20 nm)/2,8-bis(diphenyl phosphoryl)dibenzo[*b*,*d*]thiophene (PPT) (10 nm)/TPBi (30 nm)/LiF (0.8 nm)/Al (100 nm) and ITO/TAPC (50 nm)/6 wt %-**4ASOA**:mCP (20 nm)/PPT (10 nm)TPBi (30 nm)/LiF (0.8 nm)/Al (100 nm) (**Figure 2-8**). The thin layer of PPT has a high T_1 energy, which should suppress triplet exciton quenching at the neighboring interfaces and to confine the excitons inside the emitting layers.[9]

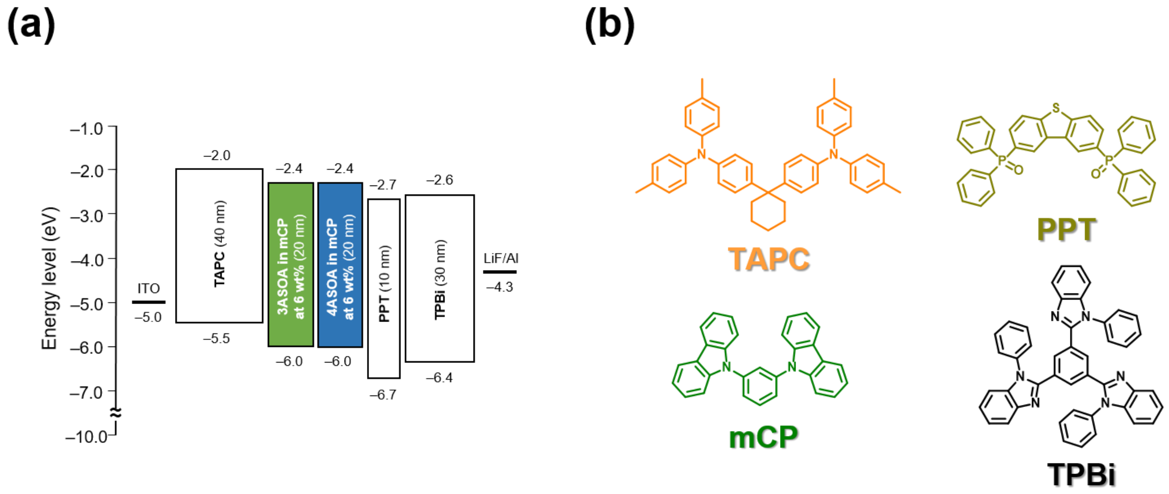

Figure 2-8. (a) Energy level diagram and (b) molecular structures of materials used for TADF-OLEDs.

All the devices employing the dibenzo[*b*,*d*]thiophene 5,5-dioxide-based emitters displayed EL spectra similar to the corresponding PL spectra, confirming that EL emission was generated solely from the emitters via the same radiative decay process. These devices indicated similar turn-on voltages (V_{on}) in the range of 4.0–4.4 V. The **3ASOA** and **4ASOA** devices exhibited EL emission peaks at 510 and 513 nm, and the EL spectra were similar to their corresponding PL spectra. In addition, Commission Internationale de l'Éclairage (CIE) color coordinates of (0.26, 0.53) were obtained (**Figure 2-9**). An EL efficiency of the **3ASOA** device was drastically decreased with increasing luminance. This severe efficiency rolloff of the device is mainly attributed to the relatively longer T_1 excited-state lifetime of the **3ASOA** emitter, which undergoes exciton quenching such as triplet–triplet annihilation and/or triplet–polaron annihilation.[10] Another possible reason can be the poor electron-transport property of the mCP host. mCP is a unipolar hole-transporting material and the hole/electron carrier balance is disrupted at high current densities. The OLED performance and rolloff behavior of the TADF device can further be improved by using suitable bipolar hosts with high T_1 values and TADF emitters with shorter triplet excited-state lifetimes. High maximum external EL quantum efficiencies (η_{ext}) with 10.4% and 13.8% were attained for the devices containing the **3ASOA-** and **4ASOA-**based OLEDs, respectively. Additionally, current efficiencies (η_c) of 21.8 cd A^{-1} and 41.2 cd A^{-1} and power efficiencies (η_p) of 15.1 lm W^{-1} and 31.5 lm W^{-1} at low current densities were obtained. However, the **4ASOA**-based device exhibited only a slight efficiency rolloff owing to its short T_1 exciton lifetime, compared to **3ASOA**. The detail EL performances of TADF-OLEDs are summarized in **Table 2-3**.

Table 2-3. EL performance of the TADF-based OLEDs.[a)]

TADF emitter	Host	λ_{EL} [nm]	V_{on} [V]	L_{max} [cd m^{-2}]	η_{ext} [%]	η_c [cd A^{-1}]	η_p [lm W^{-1}]	CIE (*x*, *y*)
3ASOA	mCP	510	4.4	385	10.4	21.8	15.1	(0.26, 0.53)
4ASOA	mCP	512	4.0	1717	13.8	41.2	31.5	(0.26, 0.53)

[a)] Abbreviations: λ_{EL} = EL emission maximum, V_{on} = turn-on voltage at 1 cd m^{-2}, L_{max} = maximum luminance, η_{ext} = maximum external EL quantum efficiency, η_c = maximum current efficiency, η_p = maximum power efficiency, CIE = Commission Internationale de l'Éclairage color coordinates measured at 10 mA cm^{-2}.

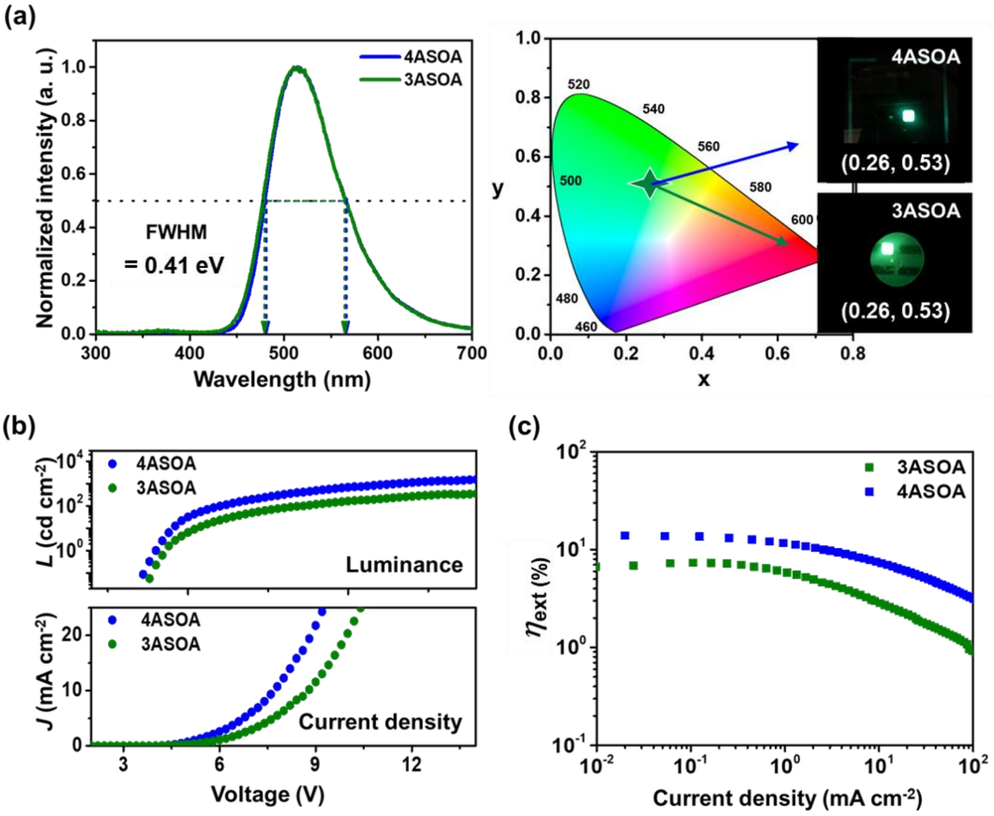

Figure 2-9. (a) Normalized EL spectra of the devices measured at 10 mA cm^{-1} (b) Current density–voltage–luminance (*J*–*V*–*L*) characteristics and (c) external EL quantum efficiency (η_{ext}) versus luminance plots of the TADF-OLEDs.

A typical rolloff behavior was observed in both OLEDs, which can be ascribed to exciton annihilation processes such as triplet-polaron and triplet-triplet interactions. **Table 2-4** summarizes the rate constants for singlet decay (k_{r}), ISC (k_{ISC}), RISC (k_{RISC}), and nonradiative decay from the triplet state (k_{nr}). **4ASOA** exhibited slightly relaxed rolloff behavior compared to **3ASOA**, which is consistent with the higher k_{RISC} than that of **3ASOA**. This result indicates that 2,8-substitution is effective for achieving the fast upconversion from triplet into singlet states, i.e., larger k_{RISC}, while maintaining high PLQY.[11] Here we note that the rolloff improvement is rather limited due to their slow k_{RISC}. The k_{RISC} values of **3ASOA** and **4ASOA** are rather small even with the relatively small ΔE_{ST} of 0.26 eV and 0.09 eV, respectively, which can be explained by some possible mechanisms. In our recent study, the upconversion process is closely related to the molecular orbital type of triplet and singlet states such as CT and LE states.[12] Also, the presence of hyperfine-coupling process[13] and vibrational coupling[14] plays an important role for the upconversion process. In next chapters, the detailed mechanism in order to realize a rapid RISC process will be discussed. Further, other factors such as charge balance and recombination width would influence the rolloff behavior and comprehensive studies will be conducted in our successive studies to relax the rolloff.

Table 2-4. Rate constant of TADF emitters in 6 wt%-**3ASOA** and **4ASOA**:mCP films.

TADF emitter	$k_r{}^a$ (10^7 S^{-1})	$k_{\mathrm{ISC}}{}^b$ (10^7 s^{-1})	$k_{\mathrm{RISC}}{}^c$ (10^2 s^{-1})	$k_{\mathrm{nr}}{}^d$ (10^1 s^{-1})
3ASOA	2.5	9.7	6.5	7.3
4ASOA	0.81	7.1	61	8.9

[a]Rate constant of radiative decay ($S_1 \rightarrow S_0$). [b]Rate constant of ISC ($S_1 \rightarrow T_1$). [c]Rate constant of RISC ($T_1 \rightarrow S_1$). [d]Rate constant of nonradiative decay ($T_1 \rightarrow S_0$).

2. 5. Experimental Section

2. 5. 1 General Methods

^{1}H and ^{13}C NMR spectra were recorded on a Varian Mercury Plus 300 MHz spectrometer in $CDCl_3$ using tetramethylsilane as an internal standard and the chemical shifts were reported in ppm relative to the signals of $CDCl_3$ at 7.26 and 77 ppm for ^{1}H and ^{13}C NMR, respectively. High-resolution mass spectrometry fast atom bombardment (HRMS (FAB)) mass spectra data were obtained from the Korea Basic Science Institute, Daejeon. The purities of the final compounds were analyzed using a HPLC instrument from Agilent Technologies. The UV−Vis absorption and fluorescence spectra were recorded at room temperature with JASCO V-570 and Hitachi F-4500 fluorescence spectrophotometers, respectively. Thermal analyses were performed on a Mettler Toledo TGA/SDTA 851e DSC 822e analyzer under a N_2 atmosphere at a heating rate of 10 °C min^{-1}. Cyclic voltammetry studies were carried out with a CHI 600C potentiostat (CH Instruments), which was equipped with a platinum disc as the working electrode, platinum wire as the counter electrode, and Ag/AgCl as the reference electrode, at a scan rate of 100 mV s^{-1} in a 0.1 M solution of tetrabutylammonium perchlorate as the supporting electrolyte in a CH_2Cl_2 solution. The potentials were referenced to the ferrocene/ferrocenium redox couple (Fc/Fc$^+$), and it was assumed that the redox potential of Fc/Fc$^+$ had an absolute energy level of −4.8 eV to vacuum. The potential of Fc/Fc$^+$ was measured under the same conditions and located at 0.09 V relative to the Ag/Ag$^+$ electrode. All electrochemical experiments were performed in ambient air at room temperature. UV–vis absorption and photoluminescence (PL) spectra were measured with a UV-2550 spectrometer (Shimadzu) and a Fluoromax-4 spectrophotometer (Horiba Scientific), respectively, using degassed spectral grade solvents. The PL quantum yields were measured using an integration sphere system C9920-02 coupled with a PMA-11 photonic multichannel analyzer (Hamamatsu Photonics). The transient PL measurements of doped thin films were performed using a C4334 Streak camera (Hamamatsu Photonics) with a N_2 gas laser (λ = 337 nm, pulse width = 500 ps, repetition rate = 20 Hz) under vacuum ($< 4 \times 10^{-1}$ Pa). The HOMO energy levels of thin films were determined using an AC-3 ultraviolet photoelectron spectrometer (Riken-Keiki). The LUMO energy levels were estimated by subtracting the optical energy gap (E_g) from the measured HOMO energies; E_g values were determined from the onset position of the PL spectra of thin films. All quantum chemical calculations were performed using the Gaussian 09 program package. Geometries in the ground state were optimized using the B3LYP functional with the 6-31G(d,p) basis set. Low-lying excited singlet and triplet states were computed using the optimized structures with time-dependent density functional theory (TD-DFT) at the same level.

2. 5. 2. Preparation of Materials

All reagents and chemicals were used without further purification unless stated otherwise, and all reactions were carefully monitored using thin layer chromatography on Merck-precoated aluminum plates. 9,9-dimethyl-9,10-dihydroacridine was prepared according to the reported procedures. Other OLED materials were purchased from Luminescence Technology Corp. All reactions were performed under nitrogen atmospheres in dry solvents. All final products were purified by temperature-gradient sublimation under vacuum before the measurements and device fabrication.

2. 5. 3. Synthesis

The synthetic schemes are outlined in **Schemes 2-1**. Compound **1** was synthesized according to the literature procedure[15]; compounds **a** and **b** were synthesized in two steps: oxidation followed by bromination on dibenzothiophene for compound **a**[16] and bromination followed by oxidation for compound **b.**[17] The **3ASOA** and **4ASOA** were synthesized to add sodium *tert*-butoxide (320 mg, 3.34 mmol) and either **a** or **b** (250 mg, 0.668 mmol) to a solution of 9,9-dimethyl-9,10-dihydroacridine (**1**) (293 mg, 1.402 mmol) in dry dioxane (15 mL). The reaction mixture was purged with N_2 for 30 min, and then $Pd(OAc)_2$ (7.5 mg, 0.033 mmol) and tri-*tert*-butylphosphine ($P(t\text{-}Bu)_3$) (13.5 mg, 0.066 mmol) were added. The resulting reaction mixture was stirred at 110 °C for 12 h under a N_2 atmosphere. Upon reaction completion, the reaction mixture was diluted with ethyl acetate and water; the organic layer was extracted and washed with water and brine solution. Finally, the organic layer was dried over Na_2SO_4 and concentrated under reduced pressure. The crude compound was purified by column chromatography on silica gel eluted with ethyl acetate/hexanes (2:8). The product was further purified by recrystallization in ethanol and triturated with CH_2Cl_2/hexanes. The compounds **3ASOA** and **4ASOA** were produced at yields of 95% and 81%, respectively.

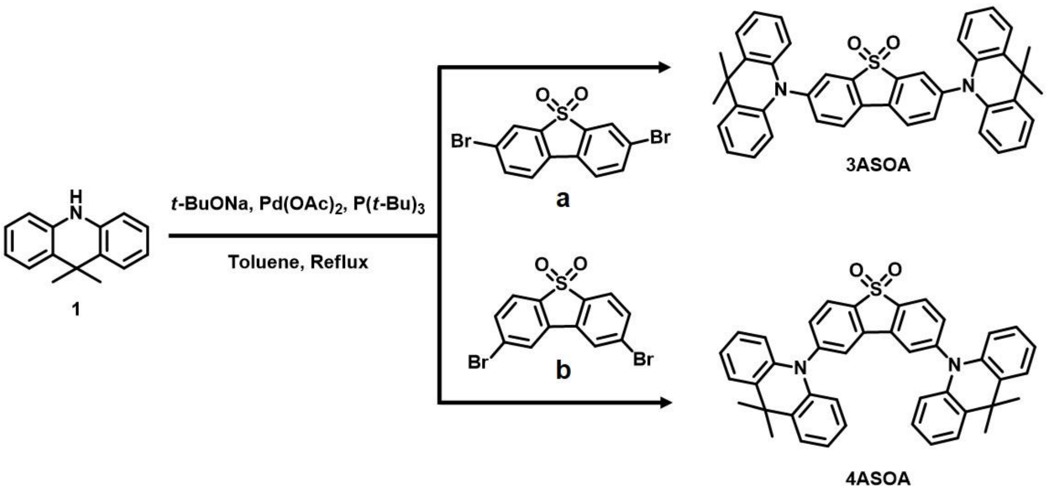

Scheme 2-1. Synthetic routes for the dibenzo[*b*,*d*]thiophene 5,5-dioxide-based TADF molecules.

All final products were purified by temperature-gradient sublimation under vacuum after column chromatography to obtain highly pure materials, which can be used for the fabrication of OLED devices by vacuum deposition. Chemical structures of the final products were confirmed by ^{1}H and ^{13}C NMR spectroscopy, matrix-assisted laser desorption ionization time-of-flight (MALDI-TOF) mass spectrometry, and elemental analysis.

Synthesis of 3,7-bis(9,9-dimethyl-9,10-dihydroacridine) dibenzo[*b*,*d*]thiophene 5,5-dioxide (3ASOA): Yellow solid. Yield: 400 mg (95%). ^{1}H NMR (300 MHz, $CDCl_3$, δ): 8.12 (d, J = 7.5 Hz, 2H), 7.91 (s, 2H), 7.71 (d, J = 7.2 Hz, 2H), 7.51–7.49 (m, 4H), 7.03–7.01 (m, 8H), 6.37 (d, J = 5.1 Hz, 4H), 1.71 (s, 12H). ^{13}C NMR (75 MHz, $CDCl_3$, δ): 144.021, 140.835, 140.207, 137.067, 131.154, 130.327, 126.635, 125.532, 125.226, 124.169, 121.703, 114.457, 36.166, 30.957. HRMS (FAB) calcd. for $C_{42}H_{34}N_2O_2S$ $[M+H]^+$ 631.24, found 631.24. Anal. calcd. for $C_{42}H_{34}N_2O_2S$: C 79.97, H 5.43, N 4.4, O 5.07, S 5.08; found C 79.99, H 5.41, N 4.1, O 5.05, S 5.06. Purity: >99.8% by HPLC.

Synthesis of 2,8-bis(9,9-dimethyl-9,10-dihydroacridine) dibenzo[*b,d*]thiophene 5,5-dioxide (4ASOA): Yellow solid. Yield: 340 mg (81%). ^{1}H NMR (300 MHz, $CDCl_3$, δ): 8.12 (d, J = 7.5 Hz, 2H), 7.71 (s, 2H), 7.59 (d, J = 7.8 Hz, 2H), 7.46 (d, J = 6.3 Hz, 4H), 7.03–6.98 (m, 8H), 6.34 (d, J = 6.3 Hz, 4H), 1.66 (s, 12H). ^{13}C NMR (75 MHz, $CDCl_3$, δ): 147.606, 139.977, 136.699, 134.264, 133.115, 131.292, 126.589, 125.609, 124.858, 123.985, 121.733, 114.672, 36.135, 31.095. HRMS (FAB) calcd. for $C_{42}H_{34}N_2O_2S$ $[M+H]^+$ 631.24, found 631.24. Anal. calcd. for $C_{42}H_{34}N_2O_2S$: C 79.97, H 5.43, N 4.4, O 5.07, S 5.08; found C 79.98, H 5.42, N 4.2, O 5.06, S 5.05. Purity: >99.8% by HPLC.

2. 5. 4. Device Fabrication and Measurements

ITO-coated glass substrates were cleaned with detergent, deionized water, acetone, and isopropanol. The substrates were then subjected to UV−ozone treatment for 15 min, before loading them into a vacuum evaporation system. The organic layers were thermally evaporated on the substrates under vacuum ($< 3 \times 10^{-4}$ Pa) with an evaporation rate of < 0.3 nm s^{-1}. A cathode aluminum layer was then deposited through a shadow mask. The layer thickness and the deposition rate were monitored *in situ* during deposition by an oscillating quartz thickness monitor. The current density–voltage–luminance (J−V−L) characteristics of the devices were measured using an E5273A semiconductor parameter analyzer (Agilent) and a 1930-C optical power meter (Newport). The EL spectra were recorded using an SD2000 multi-channel analyzer (Ocean Optics).

2. 6. Conclusion

A new green TADF emitters have been designed and synthesized by combining a dibenzo[*b,d*]thiophene 5,5-dioxide acceptor core with 9,9-dimethyl-9,10-dihydroacridine donor units. The photophysical and EL properties were tuned by a rational substituted position of the donors in dibenzo[*b,d*]thiophene 5,5-dioxide derivatives. The OLEDs based on these TADF emitters exhibited the maximum external EL quantum efficiencies of 10.4% and 13.8%, respectively, with the slightly relaxed rolloff behavior with **4ASOA**. The TADF emission behavior of the doped films and OLED performance were largely depended on k_{RISC}, indicating that a delicate tuning of donor and acceptor arrangement surely enhances TADF properties.

References

[1] Q. Zhang, B. Li, S. Huang, H. Nomura, H. Tanaka, C. Adachi, *Nat. Photon*., **2014**, 8, 1–7.

[2] F. B. Dias, K. N. Bourdakos, V. Jankus, K. C. Moss, K. T. Kamtekar, V. Bhalla, J. Santos, M. R. Bryce, A.P. Monkman, *Adv. Mater*., **2013**, 25, 3707–3714.

[3] I. S. Park, M. Numata, C. Adachi, T. Yasuda, *Bull. Chem. Soc. Jpn*., **2016**, 89, 375–377.

[4] I. S. Park, S. Y. Lee, C. Adachi, T. Yasuda, *Adv. Funct. Mater*., **2016**, 26, 1813–1821.

[5] M. J. Frisch, G. W. Trucks, H. B. Schlegel, G. E. Scuseria, M. A. Robb, J. R. Cheeseman, G. Scalmani, V. Barone, B. Mennucci, G. A. Petersson, H. Nakatsuji, M. Caricato, X. Li, H. P. Hratchian, A. F. Izmaylov, J. Bloino, G. Zheng, J. L. Sonnenberg, M. Hada, M. Ehara, K. Toyota, R. Fukuda, J. Hasegawa, M. Ishida, T. Nakajima, Y. Honda, O. Kitao, H. Nakai, T. Vreven, J. A. Montgomery, Jr., J. E. Peralta, F. Ogliaro, M. Bearpark, J. J. Heyd, E. Brothers, K. N. Kudin, V. N. Staroverov, R. Kobayashi, J. Normand, K. Raghavachari, A. Rendell, J. C. Burant, S. S. Iyengar, J. Tomasi, M. Cossi, N. Rega, J. M. Millam, M. Klene, J. E. Knox, J. B. Cross, V. Bakken, C. Adamo, J. Jaramillo, R. Gomperts, R. E. Stratmann, O. Yazyev, A. J. Austin, R. Cammi, C. Pomelli, J. W. Ochterski, R. L. Martin, K. Morokuma, V. G. Zakrzewski, G. A. Voth, P. Salvador, J. J. Dannenberg, S. Dapprich, A. D. Daniels, Ö. Farkas, J. B. Foresman, J. V. Ortiz, J. Cioslowski, D. J. Fox, *Gaussian 16*, Rev. B.01, Gaussian, Inc., Wallingford, CT, **2016**.

[6] S. Haseyama, A. Niwa, T. Kobayashi, T. Nagase, K. Goushi, C. Adachi, H. Naito, *Nanoscale Res. Lett*., **2017**, 12, 1–5.

[7] G. Méhes, K. Goushi, W. J. Potscavage, Jr., C. Adachi, *Org. Elect.,* **2014**, 15, 2027–2037.

[8] R. Ishimatsu, S. Matsunami, K. Shizu, C. Adachi, K. Nakano, T. Imato, *J. Phys. Chem. A*, **2013**, 117, 5607–5612.

[9] W. J. Park, Y. Lee, J. Y. Kim, D. W. Yoon, J. Kim, S. H. Chae, H. Kim, G. Lee, S. Shim, J.H. Yang, S. J. Lee, *Synth. Met*., **2015**, 209, 99–104.

[10] M. A. Baldo, C. Adachi, S. R. Forrest, *Phys. Rev. B*, **2000**, 62, 10967–10977.

[11] K. Masui, H. Nakanotani, C. Adachi, *Org. Elect.*, **2013**, 14, 2721–2726.

[12] T. Hosakai, H. Matsuzaki, H. Nakanotani, K. Tokumaru, T. Tsutsui, A. Furube, K. Nasu, H. Nomura, M. Yahiro, C. Adachi, *Sci. Adv.*, **2017**, 3, 1603282.

[13] T. Ogiwara, Y. Wakikawa, T. Ikoma, *J. Phys. Chem. A*, **2015**, 119, 3415–3418.

[14] J. Gibson, A.P. Monkman, T.J. Penfold, *Chem. Phys. Chem.*, **2016**, 17, 2956–2961.

[15] S. S. Reddy, V. G. Sree, K. Gunasekar, W. Cho, Y.-S. Gal, M. Song, J.-W. Kang, S-H. Jin, *Adv. Optical Mater.*, **2016**, 8, 1236–1246.

[16] I. I. Perepichka, I. F. Perepichka, M.R. Bryce, L.-O. Pålsson, *Chem. Commun.*, **2005**, 1, 3397–3399.

[17]] J. Liu, J. Zou, W. Yang, H. Wu, C. Li, B. Zhang, J. Peng, Y. Cao, *Chem. Mater.*, **2008**, 20, 4499–4506.

Chapter 3

High-Triplet-Energy Bipolar Host Molecules for Sky-Blue Thermally Activated Delayed Fluorescence Organic Light-Emitting Diodes with Reduced Efficiency Rolloff

3. 1. Introduction

For blue TADF-based OLEDs, there are some general requirements for the host material: (1) the E_T of host materials must be higher than that of the blue TADF emitter to prevent back energy transfer[1]; (2) to facilitate effective charge injection, both the HOMO and LUMO energy levels of the host materials should be well matched with both those of the emitter and the other layers of the device[2]; (3) a good host material should possess ambipolar character to best manage charge transport through the emissive layer.[3,4] In general, the recombination region tends to occur closer to the emissive layer/electron-transporting layer (EML/ETL) interface when using hole-transporting (HT) hosts such as mCP and 9-[4-(1,1-dimethylethyl)phenyl]-3,6-bis(triphenylsilyl)-9*H*-carbazole (CzSi). Likewise, the recombination region is likely to be located in the EML/HTL interface when using an electron-transporting (ET) host such as the frequently used bis[2-(diphenylphosphino)phenyl] ether oxide (DPEPO). It has been found that poor and unbalanced carrier mobility within the EML is responsible for inferior efficiencies, low stability and high efficiency rolloff of blue-emitting OLEDs.[5] OLEDs with narrow charge recombination zones lead to devices presenting severe efficiency rolloff due to the local accumulation of high-density triplet excitons, especially at high current densities. The populated triplet excitons further induce triplet-triplet annihilation (TTA), which is destructive to the devices.[6-8] In fact, it has also been demonstrated that the recombination region is widened and the device efficiency is improved by using an exciplex host system.[9,10] As a result, an ambipolar host is more suitable for improving the device performance in deep-blue and pure blue OLEDs. The simple incorporation of both HT and ET moieties within host materials should give rise to ambipolar host materials. It is confirmed that deep-blue and blue devices based on ambipolar hosts lead to improved device performances.[11-14]

DPEPO is the most popular host material for deep-blue and blue-emitting OLEDs.[15] However, the use of such ET-type host materials is usually coupled with reduced device stability and enhanced efficiency rolloff.[16-19] Thus, in this study, two host materials, **CzPO** and **Cz3PO**, by linking carbazole donor units with an electron-accepting triphenylphosphine oxide group were designed **(Figure 3-1)**. Both hosts show high E_T values of 3.1 eV that are comparable to **DPEPO**, combined with a deep HOMO level of –5.9 eV and ambipolar charge transport properties. Sky-blue OLEDs based on these two bipolar host materials not only showed smaller efficiency rolloff characteristics but also operated under relatively low driving voltages, whereas unipolar DPEPO-based device showed a severe efficiency rolloff at high current densities.

3. 2. Molecular Geometric and Electronic Structures

The energy levels of **CzPO** and **Cz3PO** were first investigated computationally using the Gaussian 16 program package.[20] Ground-state geometries in the gas phase were optimized at the PBE0/6-31G(d) level, and the lowest singlet and triplet excited states were calculated using time-dependent density functional theory (TD-DFT) based on the optimized ground-state geometries. The electron density distribution of the HOMOs and LUMOs of **CzPO** and **Cz3PO** are depicted in **Figure 3-1** along with their energies and the energies of the singlet and triplet excited states and the spin density distributions of the T_1 states.

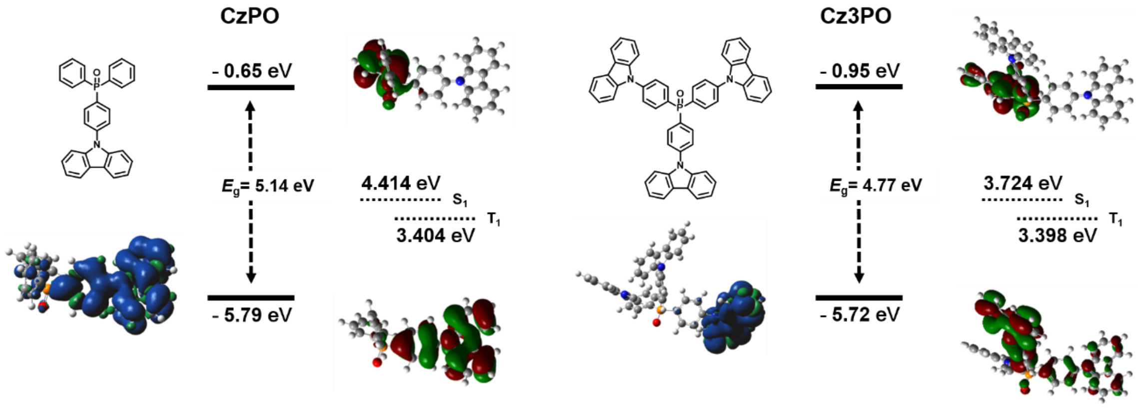

Figure 3-1 Molecular structures, HOMO, LUMO, S_1 and T_1 energy levels of host materials **CzPO** and **Cz3PO** characterized by DFT calculations at the PBE0/6-31G(d) level of theory, and the electron density distributions of the frontier molecular orbitals and spin density distributions of the lowest triplet excited state.

The HOMOs of both host materials are delocalized over the electron-donating carbazole units and bridging phenylene while the LUMOs are mainly localized over the electron-accepting phosphine oxide moiety. Owing to the presence of three donor groups, the LUMO in **Cz3PO** is stabilized at –0.95 eV compared to that of **CzPO** (–0.65 eV). The HOMO energies are similar at –5.79 and –5.72 eV for **CzPO** and **Cz3PO**, respectively. Thus, the distribution of the frontier molecular orbitals describes the ambipolar character of the host materials. The T_1 excited states of **CzPO** and **Cz3PO** are mainly localized on their corresponding carbazole units; there is more pronounced spin–density delocalization onto the bridging phenylene in **CzPO**. Both hosts show nearly identical triplet energies of 3.40 eV.

3. 3. Photophysical Properties

The UV–Vis absorption and photoluminescence (PL) spectra of **CzPO**, **Cz3PO**, and **DPEPO** in toluene solutions (10^{-5} M) and in neat films at 298 K are shown in **Figure. 3-2a** and **2b**, respectively. The photophysical data are summarized in **Table 3-1**.

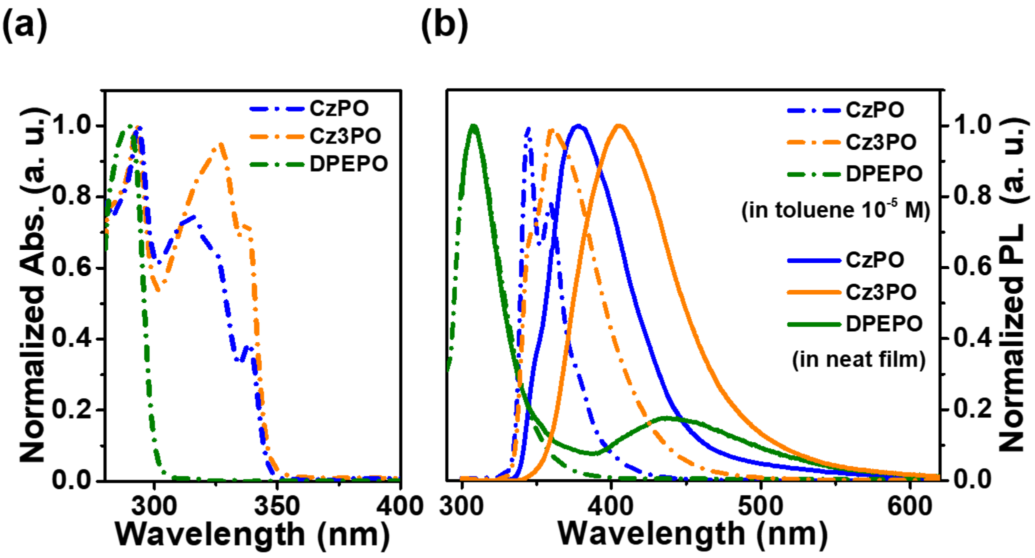

Figure 3-2. UV–Vis absorption spectra of **CzPO** (blue dash dot), **Cz3PO** (orange dash dot) and **DPEPO** (green dash dot) in toluene (10^{-5} M) and (b) PL emission spectra of **CzPO** (blue dash dot), **Cz3PO** (orange dash dot) and **DPEPO** (green dash dot) in toluene (10^{-5} M) (excitation wavelength: 290 nm) and **CzPO** (blue line), **Cz3PO** (orange line) and **DPEPO** (green line) as neat films (excitation wavelength : 280 nm).

Table 3-1. Summary of photophysical characteristics of **CzPO**, **Cz3PO**, and **DPEPO**.

Compound	λ_{abs} [nm] sol^{a)}	λ_{PL} [nm] sol^{a)} / film^{b)}	Φ_{PL}[%]^c sol^{a)} / film^{b)}	τ_p [ns]^{d)} / τ_d [μs]^{d)}	HOMO^{e)} [eV]	LUMO^{f)} [eV]	E_S / E_T [eV]^{g)}
CzPO	292, 315, 338	344, 359 / 377	64 / 81	12 / 3.1	−5.9	−2.0	3.92 / 3.06
Cz3PO	292, 327, 339	361 / 406	55 / 75	10 / 2.8	−5.9	−2.0	3.86 / 3.05
DPEPO	290	308 / 308, 437	- / 92	12 /2.6	−6.1	−2.0	4.27 / 3.87

a) Measured in oxygen-free toluene at room temperature (298 K); b)6 wt%-doped thin film in a host matrix; c)Absolute PLQY evaluated using an integrating sphere under a nitrogen atmosphere; d)PL lifetimes of prompt (τ_p) and delayed (τ_d) decay components for the 6 wt% of **CzTRZ2**-doped film at 298 K; e)Determined by atmospheric photoelectron spectroscopy of neat films; f)Deduced from the HOMO and optical energy gap (E_g) with LUMO = HOMO + E_g; g)Singlet (E_S) and triplet (E_T) energies determined from wavelengths of the emission spectra at 300 K and 77 K in toluene, respectively.

In toluene, all host materials show strong absorption bands below 300 nm, which are assigned as π–π^* transitions of the phosphine oxide moiety. The absorption band beyond 300 nm is absent in **DPEPO**, and the lowest-energy absorption bands ranging from 310 to 350 nm are attributed to the π–π^* transition of the 9-phenylcarbazole unit in **CzPO** and **Cz3PO**. In toluene, **CzPO** shows emission maxima (λ_{PL}) at 344 and 359 nm, while **Cz3PO** shows λ_{PL} at 361 nm. **DPEPO** shows the most hypsochromicly shifted emission at 290 nm. The bathochromicly shifted emission in **Cz3PO** is due to the presence of three donor groups within the molecule. Both hosts show high PL quantum yields (Φ_{PL}), in degassed toluene of 64% and 55% for **CzPO** and **Cz3PO**, respectively. In neat films, only **CzPO** and **Cz3PO** display red-shifted emission at 377 and 406 nm, respectively, whereas **DPEPO** shows an additional emission band at 437 nm that may be ascribed to excimer emission. In the present study, **CzTRZ2** (9-(4-(4,6-diphenyl-1,3,5-triazin-2-yl)phenyl)-1,3,6,8-tetramethyl-9*H*-carbazole) was used as the blue TADF emitter in the emitting layer as the absorption spectrum of **CzTRZ2** overlaps strongly with the neat film emission spectra of **CzPO** and **Cz3PO**, thereby assuring efficient Förster resonance energy transfer (FRET) from the excited hosts to **CzTRZ2**.

The phosphorescence spectra of **CzPO**, **Cz3PO**, and **DPEPO** in frozen toluene matrices at 77 K are depicted in **Figure 3-3a** and these are cross-compared with the phosphorescence spectra of *N*-phenylcarbazole and triphenylphosphine oxide (**Figure 3-3b**), which act as reference electron-donor and electron-acceptor moieties. From the phosphorescence spectra, the E_T values were determined to be 3.06 and 3.05 eV for **CzPO** and **Cz3PO**, respectively. The E_T of **CzPO** and **Cz3PO** are higher than that of **CzTRZ2** (2.85 eV) [21], ensuring a suppression of back energy transfer. Both **CzPO** and **Cz3PO** show similar vibronic-structured emission profiles and E_T to that of *N*-phenylcarbazole. Therefore, the lowest T_1 excited state of each of **CzPO** and **Cz3PO** is localized on the donor moieties, consistent with the computed spin density simulation. The PL spectra of 6 wt%-**CzTRZ2** doped films in **CzPO, Cz3PO**, and **DPEPO** are nearly identical, indicating efficient FRET (**Figure. 3-4a**). The **CzPO-**, **Cz3PO-**, and **DPEPO-**doped films of **CzTRZ2** show broad and structureless sky-blue emission with high Φ_{PL} of 81%, 75%, and 92%, respectively.

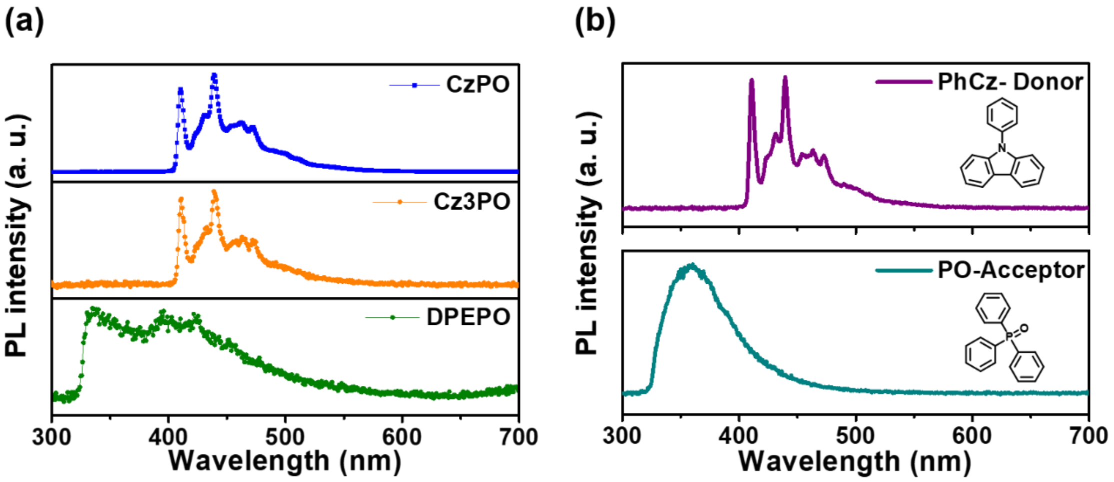

Figure 3-3. (a) Phosphorescence spectra of **CzPO**, **Cz3PO,** and **DPEPO** in toluene matrices at 77 K. (b) Phosphorescence spectra of donor and acceptor moieties in toluene matrices at 77 K.

The transient decay profiles of **CzPO-**, **Cz3PO-**, and **DPEPO-**doped films of **CzTRZ2** clearly show biexponential decay characteristics with prompt fluorescence lifetimes (τ_p) of 12, 10, and 12 ns and delayed fluorescence lifetimes (τ_d) of 3.1, 2.8, and 2.6 μs, respectively, at 298 K (**Figure 3-4b**). Such behavior is characteristics of the TADF emission previously reported for this compound.

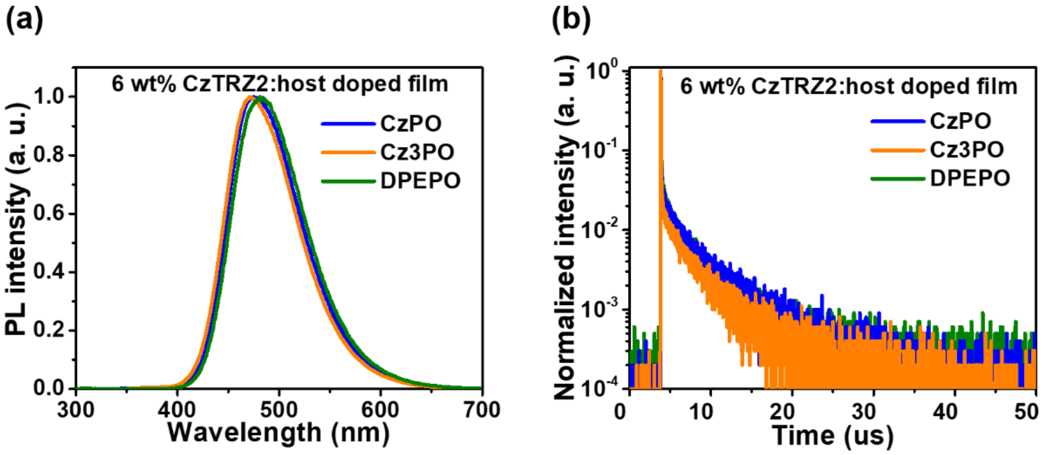

Figure 3-4. (a) Steady-state PL spectra and (b) time-resolved PL decay profiles of 6 wt%-**CzTRZ2**:host doped thin films (host = **CzPO**, **Cz3PO**, and **DPEPO**) measured at 298 K under N_2. (excitation wavelength: 280 nm)

Furthermore, both hosts materials possess a high decomposition temperature (T_d) of 365 and 454 °C, for **CzPO** and **Cz3PO**, respectively, which is indicative of high thermal and morphological stabilities. The T_d values are substantially higher than that of DPEPO (T_d = 322 °C).[22]

3. 4. Electroluminescence Performance

The EL performance of OLEDs using **CzTRZ2** as the TADF emitter and **CzPO**, **Cz3PO**, and **DPEPO** as host matrices in the EML were evaluated (**Figure 3-5a**).

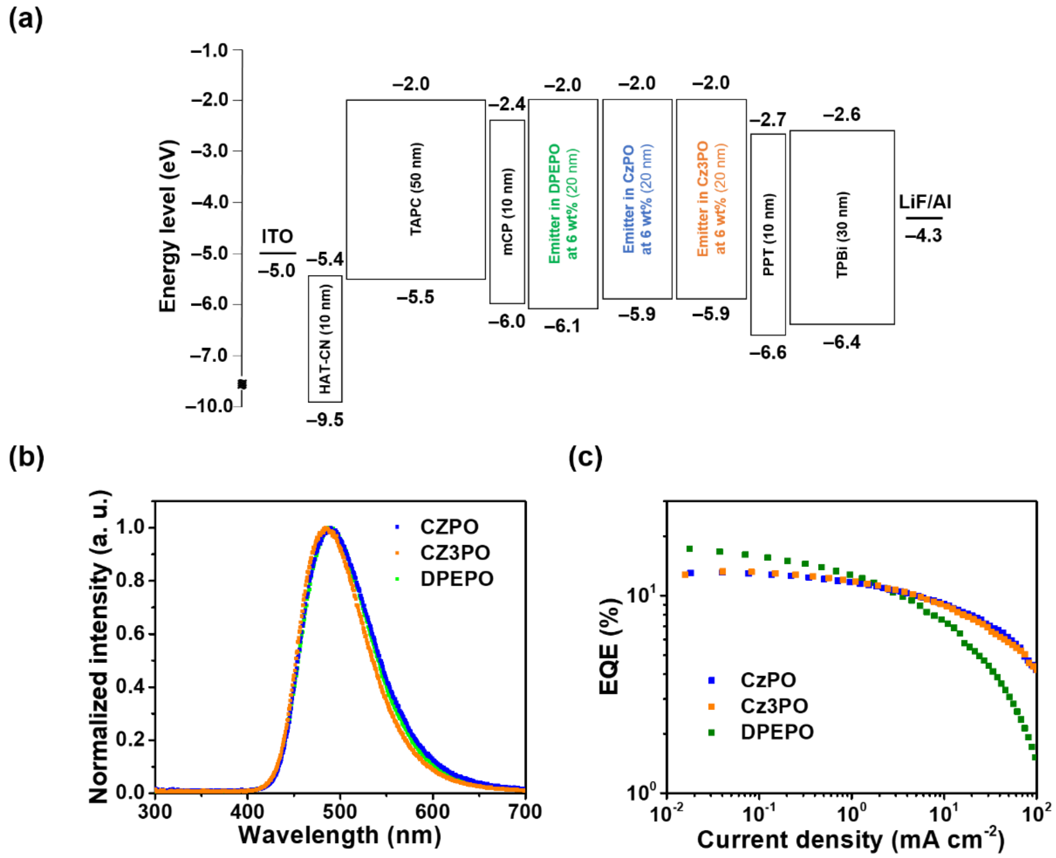

Figure 3-5. (a) Energy-level diagram of **CzTRZ2-**based TADF-OLEDs hosted by **CzPO**, **Cz3PO** and **DPEPO**. (b) The EL spectra measured at 8 V, and (c) external quantum efficiency (η_{ext})–current density curves of the TADF-based OLEDs.

The devices were fabricated with the following architecture (**Figure 3-5a**): ITO (100 nm)/HATCN (10 nm)/TAPC (40 nm)/mCP (10 nm)/6 wt%-**CzTRZ2**:host (20 nm)/PPT (10 nm)/TPBi (50 nm)/LiF (0.8 nm)/Al (100 nm), in which 2,3,6,7,10,11-hexacyano-1,4,5,8,9,12-hexaazatriphenylene (HATCN) is the hole-injection layer, 1,1-bis(4-ditolylaminophenyl) cyclohexane (TAPC) and 1,3-bis(*N*-carbazolyl)benzene (mCP) are the hole-transporting layer and electron-blocking layer, respectively. The EML layer consists of 6 wt% of **CzTRZ2** doped in **CzPO, Cz3PO** or **DPEPO**. 2,8-Bis(diphenylphosphoryl)dibenzothiophene (PPT) is the hole-blocking layer and 1,3,5-tris(*N*-phenylbenzimidazol-2-yl)benzene (TPBi), LiF and Al serve as the electron-transporting layer, the electron-injection layer and cathode, respectively. The E_T of electron-blocking and hole-blocking layers, i. e., mCP (2.9 eV) and PPT (2.9 eV), respectively, are higher than that of **CzTRZ2**, which ensures confinement of the triplet excitons within the EML. The EL spectra and EQE characteristics of the corresponding OLEDs are shown in **Figure 3-5b**.

There was no EL spectral shift at various operating voltages for all three devices, which indicates an excellent exciton confinement in the EML (**Figure. 3-6**). Devices based on **CzPO** and **Cz3PO** as host materials resulted in maximum exteran EL quantum efficiencies (η_{ext}) of 13.1 and 13.2% together with maximum current efficiencies (η_c) of 31.2 and 29.4 cd A^{-1}, and maximum power efficiencies (η_p) of 22.2 and 23.1 lm W^{-1}, respectively. By contrast, the device based on **DPEPO** showed a higher maximum η_{ext} of 16.7% with a maximum η_c of 38.4 cd A^{-1} and a maximum η_p of 26.2 lm W^{-1}. Despite the higher η_{ext}, η_c, and η_p, the **DPEPO**-based devices showed a significantly worse efficiency rolloff with an η_{ext} of only 1% at 100 mA cm^{-2}. Meanwhile, the **CzPO**- and **Cz3PO**-based devices exhibited reduced efficiency rolloff with η_{ext} of 4.2% and 4.2%, respectively, at a display-relevant current density of 100 mA cm^{-2}. All the device data are shown in **Table 3-2**.

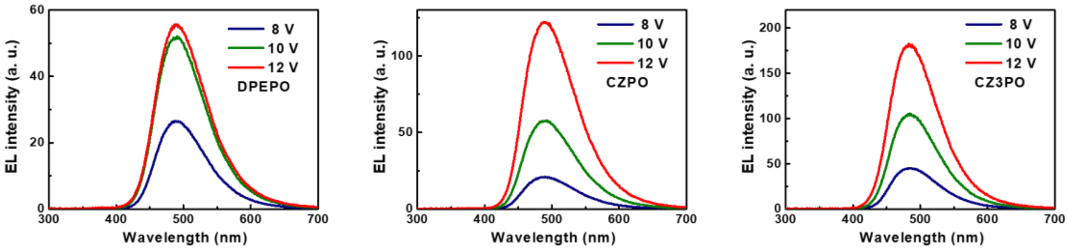

Figure 3-6 EL spectral changes of the 6 wt%- **CzTRZ2** doped into **CzPO**, **Cz3PO** and **DPEPO** host materials at different operating voltages.

Thanks to the enhanced carrier balance and efficient energy transfer in EML, the **CzPO**- and **Cz3PO** based devices displayed the relaxed efficiency rolloff behavior compared with the DPEPO-based device.

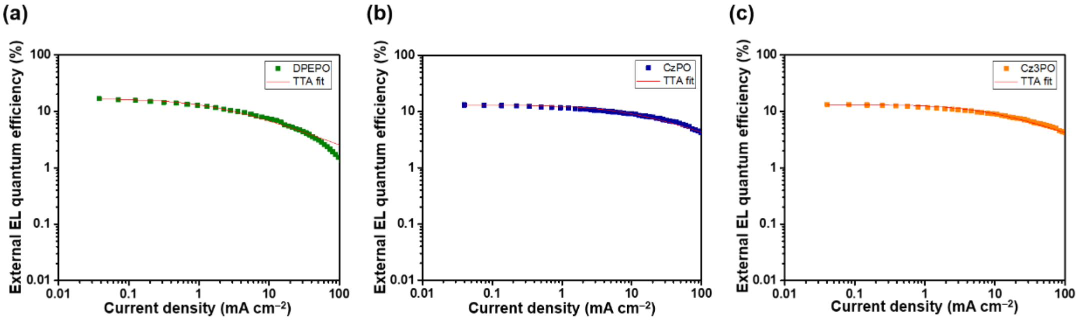

Figure 3-7. External EL quantum efficiencies (η_{ext}) for the devices based on **DPEPO** (a), **CzPO** (b), and **Cz3PO** (c) as a function of current density and the fitting results according to the triplet–triplet annihilation (TTA, red lines) mechanism.

TTA simulations studied with the η_{ext} –J curves for the **CzPO-**, **Cz3PO-**, and **DPEPO-**based devices are shown in **Figure 3-7**. TTA simulations matched well with the η_{ext} –J curves for devices **CzPO** and **Cz3PO**, which suggests that the TTA mechanism mainly accounts for efficiency rolloff of both the devices. On the other hand, significant efficiency rolloff was observed in **DPEPO**-based device, suggesting the presence of additional exciton annihilation process in addition to TTA.

Table 3-2. Summary of EL performance of TADF-based OLEDs for 6 wt% **CzTRZ2:**host as **EML.**$^{a)}$

Bipolar Host	λ_{EL} [nm]	V_{on} [V]	L_{max} [cd m^{-2}]	η_{ext} [%]	η_c [cd A^{-1}]	η_p [lm W^{-1}]	CIE (x, y)
CzPO	489	3.8	1,326	13.1	31.2	22.2	(0.19, 0.38)
Cz3PO	483	4.0	1,852	13.2	29.4	23.1	(0.18, 0.35)
DPEPO	495	4.6	453.1	16.7	26.3	38.4	(0.19, 0.37)

$^{a)}$Abbreviations: λ_{EL} = EL emission maximum, V_{on} = turn-on voltage at 1 cd m^{-2}, L_{max} = maximum luminance, η_{ext} = maximum external EL quantum efficiency, η_c = maximum current efficiency, η_p = maximum power efficiency, CIE = Commission Internationale de l'Éclairage color coordinates measured at 10 mA cm^{-2}.

To investigate the reason for the reduced rolloff characteristics, hole-only devices (HODs) and electron-only devices (EODs) with different host materials were fabricated to evaluate the carrier transporting properties of the corresponding OLEDs.[23] These device configurations were: ITO/HAT-CN (10 nm)/TAPC (20 nm)/ host (60 nm)/TAPC (20 nm)/Al (100 nm) for the HODs and ITO/TPBi (20 nm)/host (60 nm)/TPBi (20 nm)/LiF (0.8 nm)/Al (100 nm) for the EODs. **Figure 3-8** showed the J–V curves of the fabricated HODs and EODs.

For the HODs (**Figure 3-8a**), the **Cz3PO** and **Cz3PO**-based devices showed hole transporting/injection properties due to the presence of more electron-donating carbazole units, while no significant electron current was observed in **DPEPO**-based device. In contrast, for EODs, the order of the electron transporting/injection properties of devices was **DPEPO** > **CzPO** > **Cz3PO** (**Figure 3-8b**). From both the HODs and EODs characteristics, **CzPO** and **Cz3PO** were confirmed to be ambipolar in nature, in which **CzPO-** and **Cz3PO**-based devices exhibited balanced hole and electron transporting/injection properties. Thus, the well-balanced charge flux and broad distribution of the charge-recombination zones within the EML resulted in low efficiency rolloff characteristics for **CzPO-** and **Cz3PO-**based OLEDs. At this moment, it is rather hard to mention which one is superior as a host. In future study, I think that OLED stability test will distinguish the difference of these hosts.

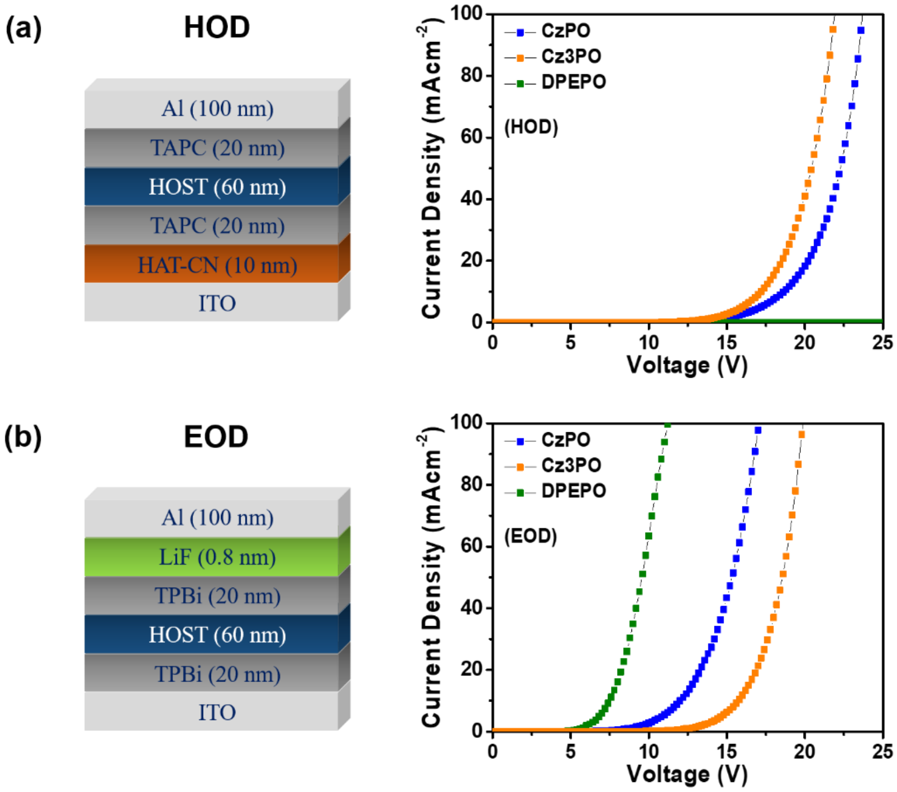

Figure 3-8. Current density–voltage (*J*–*V*) characteristics of (a) hole-only devices (HODs) and (b) electron-only devices (EODs) based on the **CzPO**, **Cz3PO**, and **DPEPO** hosts.

3. 5. Experimental Section

3. 5. 1. General Methods

Quantum chemical calculations were performed using the Gaussian 16 program package. The molecular geometries in the ground state were optimized using the PBE0 functional with the 6-31G(d) basis set in the gas phase. The lowest singlet and triplet excited states were computed using the optimized structures with time-dependent density functional theory (TD-DFT) at the same level. NMR spectra were recorded on Bruker Avance III 400 and 500 spectrometers. Chemical shifts of ^{1}H and ^{13}C NMR signals were quoted to tetramethylsilane (δ = 0.00), $CDCl_3$ (δ = 77.0), and DMSO-d_6 (δ = 39.5) as internal standards, respectively. Matrix-assisted laser desorption ionization time-of-flight (MALDI-TOF) mass spectra were collected on a Bruker Daltonics Autoflex III spectrometer using dithranol as the matrix. Elemental analyses were carried out with a Yanaco MT-5 CHN corder. Density functional theory (DFT) calculations for the pyrimidine-based molecules were performed using the Gaussian 09 program package. Geometries in the ground state were optimized using the PBE0 functional with the 6-31G(d) basis set. The lowest singlet and triplet excited states were computed using the optimized structures with time-dependent DFT (TD-DFT) at the same level. Organic thin films for photophysical measurements were prepared by vacuum deposition under high vacuum (~ 7×10^{-5} Pa) onto a quartz glass or Si (100) substrate. UV−vis absorption and photoluminescence (PL) spectra were measured with a Jasco V-670 spectrometer and a Jasco FP-8600 spectrophotometer, respectively, using degassed spectral grade solvents. The absolute PL quantum yields (Φ_{PL}) were measured using a Jasco ILF-835 integrating sphere system. The transient PL characteristics of the doped thin films were performed using a Quantaurus-Tau C11367-01 (λ_{ex} = 340 nm, pulse width = 100 ps, and repetition rate = 20 Hz) under N_2 atmosphere, and a Hamamatsu Photonics C9300 streak camera with an N_2 gas laser (λ_{ex} = 337 nm, pulse width = 500 ps, and repetition rate = 20 Hz) under vacuum (< 4×10^{-1} Pa). The HOMO energy levels of the materials in thin films were determined using a Riken-Keiki AC-2 ultraviolet photoelectron spectrometer. The LUMO energy levels were estimated by subtracting the optical energy gap (E_g) from the measured HOMO energies; E_g values were determined from the high energy onset position of the PL spectra of the thin films.

3. 5. 2. Preparation of Materials

All regents and solvents were purchased from Sigma-Aldrich, Tokyo Chemical Industry (TCI), or Wako Pure Chemical Industries, and used as received unless otherwise noted. Other

OLED materials were purchased from E-Ray Optoelectronics Technology corporation and used for the device fabrication without further purification. The detailed synthetic procedures and characterization data for compounds are described in **Schemes 3-1**.

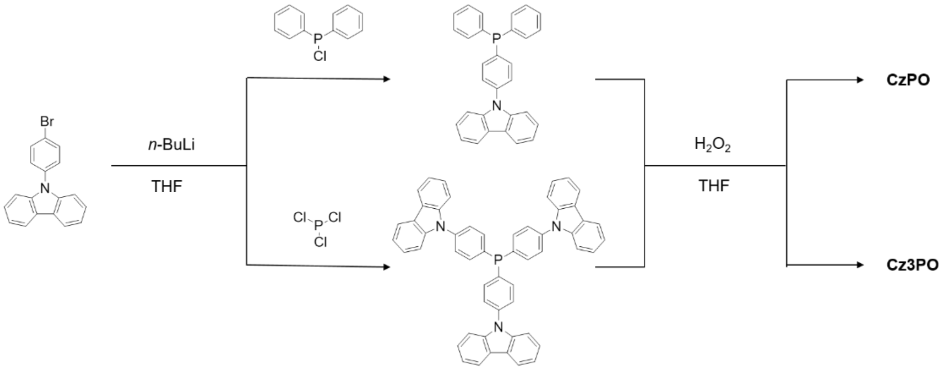

Scheme 3-1. Synthetic routes for two bipolar host materials.

3. 5. 3. Synthesis

The synthetic routes for **CzPO** and **Cz3PO** are outlined in **Scheme 3-1**. These final products were purified by temperature-gradient vacuum sublimation. Chemical structures of these compounds were characterized by ^{1}H and ^{13}C nuclear magnetic resonance (NMR) spectroscopy, matrix-assisted laser desorption ionization time-of-flight (MALDI-TOF) mass spectrometry, and elemental analysis.

Synthesis of (4-(9*H*-carbazol-9-yl)phenyl)diphenylphosphine oxide (CzPO): *n*-BuLi (2.5 M in hexanes, 4.0 mL, 10.1 mmol, 1.01 equiv.) was added dropwise to a solution of compound **1** (3.2 g, 10.0 mmol, 1 equiv.) in THF (30 mL) at −78 °C. Reaction mixture was stirred at same temperature for 30 min before quenching with chlorodiphenylphoshine (1.3 mL, 11.0 mmol, 1.1 equiv.). Reaction mixture allowed to warm up to room temperature and stirred for another 1h before adding H_2O_2 (30% v/v solution, 4.0 mL, 40.0 mmol, 4 equiv.) and then left for stirring at room temperature for overnight. Reaction mixture was diluted with water (50 mL) and extracted with DCM (75 mL). Combined organic layers were washed with brine and dried over anhydrous Na_2SO_4. Residue was purified by column chromatography (silica gel, eluent: 0−5% MeOH/DCM) to afford title compound. White crystalline solid. Yield: 2.66g, 60%. ^{1}H NMR (500 MHz, DMSO-d_6, ppm) δ: 8.26 (d, J = 7.7 Hz, 1H), 7.94 – 7.83 (m, 2H), 7.75 (dd, J = 11.7, 7.8 Hz, 2H), 7.68 (t, J = 7.2 Hz, 1H), 7.61 (t, J = 7.3 Hz, 2H), 7.52 (d, J = 8.2 Hz, 1H), 7.45 (t, J = 7.6 Hz, 1H), 7.32 (t, J = 7.4 Hz, 1H).^{13}C NMR (101 MHz, DMSO d_6, ppm) δ: 140.66, 140.63, 139.99, 134.03, 133.93, 133.54, 132.67, 132.52, 132.36, 132.13, 132.03, 131.34, 129.43, 129.31, 127.00, 126.89, 123.56, 121.08, 110.31. ^{31}P NMR (162 MHz, DMSO d_6, ppm) δ: 25.14. HR-MS (ESI) $[M+H]^+$ for ($C_{30}H_{22}NOP$) Calculated: 444.1517; Found: 444.1516.

Synthesis of tris(4-(9*H*-carbazol-9-yl)phenyl)phosphine oxide (Cz3PO): *n*-BuLi (2.5 M in hexanes, 2.6 mL, 6.3 mmol, 1.01 equiv.) was added dropwise to a solution of compound **1** (2.0 g, 6.12 mmol, 1 equiv.) in THF (20 mL) at −78 ºC. Reaction mixture was stirred at same temperature for 30 min before quenching with trichlorophoshine (0.18 mL, 2.02 mmol, 0.3 equiv.). Reaction mixture allowed to warm up to room temperature and stirred for another 1h before adding H_2O_2 (30% v/v solution, 0.5 mL, 4.04 mmol, 0.6 equiv.) and then left for stirring at room temperature for overnight. Reaction mixture was diluted with water (50 mL) and extracted with DCM (75 mL). Combined organic layers were washed with brine and dried over anhydrous Na_2SO_4. Residue was purified by column chromatography (silica gel, eluent: 0−5% MeOH/DCM) to afford title compound. White crystalline solid. Yield: 0.9 g, 56 %. R_f: 0.5 (5% MeOH/DCM). Mp: 320 ºC. ^{1}H NMR (500 MHz, DMSO-d_6, ppm) δ 8.28 (d, J = 7.7 Hz, 1H), 8.16 (dd, J = 11.3, 8.4 Hz, 1H), 8.01–7.96 (m, 1H), 7.60 (d, J = 8.3 Hz, 1H), 7.47 (t, J = 7.7 Hz, 1H), 7.34 (t, J = 7.4 Hz, 1H). ^{13}C NMR (101 MHz, DMSO-d_6, ppm) δ 140.02, 134.28, 134.18, 131.95, 130.91, 127.24, 127.12, 126.95, 123.63, 121.15, 110.39. ^{31}P NMR (162 MHz, DMSO-d_6, ppm) δ: 24.33. HR-MS (ESI) $[M+H]^+$ for ($C_{54}H_{36}N_3OP$) Calculated: 774.2596.

3. 5. 4. OLED Fabrication and Measurements

Indium tin oxide (ITO)-coated glass substrates were cleaned with detergent, deionized water, acetone, and isopropanol, and then subjected to UV−ozone treatment for 30 min, before loading into a vacuum evaporation system. The organic layers and a cathode aluminum layer were thermally evaporated through shadow masks under vacuum ($< 6 \times 10^{-5}$ Pa) with an evaporation rate of < 0.3 nm s^{-1}. The layer thickness and deposition rate were monitored in situ during deposition by an oscillating quartz thickness monitor. OLED properties were measured using a Keithley 2400 source meter and a Konica Minolita CS-2000 spectroradiometer.

3. 6. Conclusion

In summary, two ambipolar hosts, **CzPO** and **Cz3PO**, with high triplet energies were designed and synthesized for use in sky blue TADF-based OLED. Reduced efficiency rolloffs were demonstrated in sky blue TADF-based OLEDs using **CzPO** and **Cz3PO** as ambipolar hosts compared to the device with the reference **DPEPO** host. Sky blue TADF-OLEDs based employing **CzPO** and **Cz3PO** host materials showed maximum η_{ext} of 13.1% and 13.2%, respectively, and reduced rolloff with EQEs of 4.2% and 4.2%, respectively, at current densities of 100 mA cm^{-2}.

References

[1] a) T. T. Bui, F. Goubard, M. Ibrahim-Ouali, D. Gigmes, F. Dumur, *Appl. Sci.*, **2018**, 8, 494; b) X. Cai, S. J. Su, *Adv. Funct. Mater.*, **2018**, 28, 1802558; c) M. Kim, S. K. Jeon, S. H. Hwang, J. Y. Lee, *Adv. Mater.*, **2015**, 27, 2515–2520; d) R. J. Holmes, S. R. Forrest, Y. J. Tung, R. C. Kwong, J. J. Brown, S. Garon, M. E. Thompson, *Appl. Phys. Lett.*, **2003**, 82, 2422–2424; e) L. S. Cui, J. U. Kim, H. Nomura, H. Nakanotani, C. Adachi, *Angew. Chem. Int. Ed.*, **2016**, 55, 6864–6868.

[2] a) Y. Tao, C. Yang, J. Qin, *Chem. Soc. Rev.*, **2011**, 40, 2943–2970; b) K. Goushi, R. Kwong, J. J. Brown, H. Sasabe, C. Adachi, *J. Appl. Phys.*, **2004**, 95, 7798–7802.

[3] a) L. Xiao, Z. Chen, B. Qu, J. Luo, S. Kong, Q. Gong, J. Kido, *Adv. Mater.,* **2011**, 23, 926–952; b) V. Adamovich, J. Brooks, A. Tamayo, A.M. Alexander, P. I. Djurovich, B.W. D'Andrade, C. Adachi, S. R. Forrest, M. E. Thompson, *New J. Chem.*, **2002**, 26, 1171–1178; c) T. Chatterjee, K. T. Wong, *Adv. Opt. Mater.*, **2019**, 7, 1800565.

[4] a) S. Y. Lee, C. Adachi, T. Yasuda, *Adv. Mater.*, **2016**, 28, 4626–4631; b) I. S. Park, J. Lee, T. Yasuda, *J. Mater. Chem. C*, **2016**, 4, 7911–7916; c) C. Murawski, K. Leo, M. C. Gather, *Adv. Mater.*, **2013**, 25, 6801–6827.

[5] T. Nishimoto, T. Yasuda, S. Y. Lee, R. Kondo, C. Adachi, *Mater. Horizons*, **2014**, 1, 264–269.

[6] Y. Im, J. Y. Lee, *Chem. Commun.*, **2013**, 49, 5948–5950.

[7] Z. Q. Zhu, T. Fleetham, E. Turner, J. Li, *Adv. Mater.*, **2015**, 27, 2533–2537.

[8] Y. Tao, Q. Wans, C. Yang, C. Zhong, K. Zhang, J. Qin, D. Ma, *Adv. Funct. Mater.,* **2010**, 20, 304–311.

[9] K. S. Yook, Y. Lee, *Adv. Mater.*, **2012**, 24, 3169–3190.

[10] a) A. Chaskar, H. F. Chen, K. T. Wong, *Adv. Mater.*, **2011**, 23, 3876–3895; b) H. Lim, H. Shin, K.-H. Kim, S.-J. Yoo, J.-S. Huh, J.-J. Kim, *ACS Appl. Mater. Interfaces*, **2017**, 9,

37883–37887.

[11] M. K. Leung, Y. H. Hsieh, T. Y. Kuo, P. T. Chou, J. H. Lee, T. L. Chiu, H. J. Chen, *Org. Lett.*, **2013**, 15, 4694–4697.

[12] M. S. Lin, S. J. Yang, H. W. Chang, Y. H. Huang, Y. T. Tsai, C. C. Wu, S. H. Chou, E. Mondal, K. T. Wong, *J. Mater. Chem.*, **2012**, 22, 16114–16120.

[13] B. Pan, B. Wang, Y. Wang, P. Xu, L. Wang, J. Chen, D. Ma, *J. Mater. Chem. C*, **2014**, 2, 2466–2469.

[14] C. J. Zheng, J. Ye, M. F. Lo, M. K. Fung, X. M. Ou, X. H. Zhang, C. S. Lee, *Chem. Mater.*, **2012**, 24, 643–650.

[15] a) J. Zhang, D. Ding, Y. Wei, H. Xu, *Chem. Sci.*, **2016**, 7, 2870–2882; b) C. Han, Y. Zhao, H. Xu, J. Chen, Z. Deng, D. Ma, Q. Li, P. Yan, *Chem.-A Eur. J.*, **2011**, 17, 5800–5803.

[16] N. Lin, J. Qiao, L. Duan, L. Wang, Y. Qiu, *J. Phys. Chem. C*, **2014**, 118, 7569–7578.

[17] M. Kim, J. Y. Lee, *Adv. Funct. Mater.*, **2014**, 24, 4164–4169.

[18] S. Gong, Y. L. Chang, K. Wu, R. White, Z. H. Lu, D. Song, C. Yang, *Chem. Mater.,* **2014**, 26, 1463–1470.

[19] K. Masui, H. Nakanotani, C. Adachi, *Organic. Electronics*, **2013**, 14, 2721–2726.

[20] K. Shizu, M. Uejima, H. Nomura, T. Sato, K. Tanaka, H. Kaji, C. Adachi, *Phys. Rev. Applied.*, **2015**, 3, 014001.

[21] L. S. Cui, H. Nomura, Y. Geng, J. U. Kim, H. Nakanotani, C. Adachi, *Angew. Chem. Int. Ed.*, **2017**, 56, 1571–1575.

[22] G.-S. Kim, T. I. Lee, B. J. Cho, H.-Y. Yu, *Appl. Phys. Lett.*, **2019**, 114, 012102.

[23] I. S. Park, H. Seo, H. Tachibana, J. U. Kim, J. Zhang, S. M. Son, T. Yasuda, *ACS Appl. Mater. Interfaces*, **2017**, 9, 2693–2700.

Chapter 4

Nanosecond Time Scale Delayed Fluorescence Molecule for Deep-Blue Organic Light-Emitting Diodes with Small Efficiency Rolloff

4. 1. Introduction

Blue TADF-OLEDs suffer from severe efficiency rolloff compared to green and red counterparts, because relatively long-lived triplet excitons in blue TADF molecules directly effects on the operational stability and efficiency rolloff characteristics of TADF-OLEDs by increasing the exciton deactivation processes at high current density such as triplet–triplet annihilation (TTA) and singlet–triplet annihilation (STA).[24,25] New blue TADF molecules with ideally short exciton lifetimes (< 1 μs) thus are essentially required for future OLED lighting applications. To realize short exciton lifetimes in pure organic TADF molecules, a rate constant of RISC (k_{RISC}, $T_1 \rightarrow S_1$) is a most critical parameter because TADF molecules emit the light primarily via the $S_1 \rightarrow T_1 \rightarrow S_1 \rightarrow S_0$ and $T_1 \rightarrow S_1 \rightarrow S_0$ delayed processes with the $S_1 \rightarrow S_0$ prompt process under electro-excitation. According to first-order perturbation theory (i.e., Fermi's golden rule), k_{RISC} between the two states is proportional to $<\mathrm{S}|\hat{H}_{\mathrm{SOC}}|\mathrm{T}>/\Delta E_{\mathrm{ST}}$: [26–29]

$$k_{\mathrm{RISC}} \propto \left|\langle \mathrm{S}|\hat{H}_{\mathrm{SOC}}|\mathrm{T}\rangle\right|^2 \exp\left(\frac{-\Delta E_{\mathrm{ST}}}{k_{\mathrm{B}}T}\right)$$

where $<\mathrm{S}|\hat{H}_{\mathrm{SOC}}|\mathrm{T}>$ is the spin–orbit coupling (SOC) matrix element between the excited singlet (S) and triplet (T) states, k_{B} is the Boltzmann constant, and T is temperature. Based on this relationship, minimizing ΔE_{ST} is widely adopted as a strategy for efficient intramolecular charge-transfer (CT) TADF molecules.[1,3–22,24] However, the spin–flip processes (i.e. intersystem crossing: ISC and RISC) between excited CT singlet (^{1}CT) and triplet (^{3}CT) states are very inefficient in accordance with the El-Sayed rule because of the independent electric dipole moment with an electron spin, resulting from weak SOC matrix element.[30,31] In contrast, remarkably strong SOC could be expected when the spin-flip processes arise between the CT and an energetically close-lying locally excited (LE) states with different spin multiplicities due to an orbital angular momentum change between the two states.[19,29] In consideration of this aspect, several groups have reported that k_{RISC} is accelerated by the strong SOC matrix element between the ^{1}CT (S_1) and ^{3}LE (T_2) states, caused by non-adiabatic vibronic coupling ($\hat{H}_{\mathrm{VC}}$) between the ^{3}CT (T_1) and ^{3}LE (T_2) states.[32–34]

Recently, Kaji and co-workers reported a through-space CT molecule by introducing face-to-face alignment of the donor and acceptor units (**Figure 4-1a**).[35] Such a through-space CT character in single molecule induce extremely small spatial overlap between the highest occupied molecular orbital (HOMO) and lowest unoccupied molecular orbital (LUMO), resulting in a very small ΔE_{ST}. Although an exceedingly large k_{RISC} value of over 10^7 s^{-1} were achieved in its doped film, an unusually slow rate constant of fluorescence radiative decay ($k_\mathrm{r} = 1.1 \times 10^6$ s^{-1}) was observed. This is because negligible spatial overlap of the through-space molecule should lead to decreasing the transition dipole moment, which should affect its small radiative decay, according to Fermi's golden rule. As a result, the doped film exhibits a relatively long delayed emission lifetime (τ_d) of 4.1 μs. In 2018, Yasuda and co-workers have successfully designed a non-metallic TADF molecule with the largely enhanced SOC matrix element of $<^1\mathrm{CT}|\hat{H}_{\mathrm{SOC}}|^3\mathrm{LE}> = 4.67$ cm^{-1} (e.g. generally aromatic organic molecules have very small $<^1\mathrm{CT}|\hat{H}_{\mathrm{SOC}}|^3\mathrm{LE}> \leq 0.10$ cm^{-1}), thereby attaining a large k_{RISC} of 3.5×10^6 s^{-1} (Fig. 1b).[19] However, this molecule also has a very large rate constant of ISC ($k_{\mathrm{ISC}} = 9.9 \times 10^7$ s^{-1}), which is over 10 times larger than that of k_{RISC}, since SOC generally affects the whole spin–flip processes such as not only k_{RISC} but also k_{ISC}. Consequently, the ISC process occurs much more rapidly than the RISC process in this molecular system, which should interrupt conquest in regard with an ideal exciton lifetime. Therefore, the balance of rate constants k_r, k_{ISC}, and k_{RISC} is the decisive factor controlling the exciton lifetimes. In other words, a larger k_r than a k_{ISC} as well as minimizing difference between a k_{ISC} and k_{RISC} as small as possible with maintaining $^1\mathrm{CT} \approx {}^3\mathrm{CT} \approx {}^3\mathrm{LE}$ are concurrently required for TADF molecules possessing ideally fastest exciton lifetime.

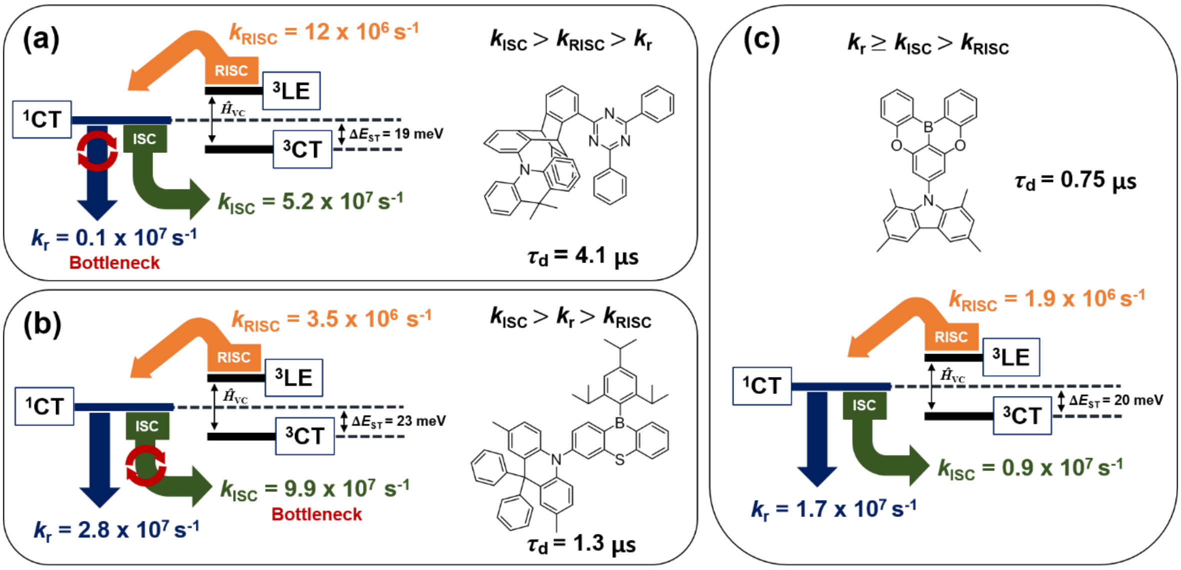

Figure 4-1. Schematic illustration of plausible TADF mechanism and the rate constants. k_r, k_{ISC}, and k_{RISC} represent the rate constants of fluorescence radiative decay, ISC, and reverse ISC, respectively.

Herein, I demonstrate a small modulation in the excited states of an aromatic organic molecules, mediated by spin–orbit coupling between ^{1}CT and ^{3}LE states, greatly affects the rate constants of a TADF molecule. As a result, an ideal nano-second scale exciton lifetime of 750 ns in a deep-blue TADF molecule was attained (**Figure 4-1c**). This can drastically minimize efficiency rolloff in the TADF-OLEDs.

4. 2. Molecular Design

To validate our concept in this study, a donor–acceptor (D–A) type TADF molecule, **TMCz-BO** (**Figure 4-2**), by introducing 1,3,6,8-tetramethyl-9*H*-carbazole (**TMCz**) as a donor unit and 5,9-dioxa-13*b*-boranaphtho[3,2,1-*de*]anthracene (**BO**) as an acceptor unit was designed, because both units have ideally high T_1 energies (**TMCz** and **BO**[36]: E_T = 3.00 eV, which are similar to the ^{1}CT of previously reported D–A type deep-blue TADF emitters,[6,8,9,13–16,20–22,24] expecting to attain ideal $^1\mathrm{CT} \approx {}^3\mathrm{LE}$. Moreover, the small spatial overlap of this molecule between the HOMO and LUMO in **TMCz** and **BO**, respectively, induced the CT character in both S_1 and T_1 states, resulting in small calculated ΔE_{ST} of 0.01 eV (i.e. $^1\mathrm{CT} \approx {}^3\mathrm{CT}$), which was carried out using time-dependent density functional theory (TDDFT) at the PBE0/6-31G(d) level in the gas phase. In order to control the ^{3}LE state of an acceptor unit, a model molecule, **TMCz-3P** (**Figure 4-2**), comprising a 3,11-diphenyl-5,9-dioxa-13*b*-boranaphtho[3,2,1-*de*]anthracene (**3P**) as an acceptor was also designed. This has a relatively lower E_T of 2.76 eV than that of **BO** (**Figure 4-3**), because theadditional phenyl substituents lead to the longer π-conjugation, thereby decreasing the E_T. Although this molecule has the similarly small frontier orbital overlap, relatively strong LE character was observed rather than CT one in its T_1 state from the triplet spin density distribution (TSDD) simulations using the optimized ground-state geometry (**Figure 4-2**). Meanwhile, the result of the TSDD simulations additionally revealed that **TMCz-BO** has the strong CT character rather than LE one in its T_1 state. This is because the TSDD of **TMCz-BO** resided on the entire D–A molecule, whereas **TMCz-3P** displayed the TSDD on only the its acceptor unit (**3P**, **Figure 4-2**).

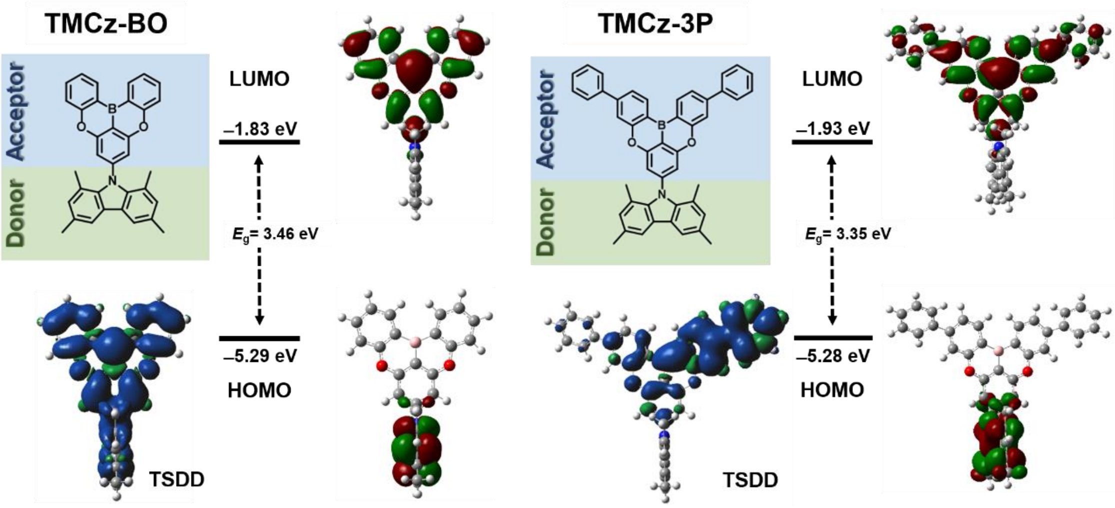

Figure 4-2 Molecular structures and HOMO and LUMO energy levels of **TMCz-BO** and **TMCz-3P** characterized by DFT calculations at the PBE0/6-31G(d) level of theory and TSDDs in the T_1 state.

Table 4-1. Summary of TDDFT calculations (PBE0/6-31G(d)).

Compound	HOMO [eV]	LUMO [eV]	E_g [eV]	E_S / E_T [eV]	ΔE_{ST} [eV]	f @S_0	μ [D]	λ_S [eV]
TMCz-BO	−5.29	−1.83	3.46	2.56 / 2.55	0.01	0.0057	3.39	0.15
TMCz-3P	−5.27	−1.96	3.54	2.63 / 2.62	0.01	0.0013	3.83	0.16

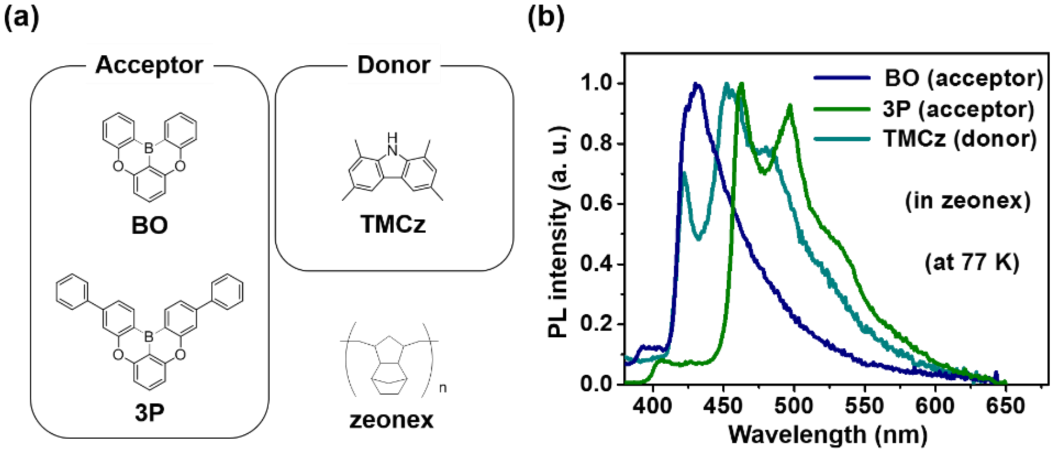

Figure 4-3. (a) Molecular structures of **BO**, **3P** (acceptor), and **TMCz** (donor) (b) Phosphorescence (77 K) spectra of **BO**, **3P** (acceptor), and **TMCz** (donor).

4. 3. Photophysical and TADF Properties

The fundamental photophysical properties of **TMCz-BO** and **TMCz-3P** were first studied in toluene solution at the concentration of 10^{-5} M. As shown in **Figure 4-4a**, both materials exhibited two clear absorption bands in the UV–Vis absorption spectra, in which a shorter wavelength is attributed to the π–π* transition of the acceptor and donor units, whereas another one at a longer wavelength (>370 nm) is corresponding to an intramolecular CT transition from the donor to acceptor units. For further investigation of the phothophysical and TADF properties, doped films of both emitters in an amorphous host matrix (i.e., PPF: 2,8-bis(diphenylphosphoryl)dibenzo[*b*,*d*]furan, E_T = 3.1 eV) were prepared in order to avoid concentration quenching. As can be seem from **Figure 4-4b**, 30 wt% doped films of **TMCz-BO** and **TMCz-3P** exhibited blue emissions with peaks at λ_{PL} = 467 and 477 nm, corresponding Commission Internationale de l'Éclairage (CIE) chromaticity coordinates of (0.15, 0.18) and (0.16, 0.25), respectively. From the transient PL characteristics of the doped films at 300 K, each of a clear nanosecond-scale prompt component and a microsecond-scale delayed PL component were observed. The decay were well fitted by using the biexponential model. As shown in **Figure 4-4c**, **TMCz-BO** has an extremely fast delayed emission lifetime (τ_d) of 750 ns (fractional delayed PL quantum yield: Φ_d = 32%) with a prompt emission lifetime (τ_p) of 38 ns (fractional prompt PL quantum yield: Φ_p = 66%) in N_2, whereas a relatively long τ_d of 14.5 μs (Φ_d = 11%) with similar τ_p of 29 ns (Φ_p = 65%) was observed in the **TMCz-3P**-based doped film (**Figure 4-4d**). The rate constants (i.e. k_r, k_{ISC}, and k_{RISC}) were also estimated for both doped films using the reported method.[19] Although similar k_r and k_{ISC} were determined from both doped films. (**TMCz-BO**: k_r = 1.7×10^7 s^{-1}; k_{ISC} = 0.9×10^7 s^{-1} and **TMCz-3P**: k_r = 2.3×10^7 s^{-1}; k_{ISC} = 1.2×10^7 s^{-1}) **TMCz-BO** has a large k_{RISC} of 1.9×10^6 s^{-1}, which is two order of magnitude higher than that of **TMCz-3P** (3.3×10^4 s^{-1}).

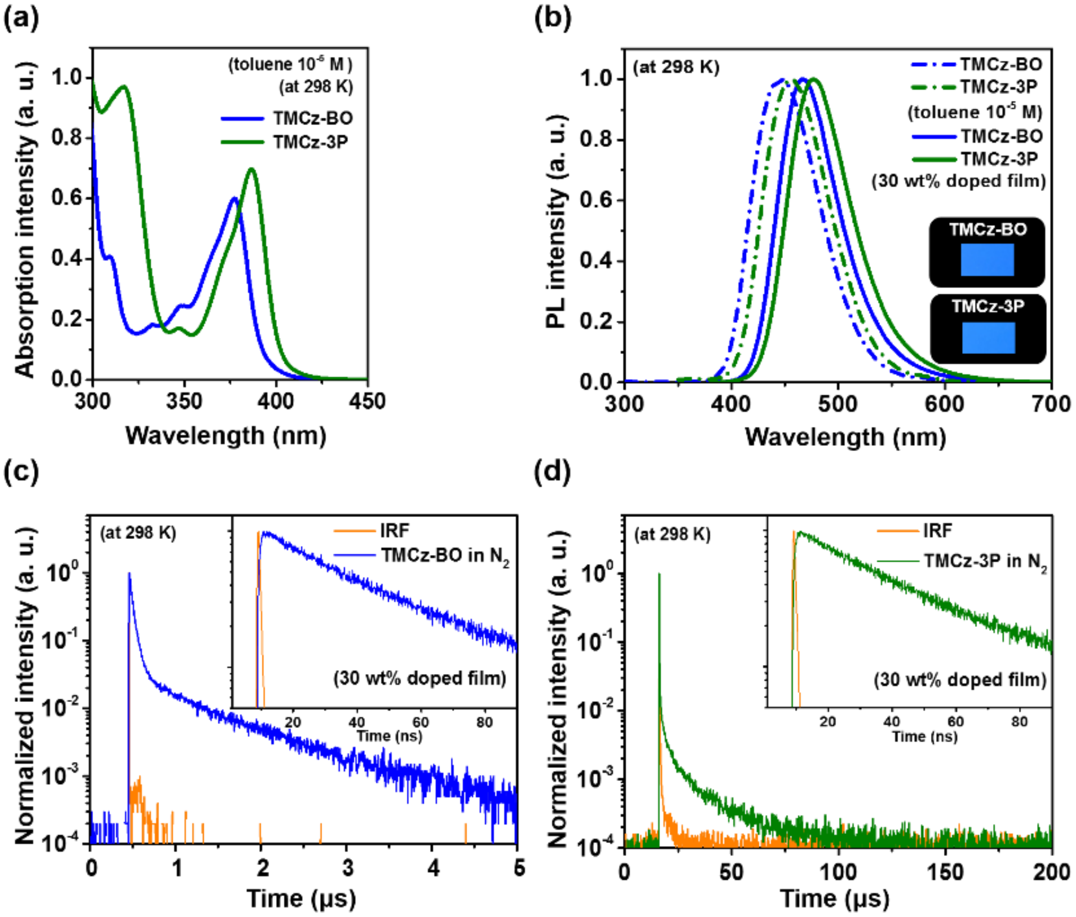

Figure 4-4. (a) UV–vis absorption spectra of **TMCz-BO** and **TMCz-3P** in 10^{-5} M toluene. (b) PL emission spectra of **TMCz-BO** and **TMCz-3P** in 10^{-5} M toluene and 30 wt% doped films in a PPF host matrix. Transient PL decay curves of (c) 30 wt% **TMCz-BO** (inset, τ_p [ns]) and (d) **TMCz-3P** (inset, τ_p [ns]) doped films in a PPF host matrix.

For a deeper understanding with regard to their excited state properties, the solvatochromic effects of **TMCz-BO** and **TMCz-3P** were also investigated in various solvents (**Figure 4-5**). Fluorescence spectra with large bathochromic shifts were observed when the solvent polarity was changed from non-polar cyclohexane to polar dichloromethane. The maximum peak wavelength (λ_{PL}) of **TMCz-BO** was about 407 nm in cyclohexane and 503 nm in dichloromethane, whereas the λ_{PL} of **TMCz-3P** was 416 nm in cyclohexane and 517 nm in dichloromethane. Owing to increased solvent polarity, there was a large difference in the emission peak wavelength ($\Delta\lambda_{max}$ = 96 nm for **TMCz-BO** and $\Delta\lambda_{max}$ = 101 nm for **TMCz-3P**), demonstrating pronounced positive solvatochromism, which confirmed the strong CT character of **TMCz-BO** and **TMCz-3P** in their S_1 states.

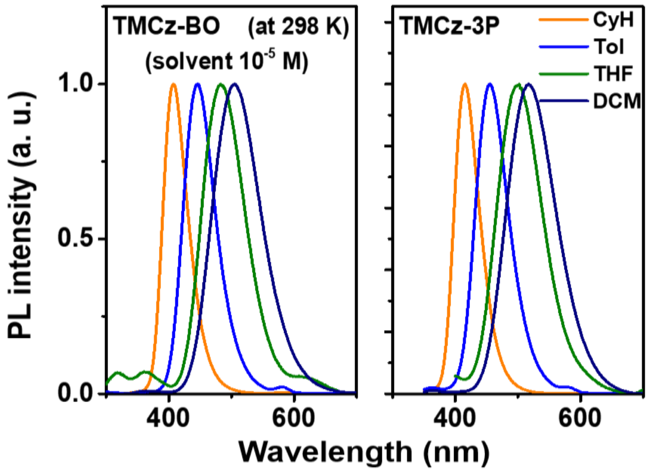

Figure 4-5. Detailed fluorescence spectra with bathochromic shifts of **TMCz-BO** and **TMCz-3P** in cyclohexane (CyH), toluene (Tol), tetrahydrofuran (THF), and dichloromethane (DCM) solutions.

To understand the exciton dynamics in the excited states of **TMCz-BO** and **TMCz-3P**, the phosphorescence (77 K) and fluorescence (298 K) spectra of 5–30 wt% doped films in the PPF host matrix were measured to identify whether their T_1 states have a CT or LE (**Figure 4-6a**). The phosphorescence spectra of 5–30 wt% **TMCz-BO** doped films contained a broad and structureless characteristics (i.e., CT character) without the vibrational mode similarly with the ^{3}LE of both the donor (**TMCz**) and acceptor (**3P**) units. Furthermore, an E_T (2.93 eV) of **TMCz-BO**, which was estimated from onset of the phosphoresce spectrum of the 30 wt% doped film, is quite far from those of both **TMCz** and **3P** (^{3}LE = 3.00 eV). Meanwhile, a similar E_T (2.76 eV) of **TMCz-3P** with that of the acceptor (**3P**, ^{3}LE = 2.76 eV) was observed (**Figure 4-6b**). The phosphorescence spectra of **TMCz-3P** coincided well with that of the acceptor (**3P**) unit with appreciable red-shift to the onset of the fluorescence. In addition, a LE character with vibrational mode was observed in the phosphorescence spectra of 5–20 wt% **TMCz-3P**-based doped films, even though the phosphorescence spectrum seems to be a CT character in the 30 wt% doped film.

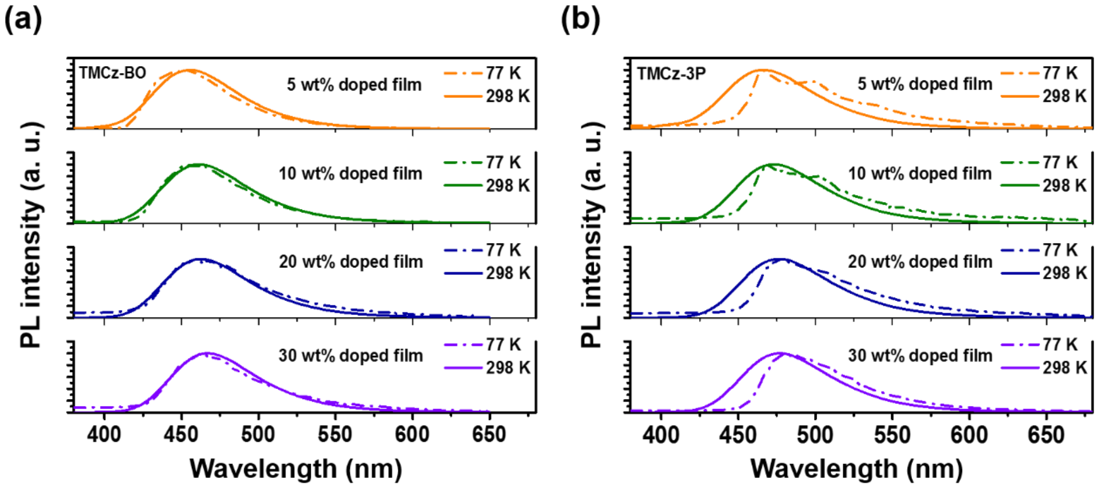

Figure 4-6. (a, b) Fluorescence (line, 298 K) and phosphorescence (dash dot, 77 K) spectra of doped films for (a) **TMCz-BO** and (b) **TMCz-3P**.

As a next step, the temperature dependences of k_{ISC} and k_{RISC} (**Figure 4-7**) using the 30 wt% doped films were also analyzed. According to the classical Arrhenius equation, k_{RISC} is given as $k_{\mathrm{RISC}} = A\exp(-E_a/k_BT)$, where A is the frequency factor involving the SOC constant. From the Arrhenius plots of k_{RISC}, similarly small activation energy for RISC ($E_{\mathrm{a,\,RISC}}$) values were experimentally estimated to be 13.4 meV for **TMCz-BO** and 39.8 meV for **TMCz-3P**. Moreover, small $E_{\mathrm{a,\,RISC}}$ values for 5–20 wt% doped films were also analyzed in the range of 13.7−14.5 meV for **TMCz-BO** and 24.0−34.0 meV for **TMCz-3P** (**Table 4-2**). Further, I estimated the activation energy for ISC ($E_{\mathrm{a,\,ISC}}$) and obtained $E_{\mathrm{a,\,ISC}}$=3 meV for **TMCz-BO** and $E_{\mathrm{a,\,ISC}}$~0 meV for **TMCz-3P**, respectively. Based on the phosphorescence characteristics in **Figure 4-6a, b**, the ISCs occur through ^{1}CT→^{3}CT→^{3}LE in **TMCz-3P** and ^{1}CT→^{3}LE→^{3}CT in **TMCz-BO**, respectively, resulted in both ISC rates of rather fast decay rates of ~10^7. In case of **TMCz-3P**, hyperfine coupling would be one of a possible spin flipping mechanism between ^{1}CT and ^{3}CT levels.

Table 4-2. Photophysical data of **TMCz-BO** and **TMCz-3P**.

TADF emitter	x wt% **TMCz-BO** doped film in PPF				x wt% **TMCz-3P** doped film in PPF			
	5 wt%	10 wt%	20 wt%	30 wt%	5 wt%	10 wt%	20 wt%	30 wt%
$E_{\mathrm{a,RISC}}$[a)] [meV]	14.5	14.2	13.7	13.4	34.0	30.4	24.0	39.8
y-intercept [s^{-1}]	2.1×10^{-6}	3.0×10^{-6}	3.1×10^{-6}	3.3×10^{-6}	3.6×10^{-4}	3.6×10^{-4}	5.4×10^{-4}	15×10^{-4}

[a] Activation energies of the rate constants of RISC (k_{RISC}) obtained with the x wt% doped films of **TMCz-BO** and **TMCz-3P**.

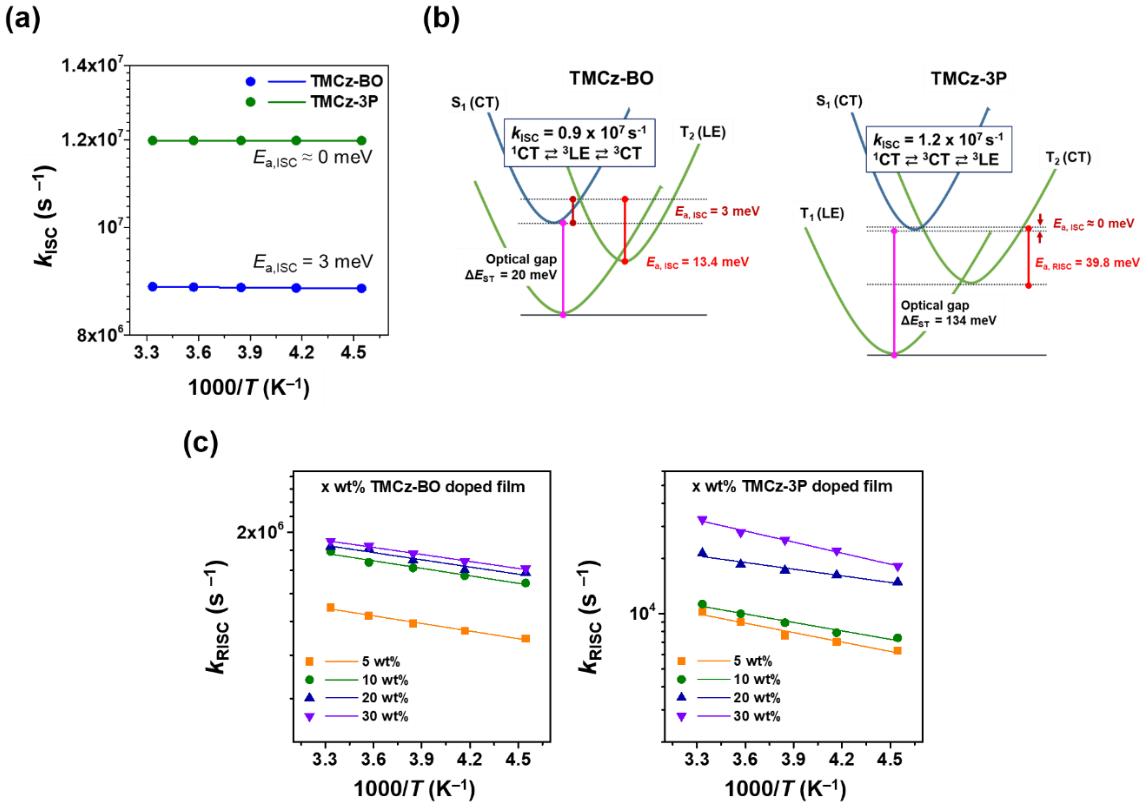

Figure 4-7. (a) Arrhenius plots of the rate constants of ISC (k_{ISC}) obtained with 30 wt% doped films of **TMCz-BO** and **TMCz-3P**. (b) Schematic illustration of plausible ISC mechanisms for **TMCz-BO** and **TMCz-3P**. (c) Arrhenius plots of the rate constants of RISC (k_{RISC}) obtained with x wt% doped films of **TMCz-BO** and **TMCz-3P**, where the solid lines denote the least-squares fittings.

In order to investigate more insight into the spin-flip RISC process, the relationship between the SOC and E_a value with consideration for their ΔE_{ST} values was carefully analyzed. While **TMCz-BO** has a similarly small ΔE_{ST} of 20 meV with its E_a, a quite large ΔE_{ST} of **TMCz-3P** was estimated to be 134 meV, which is three times larger than its ΔE_a. Such the experimentally obtained k_{RISC}, E_a, and ΔE_{ST} suggest that different spin-flip processes should be involved in **TMCz-BO** and **TMCz-3P**. As can be seem from the energy level diagram in **Figure 4-8a**, the efficient RISC spin-flip process for **TMCz-BO** should be involved in ^{3}CT → ^{3}LE → ^{1}CT because energetically close-lying excited states induce efficient $\hat{H}_{\mathrm{VC}}$ from the ^{3}CT to ^{3}LE states, and then RISC could be accelerated from ^{3}LE to ^{1}CT states mediated by much larger SOC matrix element ($<^1\mathrm{CT}|\hat{H}_{\mathrm{SOC}}|^3\mathrm{LE}> = 0.124\ \mathrm{cm}^{-1}$) than $<^1\mathrm{CT}|\hat{H}_{\mathrm{SOC}}|^3\mathrm{CT}> = 0.001\ \mathrm{cm}^{-1}$, resulting in its extraordinarily fast emission lifetime of 750 ns. Meanwhile, it is difficult to occur the spin-flip process in the **TMCz-3P** molecule as the same pathway with **TMCz-BO**, even having a similarly large $<^1\mathrm{CT}|\hat{H}_{\mathrm{SOC}}|^3\mathrm{LE}> = 0.128\ \mathrm{cm}^{-1}$, since the its experimental ΔE_{ST} much larger than the thermal energy ($k_{\mathrm{B}}T \approx 25.9$ meV) at 300 K as well as its E_{a} (**Figure 4-8b**). Experimental data thus suggest that the $^3\mathrm{CT} \rightarrow {}^1\mathrm{CT}$ spin-flip process (i.e., hyperfine coupling)[38,39] should be occurred after efficient $\hat{H}_{\mathrm{VC}}$ from $^3\mathrm{LE}$ to energetically close-lying higher $^3\mathrm{CT}$ states, leading to relatively small k_{RISC} due to negligible $<^1\mathrm{CT}|\hat{H}_{\mathrm{SOC}}|^3\mathrm{CT}>$ of $0.001\ \mathrm{cm}^{-1}$. Therefore, energetically close-lying excited states (i.e., $^1\mathrm{CT} \approx {}^3\mathrm{CT} \approx {}^3\mathrm{LE}$) with suitably large SOC between the $^1\mathrm{CT}$ and $^3\mathrm{LE}$ should be realized to extremely fast emission lifetime in TADF molecules.

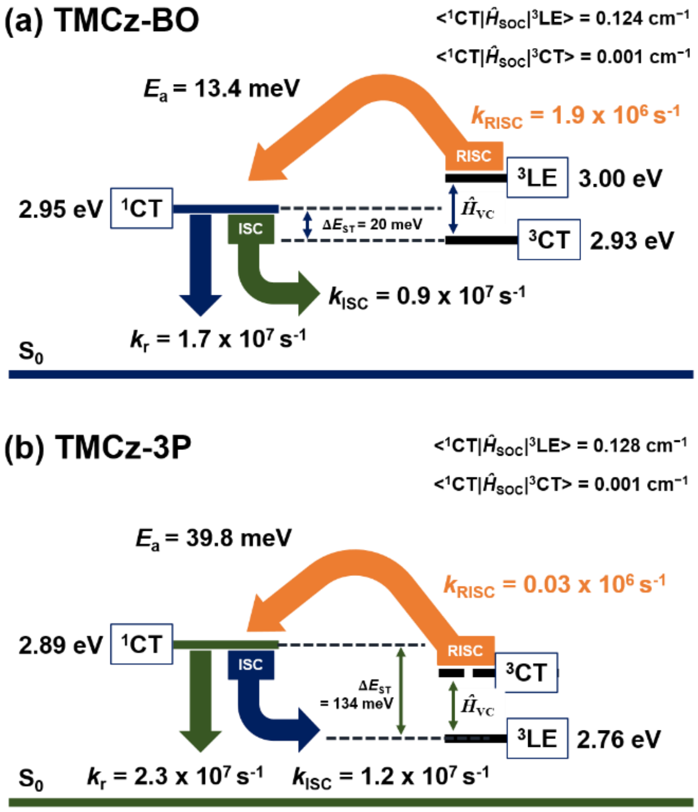

Figure 4-8. Schematic illustration of plausible TADF mechanisms for (a) **TMCz-BO** and (b) **TMCz-3P**. The energy levels and rate constants were estimated using 30 wt% doped films.

Table 4-3. Photophysical characteristics of **TMCz-BO** and **TMCz-3P**.

Compound	λ_{abs} [nm] sol$^{a)}$	λ_{PL} [nm] sol$^{a)}$ / film$^{b)}$	Φ_{PL}[%]$^{c)}$ sol$^{a)}$ / film$^{b)}$	τ_p [ns]$^{d)}$ / τ_d [μs]$^{d)}$	HOMO [eV]$^{e)}$	LUMO [eV]$^{f)}$	E_S / E_T [eV]$^{g)}$	ΔE_{ST} [meV]$^{h)}$	E_a [meV]$^{i)}$
TMCz-BO	282,377	446 / 467	81 / 98	38 / 0.75	−5.75	−2.56	2.95 / 2.93	20.0	13.4
TMCz-3P	298,386	455 / 477	56 / 76	29 / 14.5	−5.75	−2.64	2.88 / 2.74	134	39.8

$^{a)}$Measured in oxygen-free toluene at room temperature (298 K); $^{b)}$30 wt% doped thin film in a host matrix (host = PPF); $^{c)}$Absolute PLQY evaluated using an integrating sphere under a nitrogen atmosphere; $^{d)}$PL lifetimes of prompt (τ_p) and delayed (τ_d) decay components for 30 wt% doped film at 298 K; $^{e)}$Determined by photoelectron yield spectroscopy in pure neat films; $^{f)}$Deduced from the HOMO and optical energy gap (E_g); $^{g)}$Singlet (E_S) and triplet (E_T) energies estimated from onsets of the emission spectra at 298 K and 77 K in 30 wt% doped films, respectively; $^{h)}$$\Delta E_{ST} = E_S - E_T$; $^{h)}$Activation energies of RISC in 30 wt% doped films.

Table 4-4. Rate constants and quantum efficiencies of the doped films of 30 wt% **TMCz-BO** and **TMCz-3P**.$^{a)}$

Emitter	k_r^S [s^{-1}]	k_{ISC} [s^{-1}]	k_{RISC} [s^{-1}]	Φ_p [%]	Φ_d [%]	Φ_{ISC} [%]	Φ_{RISC} [%]
TMCz-BO	1.7×10^7	0.9×10^7	1.9×10^6	66	32	34	96
TMCz-3P	2.3×10^7	1.2×10^7	3.3×10^4	65	11	35	41

$^{a)}$Abbreviations: k_r^S, radiative rate constant ($S_1 \rightarrow S_0$); k_{ISC}, intersystem-crossing (ISC) rate constant ($S_1 \rightarrow T_1$); k_{RISC}, reverse ISC rate constant ($T_1 \rightarrow S_1$); Φ_p, quantum efficiency for prompt fluorescence component; Φ_d, quantum efficiency for delayed fluorescence component; Φ_{ISC}, ISC quantum efficiency; Φ_{RISC}, RISC quantum efficiency.

4. 4. Electroluminescence Performance

Employing **TMCz-BO** and **TMCz-3P** as emitters, two multi-layered OLEDs were fabricated using the following device architecture: indium tin oxide (ITO, 50 nm)/HAT-CN (10 nm)/TAPC (50 nm)/CCP (10 nm)/EML (20 nm)/PPF (10 nm)/B3PyPB (30 nm)/Liq (1 nm)/Al (100 nm), in which 2,3,6,7,10,11-hexacyano-1,4,5,8,9,12-hexaazatriphenylene (HAT-CN) and 8-hydroxyquinoline lithium (Liq) were used as hole injection and electron injection layers, respectively. The materials 4,4’-cyclohexylidenebis[*N,N*-bis(4-methylphenyl)benzenamine] (TAPC) and 1,3-bis[3,5-di(pyridine-3-yl)phenyl] benzene (B3PyPB) were used as hole transport and electron transport layers, respectively. Thin layers of 9-phenyl-3,9′-bicarbazole (CCP) and PPF with a high T_1 energy (3.0 and 3.1 eV) were inserted to suppress triplet exciton quenching at the neighbouring interfaces and to confine the excitons inside the emitting layers.[6,8,9,13–16,20–22,24,40] The EL characteristics of both devices are depicted in **Figure 4-9**, and the key device parameters are summarized in **Table 4-5**.

Table 4-5. EL performance of blue TADF-OLEDs.[a)]

TADF emitter	λ_{EL} [nm]	λ_{FWHM} [nm]	E_{FWHM} [eV]	V_{on} [V]	L_{max} [cd m^{-2}]	η_{ext} [%] Max / @100 cd m^{-2} / @1000 cd m^{-2}	η_c [cd A^{-1}]	η_p [lm W^{-1}]	CIE (*x*, *y*)
TMCz-BO	471	59	0.327	3.0	5900	20.7 / 20.2 / 17.4	29.8	31.2	(0.14, 0.18)
TMCz-3P	479	61	0.324	2.8	6500	20.4 / 18.3 / 12.8	37.8	40.3	(0.14, 0.26)

[a)] Abbreviations: λ_{EL} = EL emission maximum; λ_{FWHM} and E_{FWHM} = full width at half maximum; V_{on} = turn-on voltage at 1 cd m^{-2}; L_{max} = maximum luminance; η_{ext} = external EL quantum efficiency; η_c = maximum current efficiency; η_p = maximum power efficiency; CIE (*x*, *y*) = Commission Internationale de l'Éclairage colour chromaticity coordinates measured at 10 mA cm^{-2}.

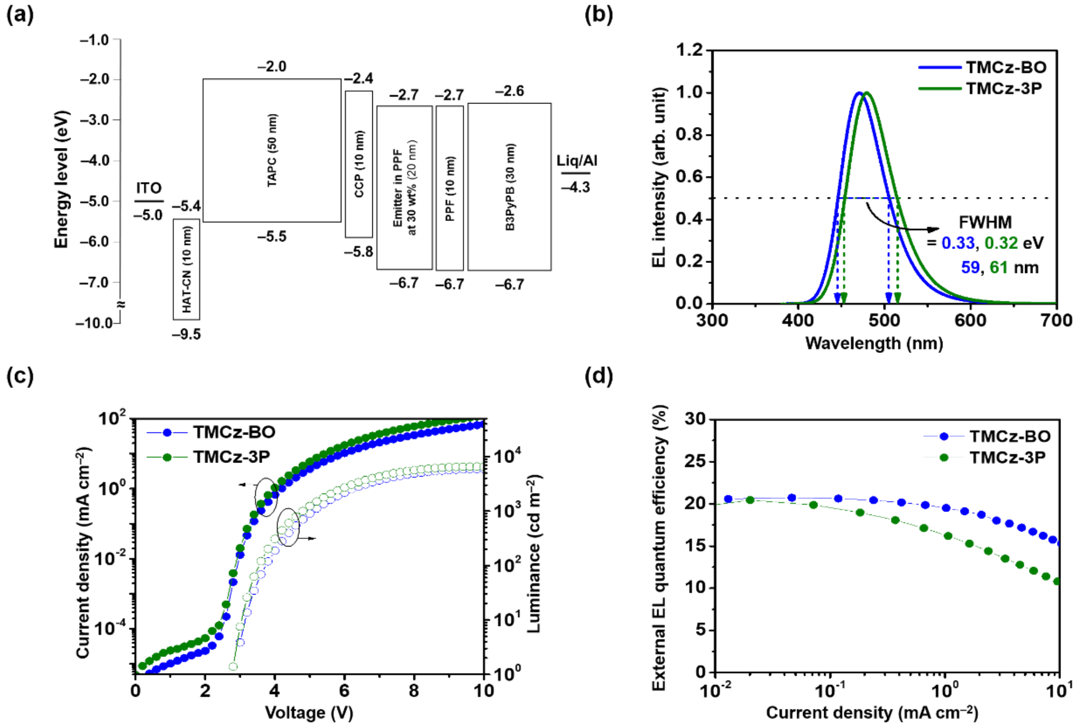

Figure 4-9. (a) Energy-level diagram of **TMCz-BO-** and **TMCz-3P**-based TADF-OLEDs. (b) Normalized EL spectra, (c) current density–voltage–luminance (*J*–*V*–*L*) characteristics, and (d) external EL quantum efficiency (η_{ext}) *versus* luminance plots of **TMCz-BO-** and **TMCz-3P-** based OLEDs.

As shown in **Figure 4-9a**, the devices based on **TMCz-BO** and **TMCz-3P** exhibited blue EL emission with peaks (λ_{EL}) at 471 nm (deep blue) and 479 nm (blue) with corresponding CIE chromaticity coordinates of (0.14, 0.18) and (0.14, 0.26), respectively, which were consistent with their corresponding PL spectra. It is noteworthy that the devices displayed a rather narrow full width at half-maximum (FWHM, λ_{FWHM}) of 59 nm (E_{FWHM} = 0.327 eV) for **TMCz-BO** and 61 nm (E_{FWHM} = 0.324 eV) for **TMCz-3P**, resulting from minimizing molecular vibrations using the rigid acceptor structure and minimizing molecular conformation changes in their ground and S_1 states using the *peri*-position dimethyl groups in TMCz.[19,23,40]

Figure 4-9c,d shows the current density–voltage–luminance (*J*–*V*–*L*) and external EL quantum efficiency versus current density (η_{ext}–J) plots. Both devices exhibited rather low turn-on voltages (V_{on}) in the range of 2.8–3.0 V and achieved high maximum η_{ext} exceeding 20% (20.7% for **TMCz-BO** and 20.4% for **TMCz-3P**). This high efficiency of the **TMCz-3P**-based device drastically decreased with increasing current density and luminance, which is similar to the trend observed for most reported blue TADF-OLEDs. As a result, low η_{ext} values (18.3% at 100 cd m^{-2} and 12.8% at 1000 cd m^{-2}) were obtained from the **TMCz-3P**-based device. However, the **TMCz-BO**-based device retained high η_{ext} values of 20.2% at 100 cd m^{-2} and 17.4% at 1000 cd m^{-2}, corresponding to a 2.4% and 15.9% decrease in η_{ext}, respectively. I aim to reduce TTA by increasing the speed of exciton lifetime in excited triplet state. Therefore, TTA simulations were studied with the η_{ext}–J curves for the devices based on **TMCz-3P** and **TMCz-BO** as shown in **Figure 4-10**. The equation for the TTA fitting is expressed as follows:[42]

$$\eta_{\mathrm{TTA}} = \frac{J_0}{4J}\left[\sqrt{1 + 8\frac{J}{J_0}} - 1\right]\eta_0$$

where η_{TTA} represents the η_{ext} of the device, η_0 refers to the initial η_{ext} in the absence of TTA, J stands for the current density of the device, and J_0 is the "onset" current density at $\eta = \eta_0/2$.

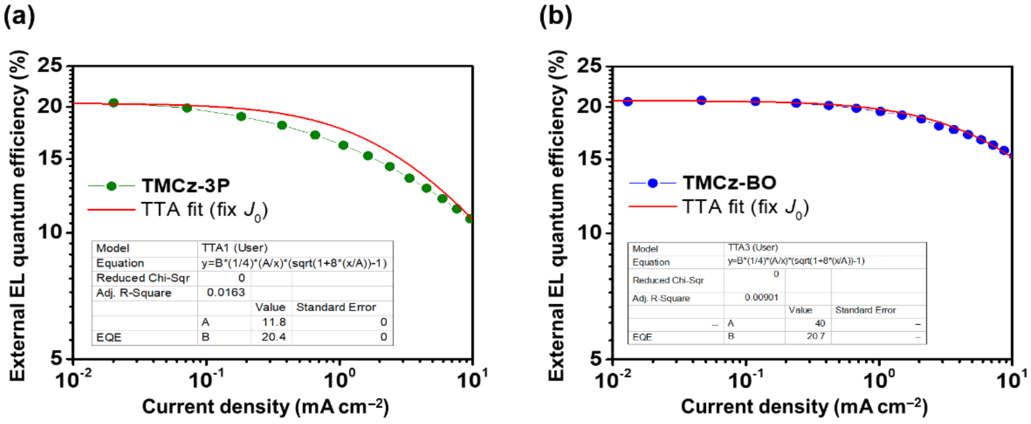

Model	TTA1 (User)		
Equation	y=B*(1/4)*(A/x)*(sqrt(1+8*(x/A))-1)		
Reduced Chi-Sqr	0		
Adj. R-Square	0.0163		
		Value	Standard Error
	A	11.8	0
EQE	B	20.4	0

Model	TTA3 (User)		
Equation	y=B*(1/4)*(A/x)*(sqrt(1+8*(x/A))-1)		
Reduced Chi-Sqr	0		
Adj. R-Square	0.00901		
		Value	Standard Error
--	A	40	–
EQE	B	20.7	–

Figure 4-10. External EL quantum efficiencies (η_{ext}) for devices based on **TMCz-3P** (a) and **TMCz-BO** (b) as a function of current density and the fitting results according to the triplet–triplet annihilation (TTA, red lines) mechanism.

TTA simulations relatively not matched well with the η_{ext}–J curves for device based on **TMCz-3P** (**Figure 4-10 (a)**). Rather rapid efficiency rolloff originates from the long triplet decay lifetime of τ_d =14.5 μs. Whereas, the appreciably relaxed efficiency rolloff of the device based on **TMCz-BO** (**Figure 4-10 (b)**) was observed and this can be ascribed to the short triplet exciton lifetime of τ_d = 750 ns. Low-efficiency rolloff is primarily attributed to its nano-second-order emission lifetime, which efficiently suppresses the accumulation of triplet excitons within **TMCz-BO**; hence, TTA could be minimized in the device. To the best of our knowledge, the efficiency decrease ratio of the **TMCz-BO**-based device is the smallest of those reported for TADF molecules for deep-blue OLEDs (CIE$y \leq 0.20$) to date (**Table 4-5**). [6,8,9,13–16,20–22,24,40]

4. 5. Experimental Section

4. 5. 1. Materials

All commercially available reagents and solvents were used as received unless otherwise noted. 2,8-Bis(diphenylphosphoryl)dibenzofuran (PPF) was prepared according to the literature procedures and were purified by vacuum sublimation. 2,3,6,7,10,11-Hexacyano-1,4,5,8,9,12-hexaazatriphenylene (HAT-CN) and 9-phenyl-3,9'-bicarbazole (CCP) were purified by vacuum sublimation before use. Other OLED materials were purchased from Luminescence Technology Corp. and were used for the device fabrication without further purification. The synthetic routes for deep-blue TADF molecules **1–4** are outlined in **Scheme 4-1**, and detailed synthetic procedures and characterization data for other intermediates (**1–4**) are given in **Schemes 4-2–3**. ^{1}H and ^{13}C NMR spectra were recorded on a Bruker Avance III 500 spectrometer. Chemical shifts of ^{1}H and ^{13}C NMR signals were quoted to tetramethylsilane (δ = 0.00), $CDCl_3$ (δ = 77.0), and DMSO-d_6 (δ = 39.5) as internal standards. Matrix-assisted laser desorption ionization time-of-flight (MALDI-TOF) mass spectra were collected on an Autoflex III spectrometer (Bruker Daltonics) using dithranol as the matrix. Elemental analysis was performed using an MT-5 CHN corder (Yanaco). Single-crystal X-ray analysis was carried out using a Rigaku VariMax with Saturn 70 system with graphite monochromated Mo$K\alpha$ radiation.All final products were purified by temperature-gradient vacuum sublimation with a P-100 system (ALS Technology), before the measurements and device fabrication.

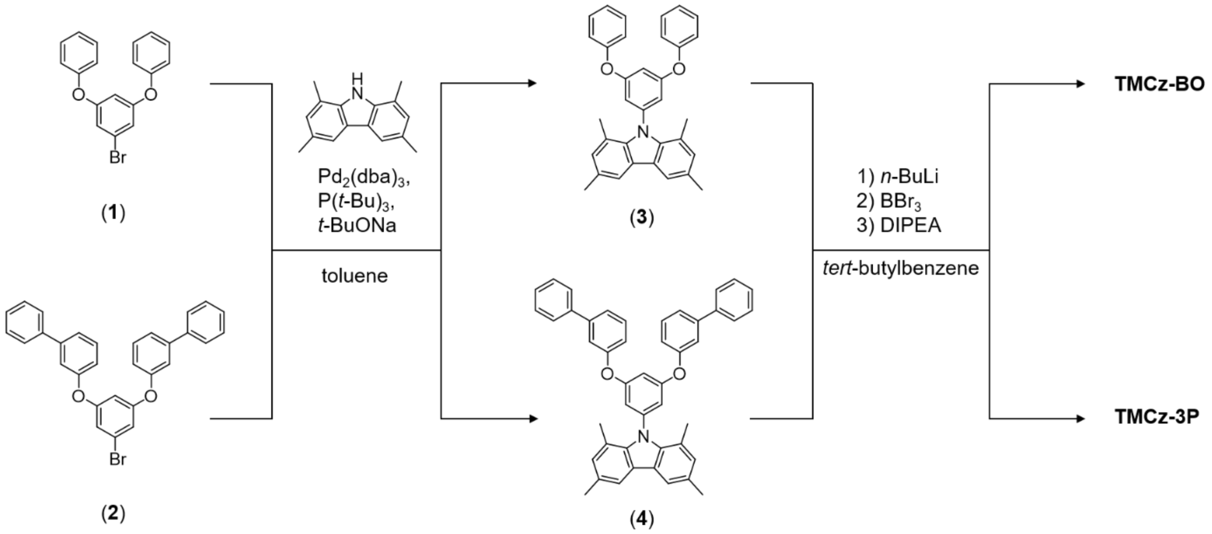

Scheme 4-1. Synthetic routes for **TMCz-BO** and **TMCz-3P**.

4. 5. 2. Synthesis

All reagents and anhydrous solvents were purchased from commercial sources and were used without further purification. The detailed synthetic procedures and characterization data for the intermediates are given in the Supplementary Information. The two final products investigated in this paper were synthesized by following the procedures described below, and then purified using temperature gradient vacuum sublimation with a P-100 system (ALS Technology). ^{1}H and ^{13}C NMR spectra were recorded on a Bruker Avance III 500 spectrometer. Chemical shifts of ^{1}H and ^{13}C NMR signals were quoted to tetramethylsilane (δ = 0.00), $CDCl_3$ (δ = 77.0), as internal standards. Mass spectra were measured in positive-ion atmospheric-pressure chemical ionization (APCI) mode on a Waters 3100 mass detector. Elemental analyses were carried out using a Yanaco MT-5 analyzer. For thin films and OLED fabrication, PPF[37] was synthesized according to the reported procedures, and then purified using temperature gradient vacuum sublimation. Other OLED materials were purchased from Luminescence Technology Corporation.

Synthesis of 5-bromo-1,3-diphenoxybenzene (1): NMP (150 mL) was added to a mixture of 1-bromo-3,5-difluorobenzene (20.0 g, 0.10 mol), phenol (24.5 g, 0.26 mol), and K_2CO_3 (35.9 g, 0.26 mol) at room temperature under a nitrogen atmosphere. The reaction mixture was stirred at 170 ºC for 12 h, and then cooled to room temperature. After addition of toluene and water for extraction, the organic layer was washed with brine, dried over anhydrous $MgSO_4$, and then condensed in vacuo. The crude product was purified by silica gel column chromatography (eluent; hexane/dichloromethane = 5/1) to afford compound **1** (28.3 g, 80% yield) as a colorless liquid. ^{1}H NMR (500 MHz, $CDCl_3$, δ): 7.29 (td, J = 7.1, 1.7 Hz, 4H), 7.08 (tt, J = 7.4, 2.1 Hz, 2H), 6.96 (dd, J = 8.7, 2.1 Hz, 4H), 6.74 (d, J = 2.2 Hz, 2H), 6.52 (t, J = 2.2 Hz, 1H); MS (ASAP) m/z: $[M^{+1}]^+$ calcd 341.20; found, 342.00.

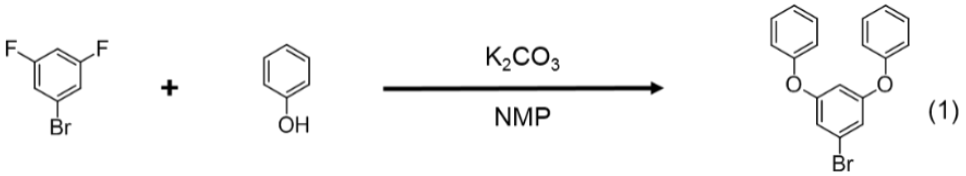

Scheme 4-2. Synthesis of compound **1**

Synthesis of 3,3''-((5-bromo-1,3-phenylene)bis(oxy))di-1,1'-biphenyl (2): Compound **2** was synthesized according to the same procedure described above for the synthesis of compound **1**. 3-phenylphenol (44.0 g, 0.26 mol) was used instead of phenol, giving compound **2** (40.9 g, 80% yield) as a colorless liquid. ^{1}H NMR (500 MHz, $CDCl_3$, δ): 7.49 (dd, J = 8.45, 1.2 Hz, 4H), 7.36 (t, J = 7.5 Hz, 6H), 7.33-7.27 (m, 4H), 7.20 (t, J = 2.0 Hz, 2H), 6.94 (m, 2H), 6.81 (d, J = 2.2 Hz, 2H), 6.60 (t, J = 2.2 Hz, 1H); MS (ASAP) m/z: $[M^{+1}]^+$ calcd 493.39; found, 495.05.

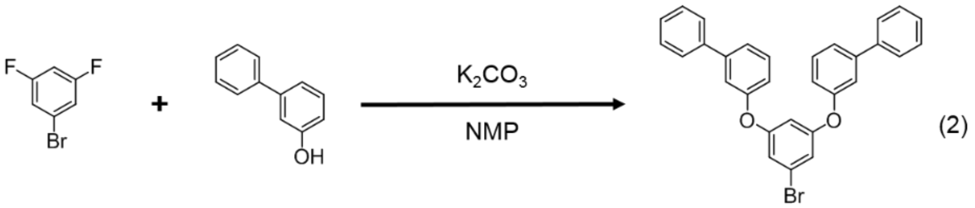

Scheme 4-3. Synthesis of compound **2**

Synthesis of 9-(3,5-diphenoxyphenyl)-1,3,6,8-tetramethyl-9*H*-carbazole (3): To a solution of **1** (20.0 g, 58.6 mmol) in toluene (100 mL) was added 1,3,6,8-tetramethyl-9*H*-carbazole (14.4 g, 64.5 mmol), $Pd_2(dba)_3$ (2.68 g, 2.93 mmol), $P(t\text{-}Bu)_3$ (1.19 g, 5.86 mmol), and *t*-BuONa (12.4 g, 128.9 mmol). After stirring at 110 ºC for 6 h, water was added to the reaction mixture at room temperature. The combined organic layer was extracted with toluene, and then dried over anhydrous $MgSO_4$. After filtration and evaporation, the crude product was purified by column chromatography on silica gel (eluent; hexane/dichloromethane = 5/1) to afford compound **3** (22.7 g, 80% yield) as a white solid. ^1H NMR (500 MHz, $CDCl_3$, δ): 7.70 (d, J = 8.1 Hz, 2H), 7.35 (td, J = 7.0, 1.7 Hz, 4H), 7.13 (tt, J = 7.4, 2.1 Hz, 2H), 7.07(dt, J = 7.8, 1.5 Hz, 4H), 6.94 (s, 2H), 6.90 (t, J = 4.5 Hz, 1H), 6.81 (d, J = 2.3 Hz, 2H) 2.47 (s, 6H), 2.08 (s, 6H); MS (ASAP) m/z: $[M^{+1}]^+$ calcd 483.60; found, 485.17.

Synthesis of 9-(3,5-bis([1,1'-biphenyl]-3-yloxy)phenyl)-1,3,6,8-tetramethyl-9*H*-carbazole (4): Compound **4** was synthesized according to the same procedure described above for the synthesis of **TMCz-BO**, except that **2** (20.0 g, 40.5 mmol), 1,3,6,8-tetramethyl-9*H*-carbazole (9.96 g, 44.5 mmol), $Pd_2(dba)_3$ (1.86 g, 2.03 mmol), $P(t\text{-}Bu)_3$ (0.82 g, 4.05 mmol), and *t*-BuONa (8.57 g, 89.2 mmol) were used as the reactants, giving compound **4** (20.5 g, 80% yield) as a light-yellow solid. ^1H NMR (500 MHz, $CDCl_3$, δ): 7.70 (s, 2H), 7.53 (dd, J = 8.5, 1.2 Hz, 4H), 7.46-7.41 (m, 5H), 7.39-7.34 (m, 5H), 7.29 (t, J = 4.0 Hz, 2H), 7.06-7.03 (m, 2H), 6.98 (t, J = 4.5 Hz, 1H), 6.93(s, 2H), 6.91(d, J = 2.3 Hz, 2H), 2.47(s, 6H), 2.10(s, 6H); MS (ASAP) m/z: $[M]^+$ calcd 635.79; found, 635.27.

Synthesis of TMCz-BO: A solution of *n*-butyllithium (*n*-BuLi) in hexane (3.11 mL, 2.5 M, 7.77 mmol) was added slowly to a solution of **2** (3.0 g, 6.47mmol) in *tert*-butylbenzene (30 mL) at –20 ºC under a nitrogen atmosphere. After stirring at 50 ºC for 4 h, hexane was distilled off at 100 ºC under a continuous flow of nitrogen. Boron tribromide (BBr_3) in dichloromethane (9.71 mL, 1.0 M, 9.71 mmol) was added slowly at –20 ºC. The reaction mixture was then allowed to warm to room temperature for 1 h and then stirred at 40 ºC for 1 h. After 10% of the solvent had been removed in vacuo, *N*,*N*-diisopropylethylamine (DIPEA, 1.67 g, 12.9 mmol) was added at 0 ºC. After stirring at 120 ºC for 5 h, methanol was added to the reaction mixture at room temperature. The reaction mixture was then filtered with a pad of Florisil. The crude product was washed with methanol to afford **TMCz-BO** (0.48 g, 15% yield) as a light-yellow solid. ^1H NMR (500 MHz, $CDCl_3$, δ): 8.77 (dd, J = 7.8, 1.5 Hz, 2H), 7.77 (td, J = 8.1, 1.5 Hz, 4H), 7.58 (dd, J = 7.8, 0.6 Hz, 2H), 7.46 (td, J = 7.4 Hz, 0.9 Hz, 2H), 7.40 (s, 2H), 6.95 (s, 2H), 2.51 (s, 6H), 1.97 (s, 6H); ^{13}C NMR (125 MHz, $CDCl_3$, δ): 160.65, 156.88, 148.61, 139.60, 134.66, 133.99, 130.29, 129.30 124.42, 123.22, 121.44, 118.63, 117.79, 112.01, 21.11, 19.33. MS (ASAP) *m/z*: $[M^{-1}]^+$ calcd 493.39; found, 492.17. Anal. calcd (%) for $C_{34}H_{26}BNO_2$: C 83.10, H 5.33, N 2.85; found: C 83.09, H 5.36, N 2.85.

Synthesis of TMCz-3P: TMCz-3P was synthesized according to the same procedure described above for the synthesis of **TMCz-BO**, except that **4** (3.0 g, 4.72 mmol), *n*-BuLi (2.26 mL, 5.66 mmol), BBr_3 (7.08 mL, 7.08 mmol), and DIPEA (1.22 g, 9.44 mmol) were used as the reactants, giving **TMCz-3P** (0.46 g, 15% yield) as a light-yellow solid. ^{1}H NMR (500 MHz, $CDCl_3$, δ): 8.74 (d, J = 8.1 Hz, 2H), 7.70 (td, J = 7.6, 1.4 Hz, 8H), 7.64 (dd, J = 8.0, 1.7 Hz, 2H), 7.46(t, J = 7.6 Hz, 4H), 7.38 (tt, J = 7.35, 3.0 Hz, 2H), 7.34 (s, 2H), 6.90 (s, 2H), 6.87 (s, 2H), 2.42 (s, 6H), 1.90 (s, 6H); ^{13}C NMR (125 MHz, $CDCl_3$, δ): 160.07, 155.98, 147.48, 145.79, 138.52, 134.04, 129.28, 128.26 128.01, 127.36, 126.34, 123.37, 120.39, 116.78, 115.58, 111.10, 20.09, 18.33. MS (ASAP) *m/z*: $[M]^+$ calcd 643.58; found, 643.23. Anal. calcd (%) for $C_{46}H_{34}BNO_2$: C 85.85, H 5.32, N 2.18; found: C 85.22, H 5.37, N 2.13.

4. 5. 3. Quantum Chemical Calculations

Quantum chemical calculations were performed using the Gaussian 16 program package. The molecular geometries in the ground state were optimized using the PBE0 functional with the 6-31G(d) basis set in the gas phase. The lowest excited singlet and triplet states as well as the triplet spin density distribution (TSDD) simulation were computed using the optimized structures with time-dependent density functional theory (TDDFT) at the same level. The spin–orbit coupling matrix elements were carried out using ADF2018 program package[41] according to the literature method.[19]

4. 5. 4. Photophysical Measurements

Thin film samples (40 nm) were deposited on quartz glass substrates by vacuum evaporation to study their excitons confinement properties in the film state. Ultraviolet–visible (UV–vis) absorption and photoluminescence (PL) spectra were recorded on a Perkin-Elmer Lambda 950 KPA spectrophotometer and a JASCO FP-6500 fluorescence spectrophotometer, respectively. Absolute PL quantum yields were measured on a Quantaurus-QY measurement system (C11347-11, Hamamatsu Photonics) under nitrogen flow and all samples were excited at 360 nm. The transient PL decay characteristics were recorded using a Quantaurus-Tau fluorescence lifetime measurement system (C11367-03, Hamamatsu Photonics).

4. 5. 5. OLED Fabrication and Characterization

Pre-patterned indium thin oxide (ITO, 50 nm)-coated glass substrates were cleaned with detergent, deionized water, acetone, and isopropanol. The substrates were then exposed to UV–ozone treatment for 15 min before being loaded into an ALS Technology E-200 vacuum evaporation system. The organic layers and cathode Al layer were thermally evaporated on the substrates under vacuum ($< 6 \times 10^{-5}$ Pa) with a deposition rate of < 0.2 nm s^{-1} through a shadow mask, defining a pixel size of 0.04 cm^2. The thickness and deposition rate were monitored in situ during deposition by an oscillating quartz thickness monitor. The current density–voltage–luminance (*J*–*V*–*L*) characteristics of the fabricated OLEDs were measured using a Keithley 2400 source meter and a CS-2000 spectroradiometer (Konica Minolta).

4. 6. Conclusions

In this study, a new deep-blue TADF emitter (**TMCz-BO**), comprising the 5,9-dioxa-13b-boranaphtho[3,2,1-*de*]anthracene (**BO**) acceptor unit with the 1,3,6,8-tetramethyl-9*H*-carbazole (**TMCz**) donor unit, was successfully designed and synthesized, resulted in the deep-blue emission with corresponding CIE chromaticity coordinates of (0.15, 0.18) and (0.14, 0.18) under photo- and electro-excitation, respectively. Thanks to its extraordinarily fast emission lifetime of 750 ns, originating from well valanced k_r, k_{ISC}, and k_{RISC} mediated by the suitably strong spin–orbit coupling between the ^{1}CT and ^{3}LE with maintaining the small activation energy, high external EL quantum efficiencies were achieved to be 20.2% and 17.4% at 100 cd m^{-2} for displays and 1000 cd m^{-2} for lighting sources, respectively.

References

[1] H. Uoyama, K. Goushi, K. Shizu, H. Nomura, C. Adachi, *Nature*, **2012**, 492, 234–238.

[2] Z. Yang, Z. Mao, Z. Xie, Y. Zhang, S. Liu, J Zhao, J. Xu, Z. Chi, M. P. Aldred, *Chem. Soc. Rev.*, **2017**, 46, 915–1016.

[3] M. Y. Wong, E. Zysman-Colman, *Adv. Mater*., **2017**, 29, 1605444.

[4] X. Cai, S-J. Su, *Adv. Funct. Mater.*, **2018**, 28, 1802558.

[5] S. Hirata, Y. Sakai, K. Masui, H. Tanaka, S. Y. Lee, H. Nomura, N. Nakamura, M. Yasumatsu, H. Nakanotani, Q. Zhang, K. Shizu, H. Miyazaki, C. Adachi, *Nat. Mater.*, **2014**, 14, 330–336.

[6] D. R. Lee, M. Kim, S. K. Jeon, S-H. Hwang, C. W. Lee, J. Y. Lee, *Adv. Mater.*, **2015**, 27, 5861–5867.

[7] H. Kaji, H. Suzuki, T. Fukushima, K. Shizu, K. Suzuki, S. Kubo, T. Komino, H. Oiwa, F. Suzuki, A. Wakamiya, Y. Murata, C. Adachi, *Nat. Commun.*, **2015**, 6, 8476.

[8] M. Numata, T. Yasuda, C. Adachi, *Chem. Commun.*, **2015**, 51, 9443–9446.

[9] J. W. Sun, J. Y. Baek, K-H. Kim, C-K. Moon, J-H. Lee, S-K. Kwon, Y-H. Kim, J. J. Kim, *Chem. Mater.*, **2015**, 27, 6675–6681.

[10] T. -A. Lin, T. Chatterjee, W. -L. Tsai, W. -K. Lee, M.-J. Wu, M. Jiao, K.-C. Pan, C. -L. Yi, C. -L. Chung, K. -T. Wong, C. -C. Wu, *Adv. Mater.*, **2016**, 28, 6976–6983.

[11] I. S. Park, J. Lee, T. Yasuda, *J. Mater. Chem. C*, **2016**, 4, 7911–7916.

[12] D. Zhang, M. Cai, Y. Zhang, D. Zhang, L. Duan, *Mater. Horizons*, **2016**, 3, 145–151.

[13] P. Rajamalli, N. Senthilkumar, P.-Y. Huang, C.-C. Ren-Wu, H. -W. Lin, C. -H. Cheng, *J. Am. Chem. Soc.*, **2017**, 139, 10948–10951.

[14] I. S. Park, H. Komiyama, T. Yasuda, *Chem. Sci.*, **2017**, 8, 953–960.

[15] M. Liu, R. Komatsu, X. Cai, K. Hotta, S. Sato, K. Liu, D. Chen, Y. Kato, H. Sasabe, S. Ohisa, Y. Suzuri, D. Yokoyama, S.-J. Su, J. Kido, *Chem. Mater.*, **2017**, 29, 8630–8636.

[16] Y. H. Lee, S. Park, J. Oh, S.-J. Woo, A. Kumar, J. J. Kim, J. Jung, S. Yoo, M. H. Lee, *Adv. Opt. Mater.*, **2018**, 6, 1800385.

[17] R. Furue, K. Matsuo, Y. Ashikari, H. Ooka, N. Amanokura, T. Yasuda, *Adv. Opt. Mater.*, **2018**, 6, 1701147.

[18] T.-L. Wu, M.-J. Huang, C.-C. Lin, P.-Y. Huang, T.-Y. Chou, R.-W. Chen-Cheng, H.-W. Lin, R.-S. Liu, C.-H. Cheng, *Nat. Photonics*, **2018**, 12, 235–240.

[19] I. S. Park, K. Matsuo, N. Aizawa, T. Yasuda, *Adv. Funct. Mater.*, **2018**, 28, 1802031.

[20] D. H. Ahn, S. W. Kim, H. Lee, I. J. Ko, D. Karthik, J. Y. Lee, J. H. Kwon, *Nat. Photonics*, **2019**, 24, 540–546.

[21] Z. Cheng, Z. Li, Y. Xu, J. Liang, C. Lin, J. Wei, Y. Wang, *ACS Appl. Mater. Interfaces*, **2019**, 11, 28096–28105.

[22] S. J. Woo, Y. Kim, S. K. Kwon, Y. H. Kim, J. J. Kim, *ACS Appl. Mater. Interfaces*, **2019**, 11, 7199–7207.

[23] Y. Kondo, K. Yoshiura, S. Kitera, H. Nishi, S. Oda, H. Gotoh, Y. Sasada, M. Yanai, T. Hatakeyama, *Nat. Photonics*, **2019**, 13, 678–682.

[24] Q. Zhang, B. Li, S. Huang, H. Nomura, H. Tanaka, C. Adachi, *Nat. Photonics*, **2014**, 8, 326–332.

[25] C. Murawski, K. Leo, M. C. Gather, *Adv. Mater.*, **2013**, 25, 6801–6827.

[26] K. Masui, H. Nakanotani, C. Adachi, *Org. Electron*, **2013**, 13, 2721–2726.

[27] J. -L. Brédas, D. Beljonne, V. Coropceanu, J. Cornil, *Chem. Rev.*, **2004**, 104, 4971–5004.

[28] K. Schmidt, S. Brovelli, V. Coropceanu, D. Beljonne, J. Cornil, C. Bazzini, T. Caronna, R. Tubino, F. Meinardi, Z. Shuai, J. -L. Bre´das, *J. Phys. Chem. A,* **2007**, 111, 10490–10499.

[29] P. K. Samanta, D. Kim, V. Coropceanu, J.-L. Brédas, *J. Am. Chem. Soc.,* **2017**, 139, 4042–4051.

[30] B. T. Lim, S. Okajima, A. K. Chandra, E. C. Lim, *Chem. Phys. Lett.*, **1981**, 79, 22–27.

[31] M. Baba, *J. Phys. Chem. A*, **2011**, 115, 9514–9519.

[32] J. Gibson, A. P. Monkman, T. J. Penfold, *ChemPhysChem*, **2016**, 17, 2956–2961.

[33] M. K. Etherington, J. Gibson, H. F. Higginbotham, T. J. Penfold, A. P. Monkman, *Nat. Commun.*, **2016**, 7, 13680.

[34] H. Noda, X. -K. Chen, H. Nakanotani, T. Hosokai, M. Miyajima, N. Notsuka, Y. Kashima, J. -L. Brédas, C. Adachi, *Nat. Mater.*, **2019**, 18, 1084–1090.

[35] Y. Wada, H. Nakagawa, S. Matsumoto, Y. Wakisaka, H. Kaji, *ChemRxiv*, **2019**, DOI:10.26434/chemrxiv.9745289.

[36] H. Hirai, K. Nakajima, S. Nakatsuka, K. Shiren, J. Ni, S. Nomura, T. Ikuta, T. Hatakeyama. *Angew. Chemie Int. Ed.*, **2015**, 54, 13581–13585.

[37] P. A. Vecchi, A. B. Padmaperuma, H. Qiao, J. S. Sapochak, P. E. A. Burrows, *Org. Lett.*, **2006**, 8, 4211–4214.

[38] T. Ogiwara, Y. Wakikawa, T. Ikoma, *J. Phys. Chem. A*, **2015**, 119, 3415–3418.

[39] F. B. Dias, J. Santos, D. R. Graves, P. Data, R. S. Nobuyasu, M. A. Fox, A. S. Batsanov, T. Palmeira, M. N. Berberan-Santos, M. R. Bryce, A. P. Monkman, *Adv. Sci.*, **2016**, 3, 1600080.

[40] T. Hatakeyama, K. Shiren, K. Nakajima, S. Nomura, S. Nakatsuka, K. Kinoshita, J. Ni, Y. Ono, T. Ikuta, *Adv. Mater.*, **2016**, 28, 2777–2781.

[41] ADF2018, SCM, Theoretical Chemistry, Vrije Universiteit, Amsterdam, The Netherlands, http://www.scm.com/. **2014**, *15*, 034202.

[42] Y. Xiang, Z. L. Zhu, D. Xie, S. Gong, K. Wu, G. Xie, C. S. Lee, C. Yang, *J. Mater. Chem. C*, **2018**, 6, 7111–7118.

Chapter 5

Summary and Perspective

In this dissertation, I designed and synthesized new host and TADF molecules aimed for relaxed efficiency rolloff in TADF-OLEDs.

In **Chapter 2**, a new green TADF emitters have been designed and synthesized by combining a dibenzo[*b*,*d*]thiophene 5,5-dioxide acceptor core with 9,9-dimethyl-9,10-dihydroacridine donor units. The photophysical and EL properties were tuned by a rational substituted position of the donors in dibenzo[*b*,*d*]thiophene 5,5-dioxide derivatives. A small ΔE_{ST} was derived from *para*-position based **4ASOA**, which had a relatively faster k_{RISC} than that of *meta*-position based **3ASOA**. The OLEDs based on these TADF emitters exhibited the maximum external EL quantum efficiencies (η_{ext}) of 10.4% and 13.8%, respectively. It is noteworthy that the slightly relaxed efficiency rolloff behavior resulting from its fast k_{RISC} was achieved from the **4ASOA**-based device. These results indicated that the efficiency rolloff behavior of TADF-OLEDs were largely depended on k_{RISC} of an emitter, indicating that a delicate tuning of donor and acceptor arrangement surely enhances TADF properties.

In **Chapter 3**, two ambipolar host materials, **CzPO** and **Cz3PO**, with high triplet energies were designed and synthesized for use in sky-blue TADF-based OLEDs. Compared to the device employing the most widely used **DPEPO** host material, reduced efficiency rolloffs were observed in sky blue TADF-based OLEDs using **CzPO** and **Cz3PO** as ambipolar host materials. **CzPO** and **Cz3PO** were confirmed to be ambipolar nature, in which **CzPO-** and **Cz3PO-**based devices exhibited balanced hole and electron transporting/injection properties. Thus, the well-balanced charge flux and broad distributions of the charge-recombination zones within the EML resulted in enhanced efficiency rolloff characteristics for **CzPO-** and **Cz3PO-**based OLEDs.

In **Chapter 4**, a new deep-blue TADF emitter (**TMCz-BO**), comprising the 5,9-dioxa-13*b*-boranaphtho[3,2,1-*de*]anthracene (**BO**) acceptor unit with the 1,3,6,8-tetramethyl-9*H*-carbazole (**TMCz**) donor unit was successfully designed and synthesized, which displayed deep-blue emission with corresponding CIE chromaticity coordinates of (0.15, 0.18) and (0.14, 0.18) under photo- and electrical excitations, respectively. Thanks to its extraordinarily fast emission lifetime of 750 ns originating from well balanced k_{r}, k_{ISC}, and k_{RISC} mediated by the suitably strong spin–orbit coupling between the ^{1}CT and ^{3}LE with maintaining the small activation energy, high η_{ext} of 20.2% and 17.4% at 100 cd m^{-2} and 1000 cd m^{-2} was achieved. Therefore, a larger k_{r} than a k_{ISC} as well as minimizing difference between a k_{ISC} and k_{RISC} as small as possible with maintaining $^1\mathrm{CT} \approx {}^3\mathrm{CT} \approx {}^3\mathrm{LE}$ are concurrently required for TADF molecules possessing ideally fastest exciton lifetime. In summary, the balance of rate constants

k_r, k_{ISC}, and k_{RISC} is the decisive factor controlling the exciton lifetimes, which will be widely employed in advanced TADF molecular design for relaxed efficiency rolloff in deep-blue TADF-OLEDs.

Finally, I would like to propose one approach for relaxed efficiency rolloff in blue TADF-OLEDs. Usually, D–A type pure blue TADF molecules have both high S_1 and T_1 energies ($E_T \geq 2.9$ eV). Therefore, the selection of blue host materials is quite limited since they have to possess high T_1 energies to prevent backward energy transfer from a T_1 state of an emitting molecule to that of a host molecule. Until now, the electron transfer (ET)-type host materials with high T_1 energies, i.e., DPEPO or PPF that have high E_T values of over 3.1 eV, are most widely used for blue TADF-based OLEDs, because almost hole transfer (HT)-type host materials have relatively lower T_1 energies, e.g., mCP = 2.9 eV and mCBP = 2.8 eV. However, these ET-type host materials lead to poor operation stability of the devices, since C–P bonds in the ET-type host materials have rather lower bond dissociation energies compared to those of C–C and C–N bonds. Thus, such ET-type host materials have a serious weakness in efficiency rolloff. Recently, Hatakeyama and co-workers reported a new series of TADF materials (**Figure 5-1**), which displayed pure blue emission with relatively lower T_1 energies by introducing a multi-resonance effect.[1] As a result, nearly 100% internal quantum efficiency (η_{int}) was successfully achieved even with a doped film of DABNA-2 in a HT-type mCBP host matrix. However, despite of the high η_{int}, serious efficiency rolloff behavior was observed in a DABNA-2-based OLED due to the quite long triplet exciton lifetime (≈ms) of DABNA-2.

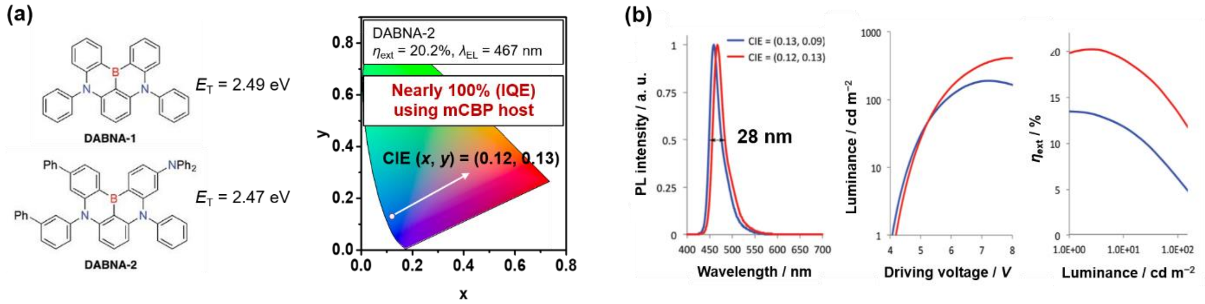

Figure 5-1. (a) Molecular structures and CIE chromaticity coordinates of DABNA-1 and -2-based OLEDs, (b) Normalized EL spectra and external EL quantum efficiency (η_{ext}) *versus* luminance plots of DABNA-1 and -2-based OLEDs.

Thus, rational molecular design strategies for blue TADF molecules are required to realize highly efficient blue TADF-OLEDs. As mentioned in **Chapter 4**, the author successfully realized the high-performance deep-blue TADF-OLED with improved efficiency rolloff, resulting from designing the blue TADF material possessing extraordinary fast delayed lifetime. Further, I'd like to propose a new molecular design for multi-resonance induced pure blue TADF materials having strong spin–orbit coupling between the S_1 and T_n states ($n \geq 2$). There are two intrinsic chemical and physical requirements for pure blue emitters; (i) efficient multi-resonance effect for sharp emission, which should allow employing HT-type host materials in pure blue OLEDs to improve operational stability, (ii) employing heavy atoms (S, Se, Te) in molecules, which should induce strong spin–orbit coupling between the excited singlet and triplet states, leading to decreasing triplet exciton lifetimes by accelerating k_{RISC} of emitters. Consequentially, relaxed efficiency rolloff characteristics would be realized in pure blue TADF-OLEDs by suppressing triple–triplet annihilation and/or singlet–triplet annihilation. I expect that the satisfaction of these requirements would realize high efficiency and stable blue TADF-OLEDs.

Reference

[1] T. Hatakeyama, K. Shiren, K. Nakajima, S. Nomura, S. Nakatsuka, K. Kinoshita, J. Ni, Y. Ono, T. Ikuta, *Adv. Mater.*, **2016**, 28, 2777–2781.

List of Publications

■ Original Papers

[1] **Jong Uk Kim**, Saripally Sudhaker Reddy, Lin-Song Cui, Hiroko Nomura, Sunbin Hwang, Dae Hyeon Kim, Hajime Nakanotani, Sung-Ho Jin, and Chihaya Adachi,
"Thermally Activated Delayed Fluorescence of Bis(9,9-dimethyl-9,10-dihydroacridine) dibenzo[*b*,*d*]thiophene 5,5-dioxide Derivatives for Organic Light-Emitting Diodes"
Journal of Luminescence, **2017,** 190, 485. (**Chapter 2**)

[2] **Jong Uk Kim**, Michael Y. Wong, Shiv Kumar, Oliver G. Hayes, Finlay Duncan, Chin-Yiu Chan, Ben Yiu-Wing Wong, Hao Ye, Lin-Song Cui, Hajime Nakanotani, Eli Zysman-Colman, and Chihaya Adachi,
"High-Triplet-Energy Bipolar Host Materials Based on Phosphine Oxide Derivatives for Efficient Sky-Blue Thermally Activated Delayed Fluorescence Organic Light-Emitting Diodes with Reduced Rolloff"
Chemistry Letters, **2019**, 48, 1225. (**Chapter 3**)

[3] **Jong Uk Kim**, In Seob Park, Chin-Yiu Chan, Masaki Tanaka, Youichi Tsuchiya, Hajime Nakanotani, and Chihaya Adachi,
"A Nanosecond Time Scale Delayed Fluorescence Molecule for Deep-Blue Organic Light-Emitting Diodes with Small Efficiency Rolloff"
Nature Communications, **2020**, 11, 1765. (**Chapter 4**)

■ Joint Papers

[1] Lin-Song Cui, **Jong Uk Kim**, Hiroko Nomura, Hajime Nakanotani, and Chihaya Adachi,
"Benzimidazobenzothiazole-based Bipolar Hosts to Harvest Nearly All Excitons in Blue Delayed Fluorescence and Phosphorescent Organic Light-Emitting Diodes"
Angewandte Chemie International Edition, **2016**, 55, 6864–6868.

[2] Lin-Song Cui, Hiroko Nomura, Yan Geng, **Jong Uk Kim**, Hajime Nakanotani, and Chihaya Adachi,
"Controlling Singlet-Triplet Energy Splitting for Deep-Blue Thermally Ac tivated Delayed Fluorescence Emitters"
Angewandte Chemie International Edition, **2016**, 56, 1571–1575.

[3] Yan Geng, Lin-Song Cui, **Jong Uk Kim**, Hajime Nakanotani, and Chihaya adachi,
"Molecular Design for Blue Thermal Activated Delayed Fluorescence Materials: Substitution Position Effect"
Chemistry Letters, **2017** 46, 10, 1490–1492.

[4] Yan Geng, Anthony D'Aleo, Ko Inada, Lin-Song Cui, **Jong Uk Kim**, Hajime Nakanotani, andChihaya Adachi,
"Donor-σ-Acceptor Motif Thermally Activated Delayed Fluorescence Emitters with Dual Upconversion"
Angewandte Chemie International Edition, **2016**, 56, 16536–16540.

[5] Chin-Yiu Chan, Lin-Song Cui, **Jong Uk Kim**, Hajime Nakanotani, and Chihaya Adachi,
"Rational Molecular Design for Deep-Blue Thermally Activated Delayed Fluorescence Emitters"
Advanced Functional Materials, **2018**, 28, 1706023.

[6] Hao Ye, Dae Hyeon Kim, Xiankai Chen, Atula S. D. Sandanayaka, **Jong Uk Kim**, Elena Zaborov, Gabriel Canard, Youichi Tsuchiya, Eun Young Choi, Jeong Weon Wu, Frédéric Fages, Jean-Luc Bredas, Anthony D'Aléo, Jean-Charles Ribierre, and Chihaya Adachi,
"Near-Infrared Electroluminescence and Low Threshold Amplified Spontaneous Emission above 800 nm from a Thermally Activated Delayed Fluorescent Emitter"
Chemistry of Materials, **2018**, 30, 19, 6702–6710.

[7] Morgan Auffray, Dae Hyeon Kim, **Jong Uk Kim**, Fatima Bencheikh, David Kreher, Qisheng Zhang, Anthony D'Aléo, Jean-Charles Ribierre, Fabrice Mathevet, and Chihaya Adachi,
"Dithia[3.3]paracyclophane Core: a Versatile Platform for Fine Triplet State Tuning and Through Space TADF Emission"
Chemistry - An Asian Journal, **2019**. 14, 1921–1925.

List of Symposium

■ International Symposium

[1] **Jong Uk Kim**, Ko Inada, Lin-Song Cui, Hajame Nakanotani, and Chihaya Adachi, *International Conference on Solid State Devices and Materials (SSDM2016)*, Ibaraki Japan (September 26–29, 2016), Oral presentation

[2] **Jong Uk Kim**, Ko Inada, Lin-Song Cui, Hajame Nakanotani, and Chihaya Adachi, *2nd International TADF Workshop* Kyushu, Japan (July 19-21, 2017), Poster presentation

[3] **Jong Uk Kim**, Ko Inada, Lin-Song Cui, Hajame Nakanotani, and Chihaya Adachi, *The 9th Asian Conference on Organic Electronics (A-COE2017),* Daejeon, Korea (October 25-27, 2017), Poster presentation.

.

Acknowledgments

Firstly, the author would like to dedicate his utmost gratitude to Professor Chihaya Adachi and Professor Hajime Nakanotani at of Kyushu University for their helpful advices in progressing advanced research and for the many opportunities given throughout the doctoral course.

The author is deeply grateful to Professor Ken Onda and Professor Hisashi Shimakoshi for their helpful and intellectual discussions as well as constructive comments regarding this thesis.

The author would like to acknowledge the continuous counseling, motivation and encouragement from Professor Takuma Yasuda and Research Assistant Professor In Seob Park in synthesis and summarizing work. Their valuable advices laid the foundation for the success of this synthesis work.

The author would also like to thank Associate Professor Ryota Kabe and Dr. Sunbin Hwang for their patience and guidance throughout the doctoral studies, especially when dealing with unfamiliar equipment, laboratory rules and regulations when the author first joined the Adachi lab.

The author would like to thank the TADF group members - Dr. Yan Geng, Lin-song Cui, Chin-Yiu Chan; Ben Yiu-Wing Wong, Hao Ye, Masaki Tanaka, Yi-Ting Lee, Umamahesh Balijapalli, Youichi Tsuchiya for their inspiring discussions and crucial comments. The author is also grateful to Ms. Nozomi Nakamura and Keiko Kusuhara for their technical support.

The author would also like to thank all the staffs of the Adachi lab for taking care of the daily life in laboratory. Especially, the author want to thank Ms. Sachiko Higashikawa for handling the Ph.D. degree application. The author will remember their endless help and keep that in mind forever.

The author is deeply indebted to Professor Se Mo Son at Pukyong National University for invaluable advices and the great opportunity to study in Kyushu University, Japan.

Finally, the author would like to express his deepest appreciation to his family members: his parents, his wife, his brother, and his relatives. Their emotional support, love, and encouragement have inspired the author to complete this thesis.